Optical Properties of Amorphous Selenium Films

A Thesis

Submitted to the College of Graduate Studies and Research

In Partial Fulfillment of the Requirements for the

Degree of Master of Science

In the Department of Electrical Engineering

University of Saskatchewan

By

Wee Chong Tan

Saskatoon, Saskatchewan

Permission to Use

In presenting this thesis in partial fulfillment of the requirements for a Postgraduate degree from the University of Saskatchewan, I agree that the Libraries of this University may make it freely available for inspection. I further agree that permission for copying of this thesis in any manner, in whole or in part, for scholarly purposes may be granted by the professor or professors who supervised my thesis work or, in their absence, by the Head of the Department or the Dean of the College in which my thesis work was done. It is understood that any copying or publication or use of this thesis or parts thereof for financial gain shall not be allowed without my written permission. It is also understood that due recognition shall be given to me and to the University of Saskatchewan in any scholarly use which may be made of any material in my thesis.

Requests for permission to copy or to make other use of material in this thesis in whole or part should be addressed to:

Head of the Department of Electrical and Computer Engineering

University of Saskatchewan

Saskatoon, Canada, S7N 5A9

Acknowledgements

I extend my sincerest gratitude towards my supervisor, Dr. S.O. Kasap, and my co-supervisor, Dr. R. Johanson, for their patience, encouragement and leadership throughout the course of this project. I also thank Dr. K. Koughia for his assistance in the interpretation of the experimental data, Dr. Martin Munzar for his coaching on the spectrometer and the Swanepoel method of analysis and George Belev for his help in sample preparation. This thesis would not have been possible without the financial support from the University of Saskatchewan. Finally, I would like to thank my family, colleague, and friends for their support, encouragement and patience.

Abstract

Recently there has been a substantial renewed interest in the electrical and optical properties of amorphous selenium (a-Se) films due to its use as an ultra-sensitive photoconductor in the newly developed flat panel x-ray image detector and high definition digital and video camera. This project has examined the optical properties of a range of a-Se films fabricated by conventional vacuum deposition technique. The films were deposited at two substrate temperatures called hot and cold deposition: (i) at 51°C, which is above the glass transition temperature ($T_g \approx 40$°C), and (ii) at 3°C, well below the glass transition temperature. The transmission spectrum $T(\lambda)$ of all the a-Se films were measured over a wide range of wavelengths from 500 nm to 2500 nm, and analyzed using the Swanepoel technique. The thickness, absorption coefficient $\alpha(\lambda)$, refractive index $n(\lambda)$, and optical bandgap, Eg_T and Eg_U, in different absorption regions of a-Se were all extracted using the Swanepoel technique. A systematic way to improve the accuracy of the calculations was also developed and the n vs. λ data was fitted to the Sellmeier dispersion equation. The optical bandgap Eg_T was obtained from the $\alpha h \upsilon$ vs $h \upsilon$ plot of the absorption spectrum and the Urbach tail was obtained from a semi-logarithmic plot of α vs $h \upsilon$. With all essential optical properties collected, the influence of thermal annealing, the deposition temperature, doping, thickness and aging time on the optical properties of a-Se films was studied.

Amorphous selenium is essentially a glass, and all glasses exhibit some degree of structural relaxation effects during which the physical properties such as the refractive index and the bandgap change with time, called "aging". First of all, thermal annealing an a-Se film at $T = 51$°C for an hour reduces the thickness by ~15% and increases the refractive index by ~0.5%. The optical bandgap does not change by more than 0.2%. While the decrease in the thickness is thought to be due to the rearrangement of the molecular clusters and the amorphous network, the increase in the refractive index is believed to be linked to the densification and the polarizability of the material. Although the influence of the thickness of the film, the temperature of the glass substrate, and the doping of 67ppm of chlorine on the optical properties of the a-Se film was found to be negligible, there are noticeable changes during aging. It was found that an aged a-Se film that was cold deposited has an increased refractive index that is believed to be caused by densification alone. In a period of 2 months, the thickness of a cold deposited a-Se:67ppm-Cl film shrinks by 3.5% and the refractive index increases by 3.7%. The optical bandgap of the film decreases by 0.6%. Similar aging trends in the thickness, the refractive index, and the optical bandgap were also observed in a cold deposited a-Se film but no significant changes, at least not more than 0.5% deviation, were noted in a period of about 1-3 weeks in any aging a-Se films that were hot deposited or annealed.

Table of Contents

List of Figures

List of Tables

List of Abbreviations

a-Se	amorphous selenium
AB	anti-bonding
AMFPI	active matrix flat-panel imager
CFO	density of states model proposed by Cohen, Fritsche and Ovshinski
Cl	chlorine
DOS	density of state
EHP	electron hole pair
ESR	electron spin resonance
HARP	high gain avalanche rushing amorphous photoconductor
HD	high definition
IF	intermediate frequency
IFTOF	interrupted field time-of-flight
IR	Infrared
IVAP	intimate valence alternation pair
LP	lone pair
NA	Not Applicable
NB	non-bonding
NIR	near infrared
NSB	normal structure bonding
PPM	parts per million
Se	selenium
TOF	time-of-flight
VAP	valence alternation pair

1. Optical Properties of Materials

1.1 Introduction

Today, the field of optics is expanding at an explosive rate. The arrival of optical communications, personal computers, and digital television around the world has placed a heavy burden on materials and devices for signal transmission and processing. In telecommunication, the benefits of optical techniques for signal processing and transmission have already changed our lives in a major way by giving us access to the information superhighway.

At the same time, an intense research effort is currently under way to integrate multiple optical technologies onto a single chip. In this chip, there will be a system in which optical signals are generated by micro-lasers, shaped by thin-film digital lenses, and coupled into optical waveguide channels by nonlinear optical switches for transmission. Within the same chip, there will also be optical logic gates where the optical signals can be analyzed and holographic data storage media where information can be stored. Incorporating all these functions into a single computer chip is no longer beyond our reach [1].

These advances are not possible without a good understanding of the optical characteristics of photonic materials and its role in the future will expand even further when photonics finds its way into new applications in transportation, medicine, biotechnologies, environmental pollution detection, conservation and power production [2]. Figure 1.1 and Figure 1.2 show the connection between key technologies and photonics, and their applications respectively. An important part of photonics involves the capture of images as in CCD image sensors or video tubes.
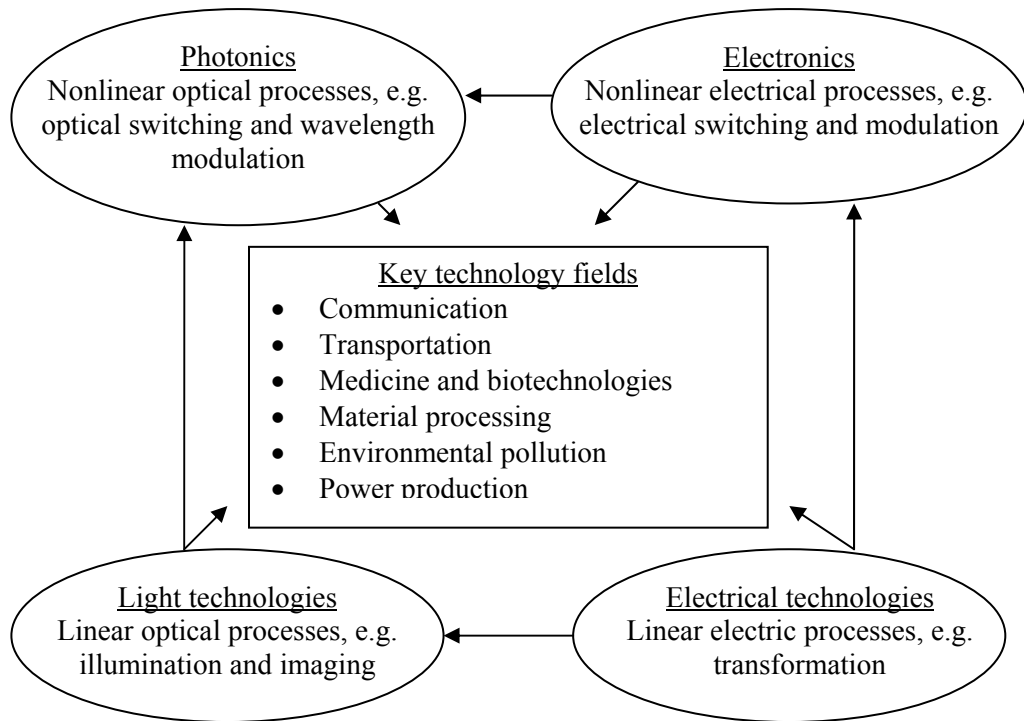
Figure 1.1: Relationship between Photonics and Key Technologies [2]. The arrows show the direction of the knowledge.
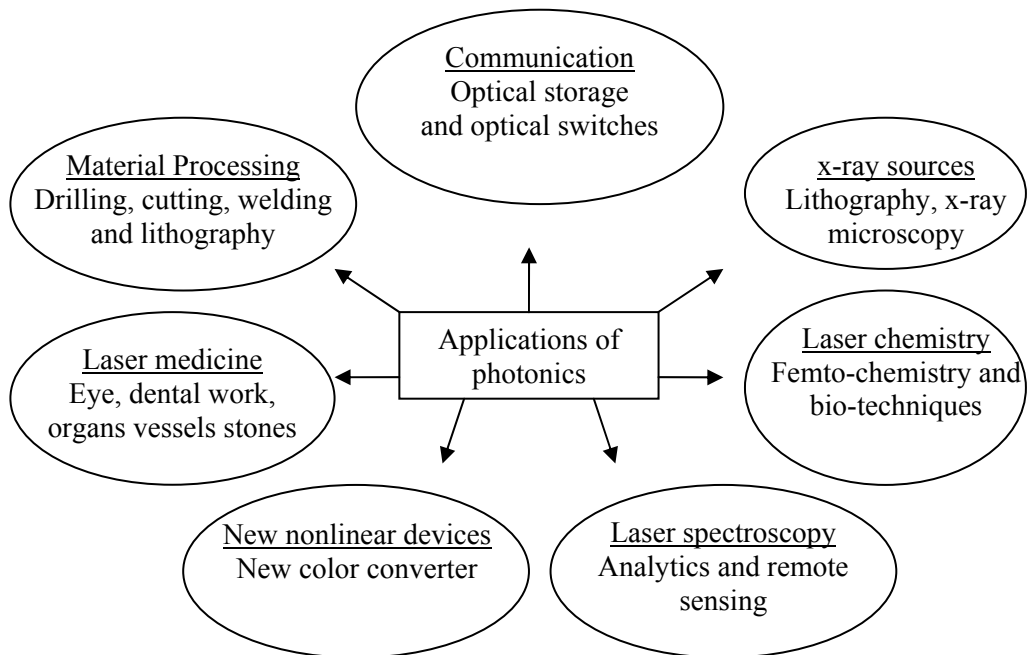
Figure 1.2: Specific Applications of Photonics [2].

1.2 Optical Characterization Techniques

The selection of the appropriate optical or optoelectronic material for a particular application requires a firm understanding of its optical properties. Many applications require the material in thin form. Microscopic defects, which control surface smoothness and coating homogeneity, contribute to the scattering of light and the associated degradation of the optical response. Similarly, structural disturbances at the atomic level can alter the optical properties through modifications to the complex refractive index of the material. To characterize defects at this level, high-resolution diffraction measurements coupled with the evaluation of localized chemical bonding using molecular spectroscopic techniques may be required. Such an approach can provide information regarding the structural phase of the material, the degree of surface or interfacial stress present, and the nature of the chemical bonding associated with a particular structure. Several surface analytical methods are also used to probe these materials to discern structure-property relationships at length scales ranging from micrometers to tenths of nanometers.

Although the surface structure and the microstructure act to distort the optical response of materials, the nature of chemical bonding, the deviations from stoichiometry, and the presence of impurities can influence the intrinsic optical properties to a greater extent. Standard surface probing techniques, such as Auger spectroscopy (AES), x-ray photoemission spectroscopy (XPS), secondary ion mass spectroscopy (SIMS), and Rutherford backscattering spectroscopy (RBS) are very useful for the elemental identification and concentration depth profiling of thin films. However, subtle changes in chemical bonding, which can produce large changes in the optical response, often are difficult to quantify using these techniques, particularly when the material under investigation is nonconducting or when bound hydrogen is an integral component of the material. Infrared absorption and inelastic light scattering (Raman spectroscopy) are two principal nondestructive methods that have been used extensively for the characterization of optical materials. Significant advances in the application of vibrational spectroscopy to the analysis of surfaces and interfaces and the successful

application of the Swanepoel technique, which will be elaborated later in Chapter 4, to the transmission spectrum of thin films have also been reported during the past several years.

The design and development of specialty thin film coatings is one of the principal thrusts in the optical materials area. Multilayer dielectric stacks are used to regulate the transmission and reflection properties of a surface by means of interference phenomena. Variations in individual layer composition, which control the refractive index and layer thickness, are used to develop antireflection (AR) coatings and high reflection (HR) mirrors. These kinds of coating are used in high power laser systems and for controlling light transmission in optical windows. In many of these applications, irreversible changes in transmittance can be introduced as a result of an applied stress (mechanical, thermal, or chemical) which alters the chemical and/or physical properties of the surface. For example, sputter-deposited coatings are often found to exhibit a columnar grain microstructure. Diffusion of water through the inter-granular channels will lead to either reversible changes in the layer's refractive index, depending on the amount adsorbed, or irreversible changes if the water chemically interacts with the dielectric material. The mechanism for this type of failure has been substantiated using a variety of surface analytical techniques [3].

1.3 Amorphous Selenium as an Optoelectronic Material

The study of the optical properties of amorphous selenium is important not only because it is an excellent photoconductor used in active matrix flat-panel imager, AMFPI, for digital x-ray imaging [4, 5] and in high-sensitivity video tube, called HARPICON for HD Television [6], but also because it belongs to a class of amorphous semiconductors referred to as the chalcogenides.

Chalcogenides are compounds of the group VIB elements and group IIIB, IVB and/or VB elements of the periodic table. VIB elements comprise Sulphur (S), Selenium (Se)

and Tellurium (Te), which are also called chalcogens, while group IIIB, IVB and/or VB elements are namely Arsenic (As), Germanium (Ge), Antimony (Sb), Phosphorus (P) etc. These glasses have low-phonon energies ($\alpha \sim$ 300-500 cm^{-1}), with attenuations less than 1 dB/m being reported for As-S fibers in the 2-3μm wavelength range, and a wide transmission range from visible to infrared region (up to 20 μm) [7]. The potential applications of chalcogenide based materials in electronic and optoelectronic devices are vast, but has received little attention until recently due to the cheap and wide availability of silicon based alternatives. However, as the use of silica as an electronic/optoelectronic material is rapidly approaching its physical limitations, research into chalcogenide materials is receiving increasing attention around the world. Various passive and active applications of chalcogenide glasses in photonics, whether potential or realized, have already been demonstrated in the fabrication of IF fibers, planar waveguides, Bragg diffraction gratings, photoinduced holograms, and rare-earth doped films. Their large refractive index and high probability of radiative transitions make them a very attractive host material for active optical devices that are based on rare-earth elements, e.g. Er, Nd, Pr, etc. As the nonlinearity of their optical properties is about 3 orders of magnitude greater than that of silica, chalcogenide glasses are also an ideal candidate for use in optical switching devices.

At present, the commercial importance of amorphous selenium (a-Se) and its various alloys lies in their use as a vidicon photoconductor material (e.g. Se-Te alloys) and as a photoconductor in x-ray imaging. Moreover, with the advent of digital medical imaging, the use of a-Se in direct conversion flat panel digital x-ray detectors is likely to experience substantial growth in near future. There are currently also a number of potential applications for selenium-based glassy alloys. These are found in large area x-ray sensitive vidicons for medical imaging, called the X-icon, in electro-photographic light-to-image converter imaging devices, optical storage, IR fiber optics and optical recording of images via selective photo-deposition of a-Se films from a colloid [8].
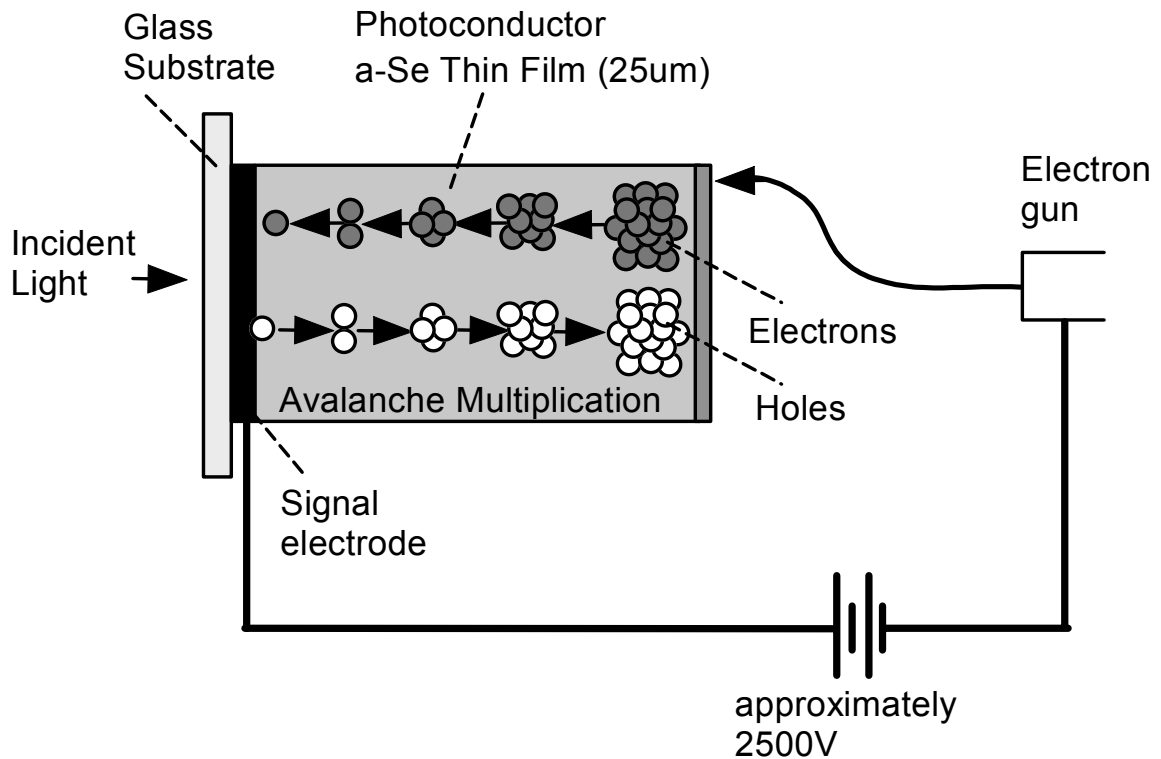
Figure 1.3: Operating principle of the new Super-HARP tube [6].

One other interesting application for selenium-based glassy alloys is in high-sensitivity TV pickup or video tubes, called the HARPICON. In a High-gain Avalanche Rushing amorphous Photoconductor, or HARP, an electron-hole pair is produced by an incident photon. The photo-carriers are then accelerated by the large electric field applied to an *a-Se* target. These accelerated carriers produce other electron-hole pairs through impact ionization. The impact ionization phenomenon occurs repeatedly inside the target and leads to an avalanche effect that enables the video tube to capture clear images with full color reproduction even in the "dark", 50×10^{-6} lux. Figure 1.3 shows the basic operating principle of a HARP video tube. Since the sensitivity of the camera can be varied over a wide range by changing the voltage applied to the target, there will be no problem using it during the day or under normal lighting conditions. Figure 1.4 shows the new Super-HARP tube and illustrates the kind of pictures a HARP-fitted video camera is capable of reproducing [6].
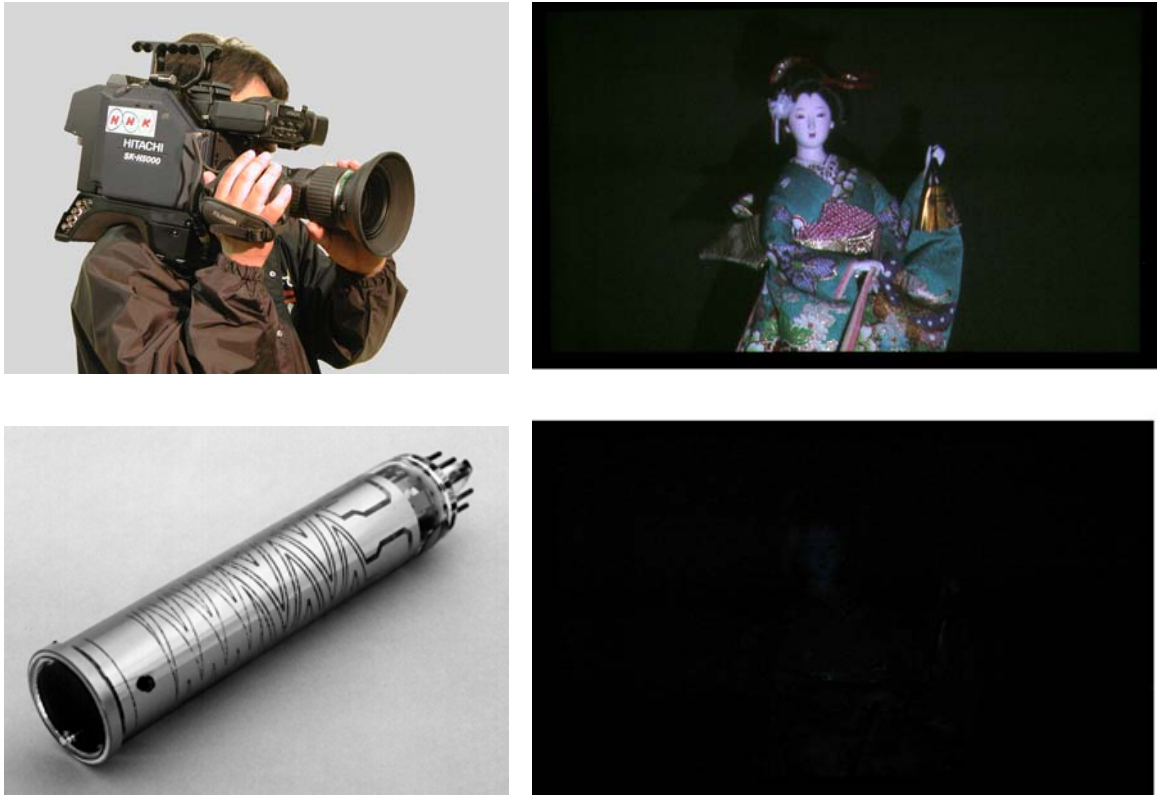
Figure 1.4: The top left corner of the figure shows the HARP-fitted video camera used in capturing the image in the upper right corner. At the bottom right corner of the figure is a picture of the same image shown in the upper right corner except this time it was captured using an video camera without the HARP tube. The bottom left corner of the figure shows the new Super-HARP tube designed for a HD video camera. The sensitivity of the experimental HD video camera shown above was 0.8 lux and its resolution was 1000 TV lines with a lag time of less than 0.1%. Note: moonlight is equivalent to 1 lux and starlight is equivalent to 50×10^{-6} lux [6].

Besides being used as a high gain photoconductor in the making of a HDTV camera, the HARP can also be made into an ultrahigh-sensitivity CMOS image sensor. This sensor can then be used in imaging devices like video and digital cameras to enhance their sensitivity and resolution. The proposed ultrahigh-sensitivity CMOS image sensor is shown in the diagram below.
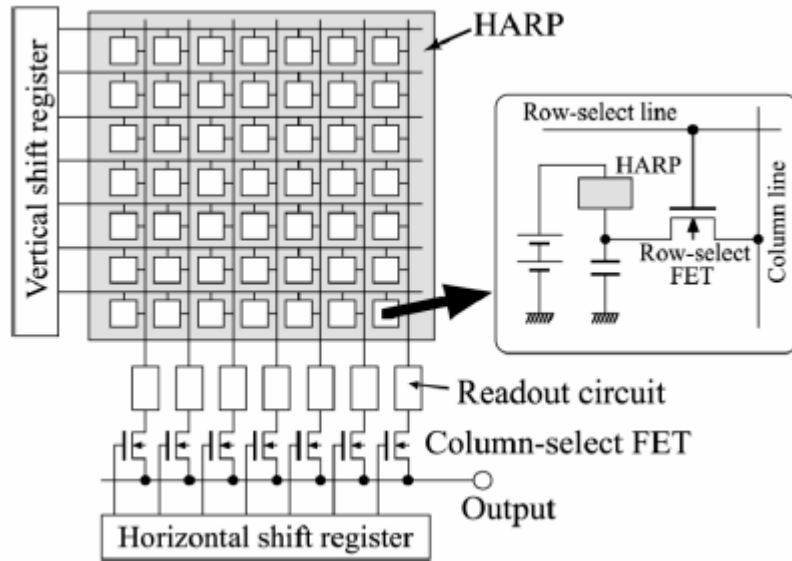
Figure 1.5: Schematic diagram of the solid-state HARP image sensor (after [9]).

1.4 Research Objective

Amorphous films are known to have properties that are sometimes different from their bulk glass counterparts. They typically have more defects and may or may not exhibit the same degree of structural relaxation. This is because materials that are deposited as thin films usually exhibit some degree of interfacial stress arising in part from the difference in the thermal expansion coefficients or lattice mismatch between the film and the substrate material. Since the magnitude of such interfacial stresses can be influenced by changing the film deposition parameters, or through physical or chemical interactions with the environment, it is interesting to know how the substrate deposition temperature and the process of thermal annealing will influence the behavior of a-Se thin films.

Other than having properties that depend on the deposition conditions, amorphous selenium is also intrinsically metastable, a feature unique to the amorphous phase. The chalcogenide glasses, including a-Se, exhibit a variety of photoinduced effects such as photo-induced darkening, bleaching, dichroism, expansion, and crystallization. These photoinduced effects greatly affect their optical properties and allow them to easily

8

transform from one metastable state to another by means of external stimuli. Depending on the situation, the photoinduced effects can either be beneficial or undesirable. Some applications that make use of these effects are in high-density optical memories and photolithography. On the other hand, photo-induced degradation in some amorphous semiconductors is why devices like the solar cells and the flat panel x-ray detector are still not widely used in the market. Since *a*-Se is intrinsically metastable, it is interesting to know whether *a*-Se will undergo structural relaxation (aging) and whether thermal annealing affects its optical properties. The main goals of this project are as follows:

i. Prepare *a*-Se films of different thickness by vacuum deposition.

ii. Measure their thickness and optical properties, i.e. the refractive index *n*, the absorption coefficient α, the optical bandgap Eg_T obtained from $\alpha > 10^4$ cm^{-1}, the optical bandgap Eg_U obtained from absorption region lower than $\alpha = 10^4$ cm^{-1} and the slope of the absorption coefficient ΔE in absorption region lower than $\alpha = 10^4$ cm^{-1}.

iii. Examine how the optical properties depend on annealing, thickness, aging and doping with chlorine. (*a*-Se is doped with chlorine to improve hole transport which is important in applications such as the HARPICON).

The above measurements will then have to be analyzed and interpreted in terms of our current understanding on amorphous semiconductors.

1.5 Thesis Outline

This thesis is divided into a total of six chapters. Following this introductory chapter, a brief overview of the various electrical and optical properties of amorphous selenium will be given in Chapter 2. A step by step description of how the various samples were prepared and measured can be found in Chapter 3. Chapter 4 will describe in detail the method used to extract the optical properties of the material and the mathematical expressions used for the calculation of the optical constants from the transmission measurement. The results and discussion of how these properties vary with different

parameters and conditions are given in Chapter 5. Chapter 6 summarizes all the findings and provides the conclusions of this work.

2. Properties of Amorphous Selenium

2.1 Introduction

In order to gain some measure of understanding of the unique electronic and optical properties of amorphous semiconductors, a theoretical grasp of its energy band structure is required. This can be done by applying quantum mechanic to an amorphous system. However, due to the absence of periodicity, or more specifically the loss of long range order in an amorphous material, quantum mechanical methods that so effectively predict the behavior of crystalline semiconductors become mathematically too complex to apply in such a system. As a result, the behavior of an amorphous semiconductor cannot be derived in the same manner as in a crystalline material but are determined by studying the energy band structure that was mapped from observations obtained from various rigorous experiments. The chapter will begin with a brief introduction to an amorphous solid in general before narrowing down the discussion to amorphous selenium.

2.2 The Atomic Structure of Amorphous Solids

All solids that do not have long range periodicity in their arrangement of its atoms can be termed as amorphous or "structureless". They are best defined when compared to a crystalline solid which has a distinctive regular spatial arrangement of atoms throughout the whole material. In fact they are often simply referred to as non-crystalline materials. Although their structure appears random over the long range, an amorphous substance still has a high degree of short range spatial order in its atomic structure. This is because individual atoms in an amorphous solid must still fulfill their requirement for valence bonding. However, unlike their crystalline counterpart, there are some small deviations in the bonding angles between adjacent atoms and this leads to a disruption of the

periodicity in the material. Figure 2.1 illustrates the difference between a crystalline and an amorphous solid.

(a)   (b)
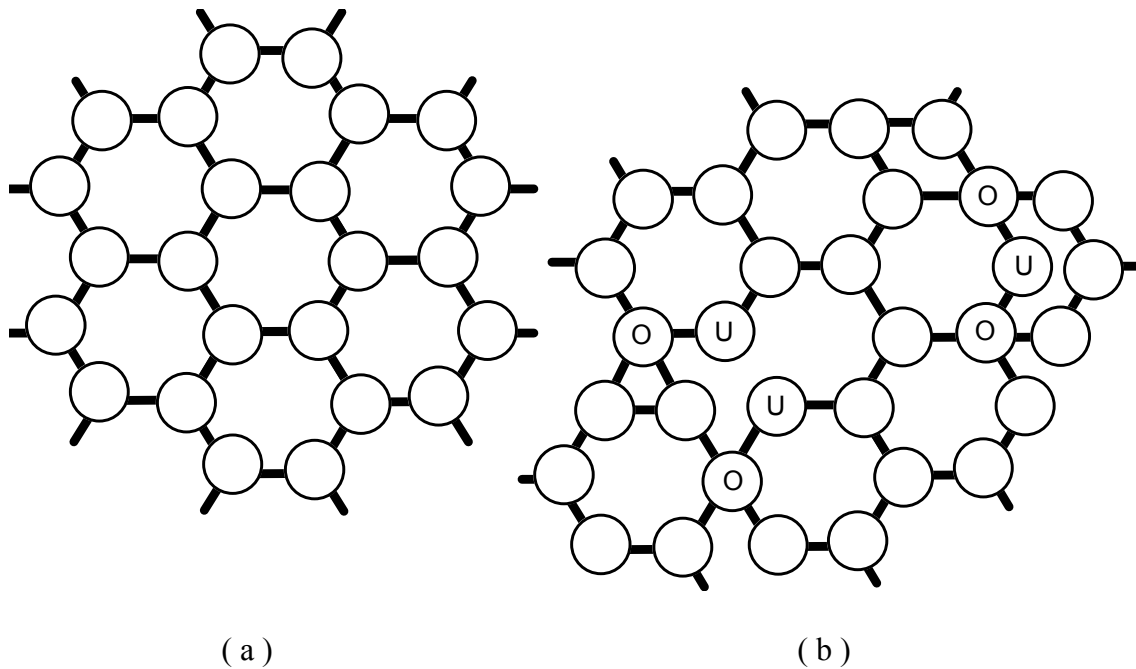
Figure 2.1: Two dimensional representation of the structure of (a) a crystalline solid and (b) an amorphous solid. Atoms marked "O" represent over-coordinated atoms with more than usual numbers of bonding with adjacent atoms and "U" represent under-coordinated atoms with less than the usual number of bonds with adjacent atoms.

2.3 Band Theory of Amorphous Semiconductors

Although an amorphous semiconductor is a non-crystalline material, the band theory of amorphous semiconductors is closely related to its crystalline counterpart. The theory was called the band theory because when quantum mechanics was applied to a crystal, bands of allowable energy states were brought into existence. Besides these bands of allowable states, which are often grouped into two principle bands labeled as the valence and conduction bands, there is also a bandgap separating the two bands where no electron states can exist. Very often the density of states (DOS) diagram is used to explain or predict the properties of a material in the band theory. It denotes the number of electron states per unit energy per electron a material will have at an energy level and is used successfully to describe many of the characteristic found in a crystalline

semiconductor. When it was discovered that amorphous and crystalline semiconductors shared the same basic electronic and optical properties [10], it immediately led to the thinking that the DOS of the amorphous semiconductor might be similar to that of its crystalline counterpart and not completely different as it was thought initially. This can be seen in the three popular density of states models proposed shown in Figure 2.2.

One important difference between crystalline and amorphous semiconductors is the existence of localized states in the mobility gap. Unlike the extended states found in the two principal bands, electrons in the localized states are not free to travel anywhere in the material and thus have zero mobility. While some of these localized states are created by defects, the majorities of them are created by the loss of long range order and is unique to solids which are amorphous.
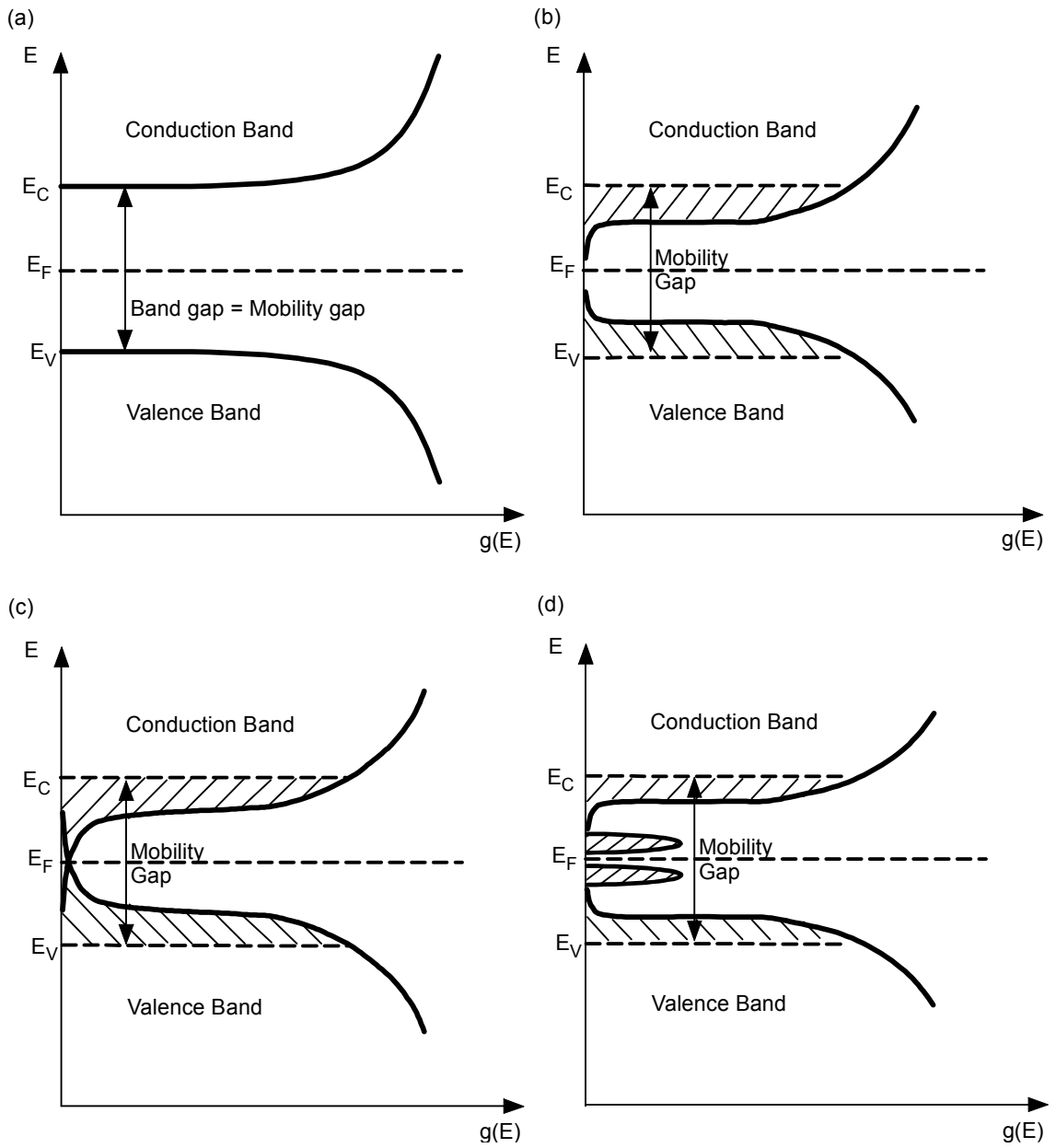
Figure 2.2: (a) DOS of a crystalline semiconductor; (b) DOS models proposed by Mott [11], (c) DOS models proposed by Cohen, Fritzsche and Ovshinski (CFO) [12], and (d) DOS models proposed by Marshall and Owen [13]. The hatched regions denote localized states. Note: the x-axis in all the 4 figures is logarithmic.

2.4 The Optical Properties of Amorphous Semiconductors

In general, the optical properties of a material describe how the characteristics of light are affected when it passes through it. The two most important optical constants are the refractive index n and absorption coefficient α. The refractive index of an optical material or dielectric medium is generally defined as the ratio of the velocity of light c in vacuum to its velocity v in the medium. In materials where an electromagnetic wave can lose its energy during propagation, the refractive index becomes complex. The real part of this complex refractive index N is the refractive index n while the imaginary part is referred to as the extinction coefficient K, which is related to the absorption coefficient α through $K = c\alpha / 2\omega$, where ω is the frequency of interest. While the importance of the absorption coefficient, which dictates how readily photons will be absorbed by the material, can be understood from the viewpoint of a photoconductor, the interest in the refractive index, which ultimately determines the amount of dispersion, is obvious in the engineering of optical waveguides. Although our understanding of these two properties in amorphous semiconductors is limited and not complete, some perspectives on the optical properties of amorphous semiconductor can still be gained from the proposed models.

2.4.1 The Absorption Coefficient

The absorption edge of many amorphous compound semiconductors has the shape that looks like the one depicted in Figure 2.3. There will be a high absorption region A, which is also referred to as the fundamental absorption edge, where the absorption coefficient is $\alpha > 10^4 \text{cm}^{-1}$. An exponential region B, which is usually referred to as the Urbach edge and has values that extend over 4 orders of magnitude of α, and a weak absorption tail C called the Urbach tail. Very often the density of states proposed by different models mentioned previously in Section 2.3 is used to describe optical transitions in semiconductors. The basic difference between models used for crystalline

semiconductors and those used for amorphous semiconductors is the non-conservation of the k-vector momentum. This is due to the change in the character of the wavefunctions, some of which no longer extend over the whole volume of the sample but become localized over a certain volume, *V(E)*. As a result, the transition probabilities between states localized at different sites are reduced by a factor depending on the overlap of the wavefunctions at the initial and final states.
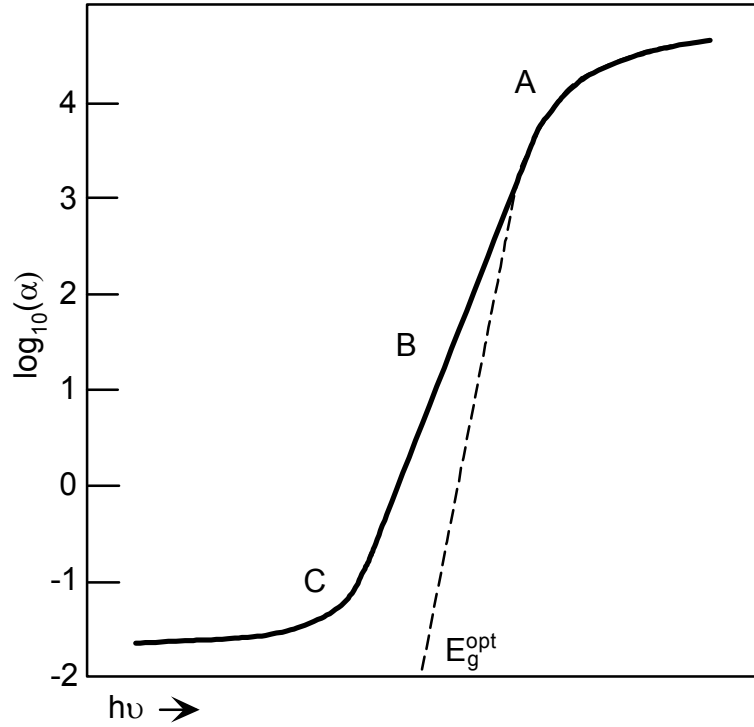
Figure 2.3: Typical absorption edge of an amorphous semiconductor, where A represents a region where $\alpha \geq 10^4 cm^{-1}$, called the fundamental absorption edge, B represents a region changing exponentially, which is referred to as the Urbach edge, and C represents a region referred to as the weak absorption tail or Urbach tail. E_g^{opt} is the optical bandgap [14].

Many semiconducting glasses have been observed to have an absorption, α that has the following frequency dependence in the region where the absorption is high, i.e. region A of Figure 2.3,

$$\alpha \hbar \omega (\omega) = A(\hbar \omega - E_g^{opt})^r, \qquad (\alpha \geq 10^4 cm^{-1}) \qquad 2.1$$

where A and r are some physical constants that depend on the material properties, $\hbar\omega$ is the energy of the photon and E_g^{opt} is a parameter that has been called optical bandgap energy. In many direct bandgap crystalline semiconductors, r has been found to have a value of $r = 2$ and $A = 10^5$ to 10^6 cm^{-1} eV^{-1}. Many amorphous semiconductors also have $r = 2$ (e.g. a-Si:H, As$_2$Se$_3$ etc.) while some complicated glasses have $r = 3$. On the other hand, $r = 1$ for a relatively simple glass, such as a-Se [15, 16].

If the optical transitions were limited to those that are between states of which one is localized and the other extended, and the density of the initial and final states, $g_v(E)$ and $g_c(E)$, can be assume to be,

$$g_v(E) \propto (E_v - E)^{r_1} \text{ and } g_c(E) \propto (E - E_c)^{r_2}, \qquad\qquad 2.2$$

then according to Tauc [15] the absorption in region A is given by,

$$\alpha\hbar\omega = A(\hbar\omega - E_g^{opt})^{r_1+r_2+1}, \qquad\qquad 2.3$$

where A, r_1, and r_2 are physical constants that depend on the material properties, $\hbar\omega$ is the energy of the photon and E_g^{opt} is a parameter that has been called optical bandgap energy. For a solid whose density of states are parabolic, i.e. $g_v(E) \propto (E_v - E)^{1/2}$ and $g_c(E) \propto (E - E_c)^{1/2}$, we thus have,

$$\alpha\hbar\omega(\omega) = A(\hbar\omega - E_g^{opt})^2. \qquad (\alpha \geq 10^4 \text{cm}^{-1}) \qquad\qquad 2.4$$

Many amorphous semiconductors follow the above behavior in Equation (2.4). For example, the optical absorption in a-Si:H and many chalcogenide glasses has been analyzed using Equation (2.4). It is important to emphasize that there are also amorphous semiconductors, such as a-Se, that do not follow the above rule. a-Se is a well known example in which $r \approx 1$. [15, 16]. The table below shows the experimentally determined values of some popular materials using Equation (2.4) [16]. O'Leary has studied the optical absorption in a-Si:H using model DOS functions and calculated the dependence of the joint density of states (and hence the absorption coefficient) on the photon energy [17, 18]. One significant conclusion from his work is that the optical bandgap determined from a typical Tauc plot, Equation (2.4), depends on the spread of

the tail states. The wider the tail spread, the lower is the Eg_T from $E_C - E_V$. In fact, only in the absence of tail states, would $Eg_T = E_C - E_V$.

Table 2-1: The optical bandgap Eg_T and constant A determined experimentally for some amorphous semiconductors using Equation (2.4) [16].

Material	Eg_T(eV)	A(cm^{-1}eV^{-1})
c-Si	1.26	5.2×10^5
a-SiH$_{0.26}$	1.82	4.6×10^5
a-Ge:H	1.05	6.7×10^5
As$_2$S$_3$	2.32	4.0×10^5
As$_2$Se$_3$	1.76	8.3×10^5
As$_2$Te$_3$	0.83	4.7×10^5

In the exponential region B of the absorption edge of Figure 2.3, whose existence was said to be the evidence of the presence of localized states, the absorption coefficient was found to have the following properties. Firstly, it has a frequency dependency of the form: $\alpha(\upsilon) \propto \exp(h\upsilon/\Delta E)$, where ΔE is the energy characterizing the slope. Secondly, at low temperatures, usually below room temperature, the energy ΔE is almost temperature independent and has, in many semiconducting glasses, the value between 0.05eV and 0.08eV. While at high temperatures, ΔE increases with temperature in such a way that $\Delta E \propto T$. Lastly, in many amorphous semiconductors except a-Se, parts A and B of Figure 2.3 move as a whole [19].

In a crystalline semiconductor, similar exponential tails have been observed and these tails are usually referred to as Urbach edges. The theories of the Urbach edge are based on the idea that the sharp absorption edge is broadened by some kind of mechanism. In ionic crystals it is the optical phonons which are responsible for the Urbach edges. Although developed for crystals, the Urbach edge was successfully applied to the temperature dependence of the absorption edge of a-Se shown in Figure 2.4 [19].
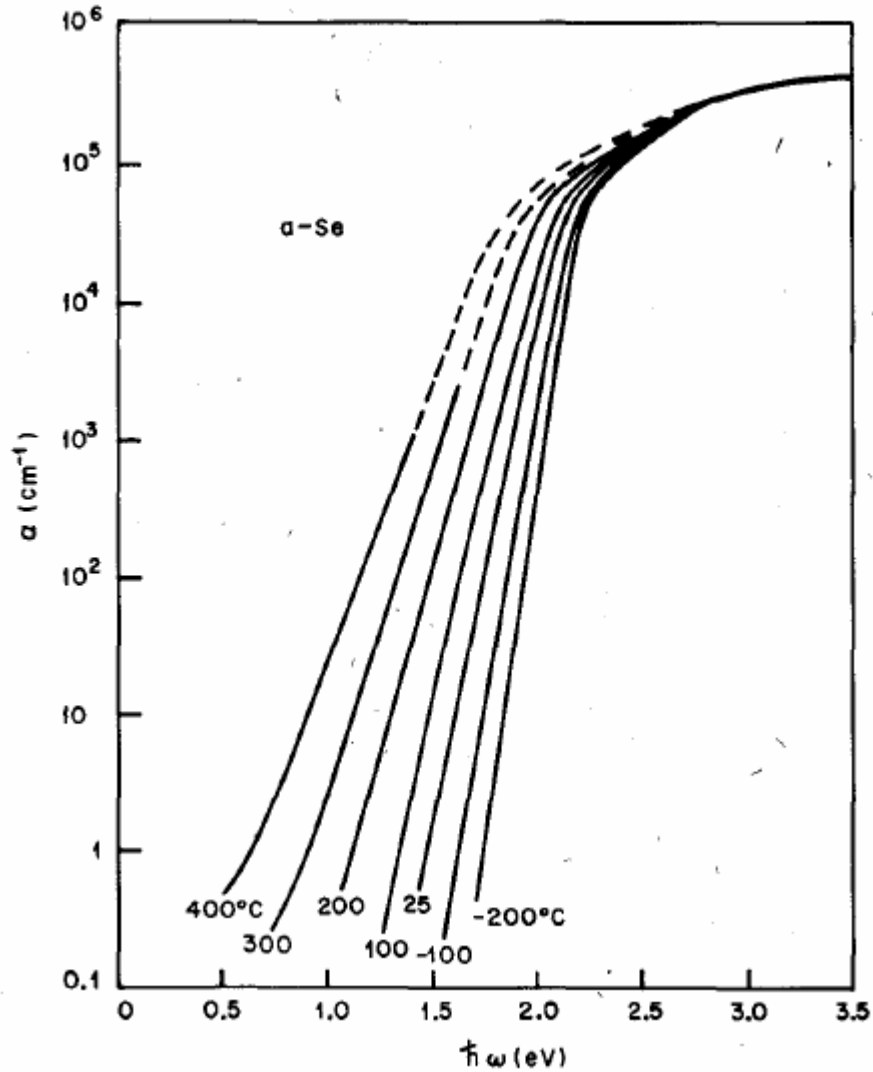
Figure 2.4: The absorption edge of *a*-Se at various temperatures (after [19]).

Other more popular models are based on the interactions with internal electric fields. In these models, the exponential edges are caused by various sources of electric field generated internally. For example, in pure crystals the exponential edges are due to electric fields produced by longitudinal optical phonons while those in compensated semiconductors are due to the electric fields produced by charged impurities. Besides optical phonons and charged impurities, there are also other possible sources of internal electric fields. One of them is the density fluctuations via the piezoelectric effect in semiconductors with a piezoelectric constant different from zero. In an amorphous solid, these density fluctuations do not change with time, and so the exponential edge can be

19

thought of as due to frozen-in longitudinal optical phonons. These theories may have a general applicability and interested readers can find out more detail in the reference [19].
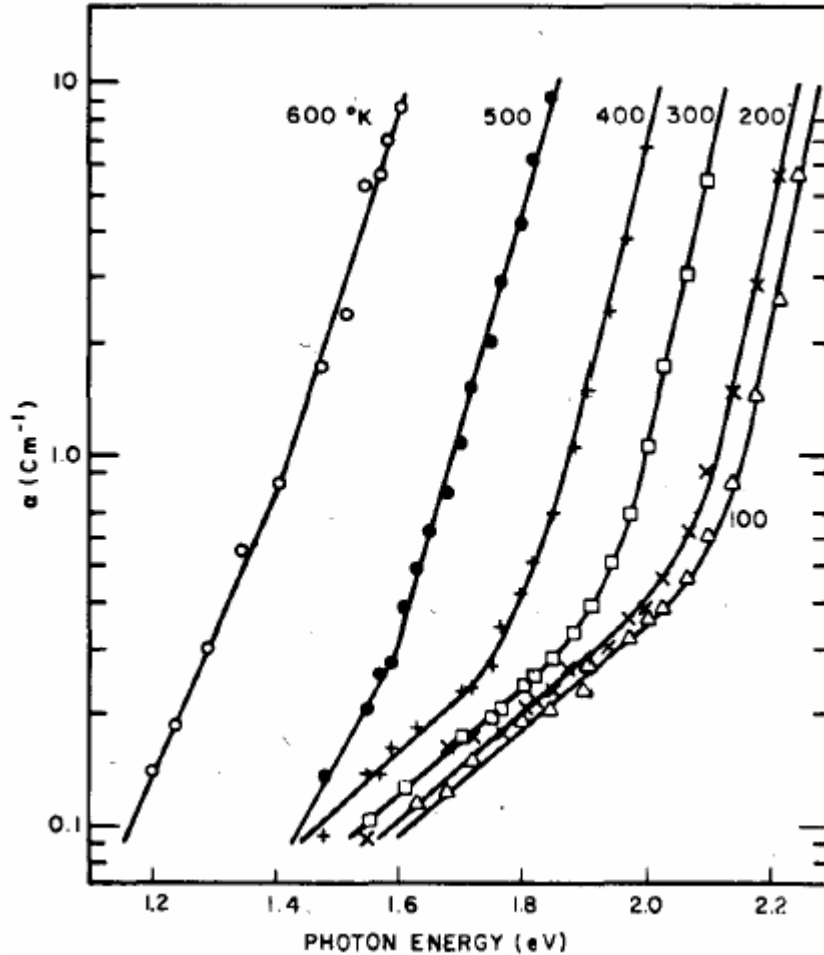
Figure 2.5: The absorption edge of a-As$_2$S$_3$, at low absorption levels at various temperatures (after [20]).

Of the three absorption regions in Figure 2.3, part C is the most difficult to study. This is because absorption at such low levels may only be apparent or false due to the possibility that it might be light scattering or simply noise in the system. This absorption tail lies below the exponential part of the absorption edge B and its strength and shape were found to depend on the preparation, purity and thermal history of the material, and vary very little with its thickness.

Nevertheless it is still possible to study the optical transition in this region if the sample is properly prepared. This can be seen when light scattering had been experimentally tested on the sample with an absorption tail shown in Figure 2.5. In this experiment, the attenuation that is due to scattering was found to be $\alpha_{scatter} \approx 0.04 cm^{-1}$ for a sample that was free of large macroscopic inhomogeneities. This is about an order of magnitude lower than the absorption level in the region of the weak absorption tail, as can be seen in Figure 2.5. Similar results were also observed for other chalcogenide glasses [20].

There are two possible forms of optical transitions in this region that are considered to be most probable. First, the optical transitions may be of the kind that corresponds to electron transitions from an impurity ion to an ion of the host lattice, or vice versa, that is the initial and final states are localized at different centers. Although one has observed formulations of similar tails in crystals, it has not been studied quantitatively. Second, the optical transitions may be of the kind that is similar to what was suggested for the exponential region B of the absorption edge in Figure 2.3. This is to say that the initial state is localized and the final state is extended, or vice versa. According to Tauc [20], there is evidence of correlation effects in this region, which reduces the effective optical cross-sections for transitions from localized states into delocalized states in glasses relative to the corresponding case in crystals. In other words, due to the internal potential fluctuations in glasses, the extended states close to the band gap exist only in a part of the sample and not at every site of the centers. It was suggested that because of this effect, glasses are more transparent below the absorption edge than crystals with the same content of impurities [20].

2.4.2 Index of Refraction

As mentioned earlier, the refractive index n of an optical or dielectric medium is defined as $n = c/v$, where c is the velocity of light in vacuum and v is the velocity in the medium. In a lossy material, this refractive index becomes complex and can be expressed as

$$N = n - jK,$$

2.5

where N is the complex refractive index, n is the refractive index and K is the extinction coefficient.

The optical constants, n and K can be determined by measuring the reflectance from the surface of a material as a function of polarization and the angle of incidence. For normal incidence, the reflection coefficient, r, is obtained as

$$r = \frac{1-N}{1+N} = \frac{1-n+jK}{1+n-jK},$$

2.6

and thus the reflectance R is,

$$R = |r|^2 = \left|\frac{1-n+jK}{1+n-jK}\right|^2 = \frac{(1-n)^2 + K^2}{(1+n)^2 + K^2}.$$

2.7

So by fitting this equation to the measured reflectance R at normal incidence, the optical constants, n and K can be calculated [21].

The refractive index, n is also related to the relative permittivity through an equation derived from the Maxwell's equations, which is $n = \sqrt{\varepsilon_r \mu_r}$, where ε_r is the static dielectric constant or relative permittivity and μ_r is the relative magnetic permeability. This equation associates the dielectric properties of a material to its optical properties.

For a lossy nonmagnetic medium, where $\mu_r = 1$, both its refractive index and relative permittivity will have an imaginary component that represent the attenuation. If the complex static dielectric constant is given by

$$\varepsilon_r = \varepsilon_r' - j\varepsilon_r'',$$

2.8

where ε_r' and ε_r'' are just the real and imaginary part of the complex permittivity respectively, then from $N = \sqrt{\varepsilon_r \mu_r}$, it will become $n - jK = \sqrt{\varepsilon_r' - j\varepsilon_r''}$, and thus either

$$n^2 - K^2 = \varepsilon_r',$$

2.9

$$2nK = \varepsilon_r''$$

2.10

or

$$n = (1/\sqrt{2})[\sqrt{\varepsilon_r'^2 + \varepsilon_r''^2} + \varepsilon_r']^{1/2},$$ 2.11

$$K = (1/\sqrt{2})[\sqrt{\varepsilon_r'^2 + \varepsilon_r''^2} - \varepsilon_r']^{1/2}.$$ 2.12

Figure 2.6 shows the complex relative permittivity and the complex refractive index of crystalline silicon in terms of the photon energy, $h\upsilon$. For photon energies below the bandgap energy (1.1eV), both ε_r'' and K are negligible and n is close to 3.7. They increase and change strongly as the photon energy becomes greater than 3eV, which is far beyond the bandgap energy. Notice that both ε_r' and n peak at $h\upsilon \approx 3.5eV$, which corresponds to a direct photoexcitation process [21].
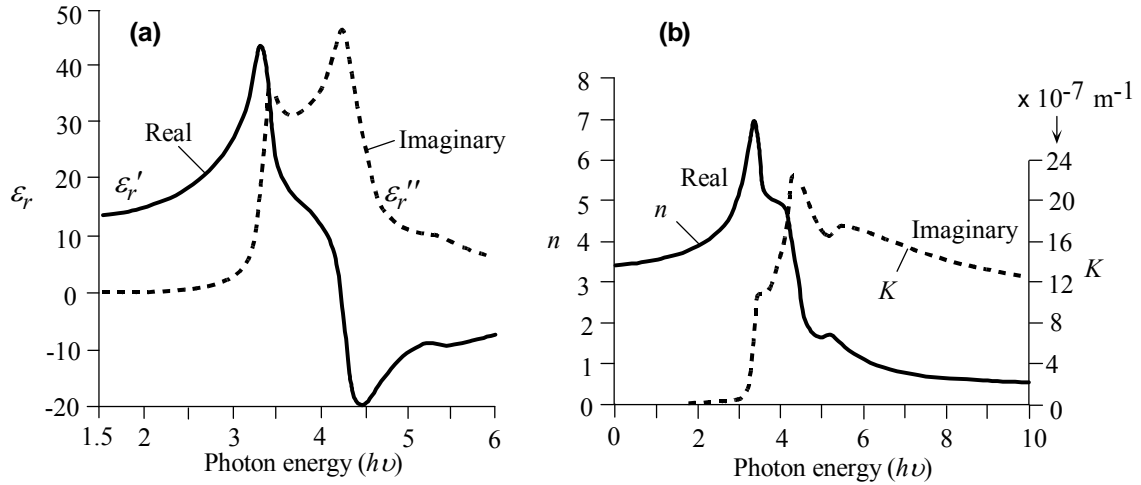
Figure 2.6: (a) Complex relative permittivity of a silicon crystal as a function of photon energy plotted in terms of the real (ε_r') and imaginary (ε_r'') parts. (b) The optical properties of a silicon crystal vs. photon energy in terms of the real (n) and imaginary (K) parts of the complex refractive index [21].

The above Equations (2.9) and (2.10) and (2.11) and (2.12) relate the complex relative permittivity of the material to its index of refraction regardless of the mechanism of loss. Since the optical properties of materials are typically presented either by showing the frequency dependencies of n and K or ε_r' and ε_r'', a link to the complex permittivity allows us to relate macroscopic optical properties, like n and K to a microscopic properties such as electronic polarizability, α_e. This can be done through a model used

for the study of dielectric dispersion in material. The model is based on a single oscillator, in which the electric field of the incident EM wave induces dipole oscillations in the material with a single resonant frequency ω_o, in such a way that

$$\varepsilon_r' = 1 + \frac{N_{at}}{\varepsilon_o}\alpha_e' \text{ and } \varepsilon_r'' = 1 + \frac{N_{at}}{\varepsilon_o}\alpha_e'', \qquad 2.13$$

where N_{at} is the number of atoms per unit volume, ε_o is the permittivity of free space, and α_e' and α_e'' are the real and imaginary parts of the electronic polarizability, given respectively by:

$$\alpha_e' = \alpha_{eo}\frac{1-(\omega/\omega_o)^2}{[1-(\omega/\omega_o)^2]^2 + (\gamma/\omega_o)^2(\omega/\omega_o)^2} \qquad 2.14$$

and

$$\alpha_e'' = \alpha_{eo}\frac{(\gamma/\omega_o)(\omega/\omega_o)}{[1-(\omega/\omega_o)^2]^2 + (\gamma/\omega_o)^2(\omega/\omega_o)^2}, \qquad 2.15$$

where α_{eo} is the DC polarizability corresponding to $\omega = 0$ and γ is the loss coefficient that characterizes the attenuation of the EM wave within the material system [21].

There are several popular models or equations describing the spectral dependence of refractive index n in a material. Such dispersion relationships are essential in designing photonic devices, such as waveguides. In the *Cauchy* equation, the dispersion relationship is commonly described as follows:

$$n = A + \frac{B}{\lambda^2} + \frac{C}{\lambda^4}, \qquad 2.16$$

where A, B and C are material dependent constants determined through curve fittings, n is the refractive index and λ is the wavelength. It is typically used in the visible spectrum region for various optical glasses. Besides Cauchy's dispersion model, there is also the *Sellmeier* equation, which is an empirical formula made up of a series of lossless single dipole *Lorentz* oscillator terms, each of which having the same wavelength dependence of the type $\lambda^2/(\lambda^2 - \lambda_i^2)$ with different strengths, i.e.

$$n^2 = 1 + \frac{A_1\lambda^2}{\lambda^2 - \lambda_1^2} + \frac{A_2\lambda^2}{\lambda^2 - \lambda_2^2} + \frac{A_3\lambda^2}{\lambda^2 - \lambda_3^2} + ..., \qquad 2.17$$

where the *Sellmeier coefficients*, A_i and λ_i, with integer $i = 1,2,3,\ldots$, are determined through curve fitting. Since any number of resonance type or oscillator terms can be summed together to get as wide a range of wavelength dependence as possible with this model, it is the most popular dispersion relation. Its main drawback is that it does not accurately represent the refractive index when there is a contribution arising from free carriers in narrow bandgap or doped semiconductors [21].

Another model that is based on the single oscillator is the *Wemple-DiDominico* equation. It is a semi-empirical dispersion relation for determining the refractive index at photon energies below the inter-band absorption edge. It is expressed as:

$$n^2 = 1 + \frac{E_o E_d}{E_o^2 - (h\upsilon)^2}, \qquad\qquad 2.18$$

where υ is the frequency, h is the Planck constant, E_o is the single oscillator energy and E_d is the dispersion energy which measures the average strength of inter-band optical transitions. It is given by $E_d = \beta N_c Z_a N_e$ (eV), where N_c is the effective coordination number of the cation nearest-neighbor to the anion, Z_a is the formal chemical valency of the anion, N_e is the effective number of valence electrons per anion excluding the cores, and β is a two-valued constant that depends on whether the inter-atomic bond is ionic or covalent ($\beta_i = 0.26 \pm 0.03$eV and $\beta_c = 0.37 \pm 0.04$eV respectively). It was said that E_d (corrected for differences in densities) depends on the short range order only and is the same in the crystalline and amorphous forms if the short-range order (the first coordination number) is the same. Further, empirically, $E_o = CE_g(D)$, where $E_g(D)$ is the lowest direct bandgap and C is a constant, typically $C \approx 1.5$. It has been associated with the main peak in the $\varepsilon_r''(h\upsilon)$ versus $h\upsilon$ spectrum [22].

The refractive index of a semiconductor (typically for $h\upsilon < E_g$) usually decreases with increasing energy bandgap E_g. There are various empirical and semi-empirical rules and expressions that relate n to E_g. In the *Hervé-Vandamme* relationship [23],

$$n^2 = 1 + \left(\frac{A}{E_g + B}\right)^2, \qquad\qquad 2.19$$

where A and B are constants, typically $A \approx 13.6\text{eV}$ and $B \approx 3.4\text{eV}$. The temperature dependence of n arises from the variation of E_g with temperature T and typically increases with increasing temperature. The temperature coefficient of refractive index (*TCRI*) of semiconductors can be found from the *Hervé-Vandamme* relationship as:

$$TCRI = \frac{1}{n} \cdot \frac{dn}{dT} = \frac{(n^2-1)^{3/2}}{13.6n^2} \left[\frac{dE_g}{dT} + \frac{dB}{dT} \right].$$ 2.20

where $dB/dT \approx 2.5 \times 10^{-5}\text{eVK}^{-1}$. TCRI is typically found to be in the range of 10^{-6} to 10^{-4} K^{-1} [21].

The electronic polarizability of solids, α_e is proportional to the real part of the dielectric constant ε_r', and is interconnected with absorption, α through the imaginary part of the dielectric constant ε_r'', by the *Kramers-Kronig* dispersion relation:

$$\varepsilon_r'(\omega) = 1 + \frac{2}{\pi} P \int\limits_0^\infty \frac{\omega' \varepsilon_r''(\omega')}{\omega'^2 - \omega^2} d\omega',$$ 2.21

$$\varepsilon_r''(\omega) = \frac{2\omega}{\pi} P \int\limits_0^\infty \frac{\varepsilon_r'(\omega')}{\omega'^2 - \omega^2} d\omega',$$ 2.22

where ω is the frequency of interest, ω' is the integration variable and P represents the *Cauchy* principal value of the integral, which ensures that the singularity at $\omega = \omega'$ is avoided. The relationship was deduced under very general conditions and is valid for amorphous materials and liquids as well as for crystals. It only requires that the material have a relative permittivity that is independent of the applied field [21, 24]. The refraction index at zero frequency is a useful parameter that is sometimes used to describe the characteristics of amorphous solids. This is because large changes in the index of refraction are very often an indication of some differences in the bonding and thus, the structure and the polarizability of the material. The refraction index at zero frequency is related to the *Kramers-Kronig* dispersion relation in the following way. From Equation (2.23), at $\omega = 0$, $\varepsilon_r''(0) = 0$. Since $n \geq 1$, because nothing can travel faster than the speed of light, from Equations (2.10 and 2.11), $K = 0$ and $n^2 = \varepsilon_r'$. In other words, the electronic part of the refraction index at zero frequency will be,

$$n_o^{\,2} = n^2(0) = \varepsilon_r'(0) = 1 + \frac{2}{\pi} P \int_0^\infty \frac{\varepsilon_r''(\omega')}{\omega'} d\omega' \,,$$ 2.23

or

$$n_o^{\,2} = 1 + \frac{2}{\pi} P \int_0^\infty \omega \varepsilon_r''(\omega) d\omega \,.$$ 2.24

In crystalline semiconductors, such as Ge, Si, and the III-V compounds, the refractive index at zero frequency, $n_o(\text{c-Ge}) = 4.01$, $n_o(\text{c-Si}) = 3.42$, and $n_o(\text{c-GaAs}) = 3.28$, is typically a little bit larger in the amorphous state than in the crystalline state, $n_o\,(a\text{-Ge}) = 4.05$, $n_o(a\text{-Si}) = 3.50$, and $n_o(a\text{-GaAs}) = 3.60$. However, the change is not only in the opposite direction for Se but also larger, $n_o(c\text{-Se}_{//}) = 3.41$, $n_o(c\text{-Se}_\perp) = 2.64$ and $n_o(a\text{-Se}) = 2.50$, where $n_o(c\text{-Se}_{//})$ is measured with the light polarization parallel to the c-axis or the <001> direction of the hexagonal lattice of the trigonal crystalline Se and $n_o(c\text{-Se}_\perp)$ is measured with the light polarization perpendicular to the c-axis or the <001> direction of the hexagonal lattice of the trigonal crystalline Se [24]. This significant decrease in n_o in a-Se is associated with the large shift of the absorption spectrum towards higher energies. Figure 2.7 shows the fundamental absorption bands of Se determined from both the measurements of the reflectivity at normal incidence and the use of *Kramers-Kronig* analysis.
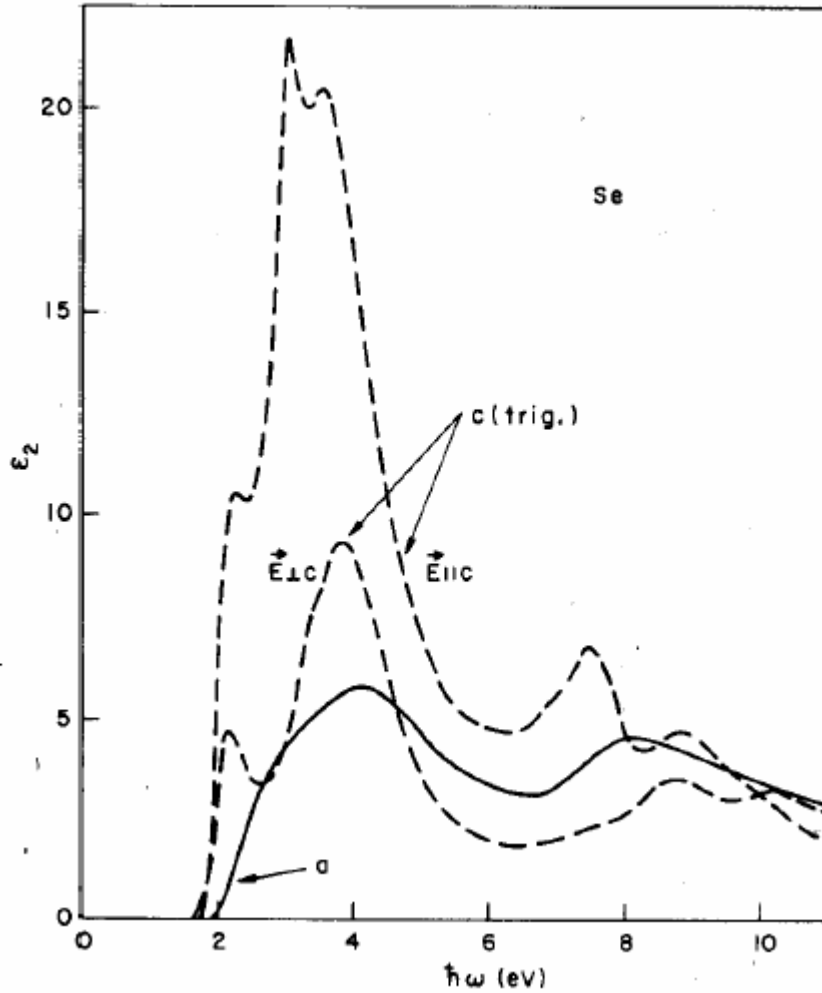
Figure 2.7: Fundamental absorption band of *a*-Se, and crystalline Se for 2 directions of light polarization. The light polarization is either parallel or perpendicular to the *c*-axis, which is the <001> direction of the hexagonal lattice of the trigonal crystalline Se. The shift in the absorption is said to be due to the decreased interaction between the chains in the disordered structures (after [24]).

From various studies done on the bonding differences between the amorphous and crystalline Ge chalcogenides and other materials, it appears that unlike the large shifts in n_o observed when there are changes in the bonding around the first and second nearest neighbor region, the loss of long-range order alone changes n_o by only a little. Although the value of n_o in bulk amorphous materials is reproducible, it is not so in films due to the dependence of n_o on the preparation conditions and thermal history. There is a formula that relates the changes in the refraction index of a crystal at zero frequency to

its density ρ, the nearest neighbor distance d, and the fraction s of the dangling bonds. This equation can also be used to estimate the large shift in n_0 that is due to the changes in the short range order in amorphous material and is done through the real part of the dielectric constant ε'_r as shown below [24]:

$$\frac{\varepsilon'_{r\,\text{film}}(0)-1}{\varepsilon'_{r\,\text{crystal}}(0)-1} = \frac{1}{(1-s)^2}\frac{\rho_{\text{film}}}{\rho_{\text{crystal}}}\left(\frac{d_{\text{film}}}{d_{\text{crystal}}}\right)^5 .$$

2.25

2.5 The Physical Structure of Amorphous Selenium

Now that a basic understanding of the amorphous solid has been reached, it will be appropriate to start with the physical structure of amorphous selenium. For a long time, the structure of amorphous selenium was believed to contain a random mix of selenium chains (Se_n) and 8-ring structures (Se_8) distributed randomly throughout the solid. This is probably because crystalline selenium can exist in either the α-monoclinic (α-Se) form that contains the 8-ring structures or the trigonal (γ-Se) form that contains the selenium chain. However, recent structural studies on selenium and its alloys favor a "random chain model", in which all the atoms are in a twofold coordinated chain structure and not random. The dihedral angle ϕ, which is defined as the angle between two adjacent bonding planes as illustrated in Figure 2.8, is constant in magnitude but changes in sign randomly [25, 26].

The "random chain model", which assumes only local molecular order within a selenium chain like the one shown in Figure 2.9, has been successfully used to explain the vibrational spectra of a-Se. It accounts for the presence of various 8-ring structures Se_8-like spectral features in the infrared absorption and Raman scattering spectra without invoking a random mixture of selenium chains Se_n and 8-ring structures Se_8 members for the structure.
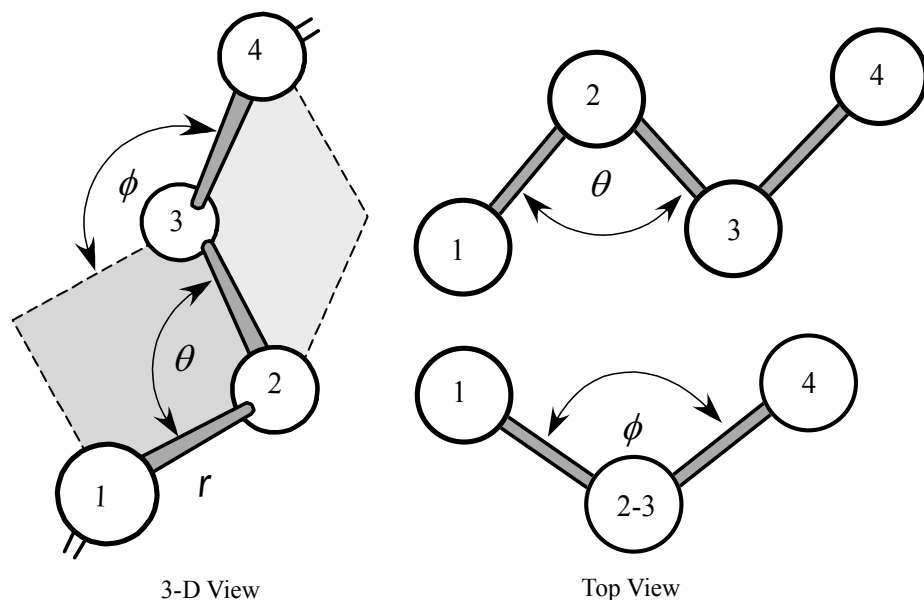
Figure 2.8: *a*-Se chain molecules and the definition of the dihedral angle. The dihedral angle is defined as the angle ϕ between two adjacent bonding planes. It is observed looking down the bond joining atoms 2 & 3 just like the diagram on the right.
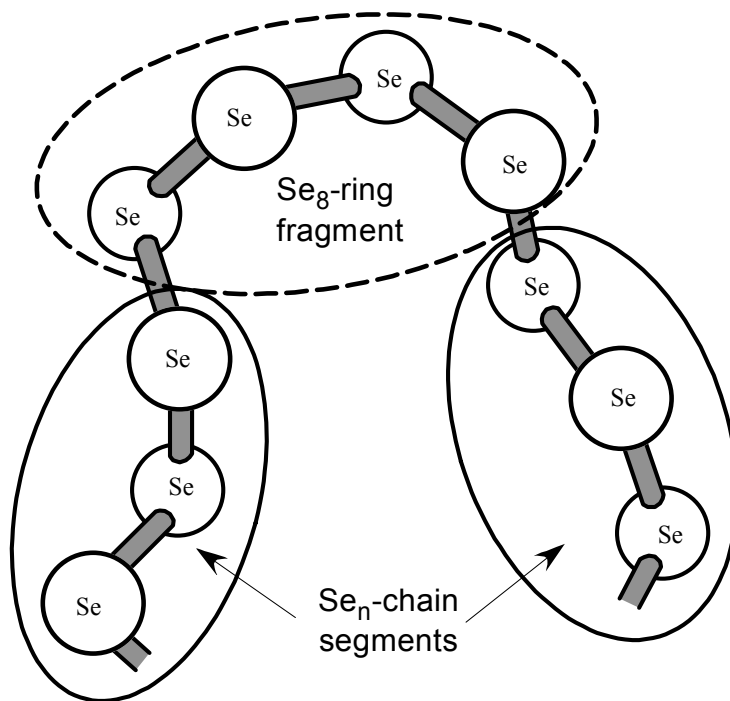
Figure 2.9: Local molecular order in a selenium chain in which there are segments characterized by the repetition of the same dihedral angle ("chain-like" in the sense of trigonal Se) and segments characterized by the alternating dihedral angles ("ring-like" in the sense of Se_8 molecules).

In the trigonal crystalline form (γ-Se), the dihedral angle rotates in the same sense as in moving along the chain to give a spiral pitch of three atoms, whereas in the α-monoclinic crystalline form (α-Se), the change in the sign of the dihedral angle alternates when moving around the ring. Thus in an amorphous selenium solid, depending on a particular sequence of ϕ, the change in the sign of the dihedral angle, ϕ will either lead to regions that are ring-like or to regions that are chain-like. If the symbol + or – is used to indicate the relative phase of the dihedral angles between the adjacent bonding planes, then a region will be termed ring-like when the relative phase of the dihedral angles was a sequence of the type $+ - + -$ and a region termed chain-like when the sequence is of the type $+ + +$ or $- - -$ [25]. Using these symbols, the "random chain model" shown in 2.10, can be characterized as $+ + + - + - + - - -$. There were also other structural studies of a-Se which support the random chain model and they can be found in the literature [27, 28].

Another characteristic of amorphous selenium is the presence of some thermodynamically derived charged structural defects, called the valence alternation pairs (VAP). This important feature is common in nearly all the chalcogenide glasses and it corresponds to some of the chalcogen atoms being under-coordinated and over-coordinated [29, 30, 31]. These defects arise because it is energetically more favorable to form a diamagnetic pair of over-coordinated and under-coordinated chalcogenide charged centers, like Se_1^- and Se_3^+, than to form a paramagnetic singly or triply coordinated defects, like Se_1^0 and Se_3^0. The pair of charged centers, Se_1^- and Se_3^+, is believed to be the lowest energy structural defect in an a-Se because of an absence of electron spin resonance (ESR) signal in amorphous selenium. The lack of ESR signal implies that any low energy structural defects in these glasses would not have any dangling bonds and so must be charged centers that have their electrons paired [32,33]. As a result, a neutral Se atom with a dangling bond Se_1^0 will want to lower its energy by approaching the lone pair on a normally coordinated Se_2^0 atom to form a pair of charged centers, Se_1^- and Se_3^+, termed valence alternation pair (VAP). If the atoms of the pair of charged centers are in close proximity, they are also called an intimate valence

alternation pair (IVAP). The reaction $Se_1^0 + Se_2^0 \rightarrow Se_1^- + Se_3^+$ will be exothermic because some lone pair electrons have been absorbed into dative bonding. A schematic representation of a typical *a*-Se structure with VAP and IVAP centers that illustrates the nature of the lowest energy defects in chalcogen glasses can be found in Figure 2.10.
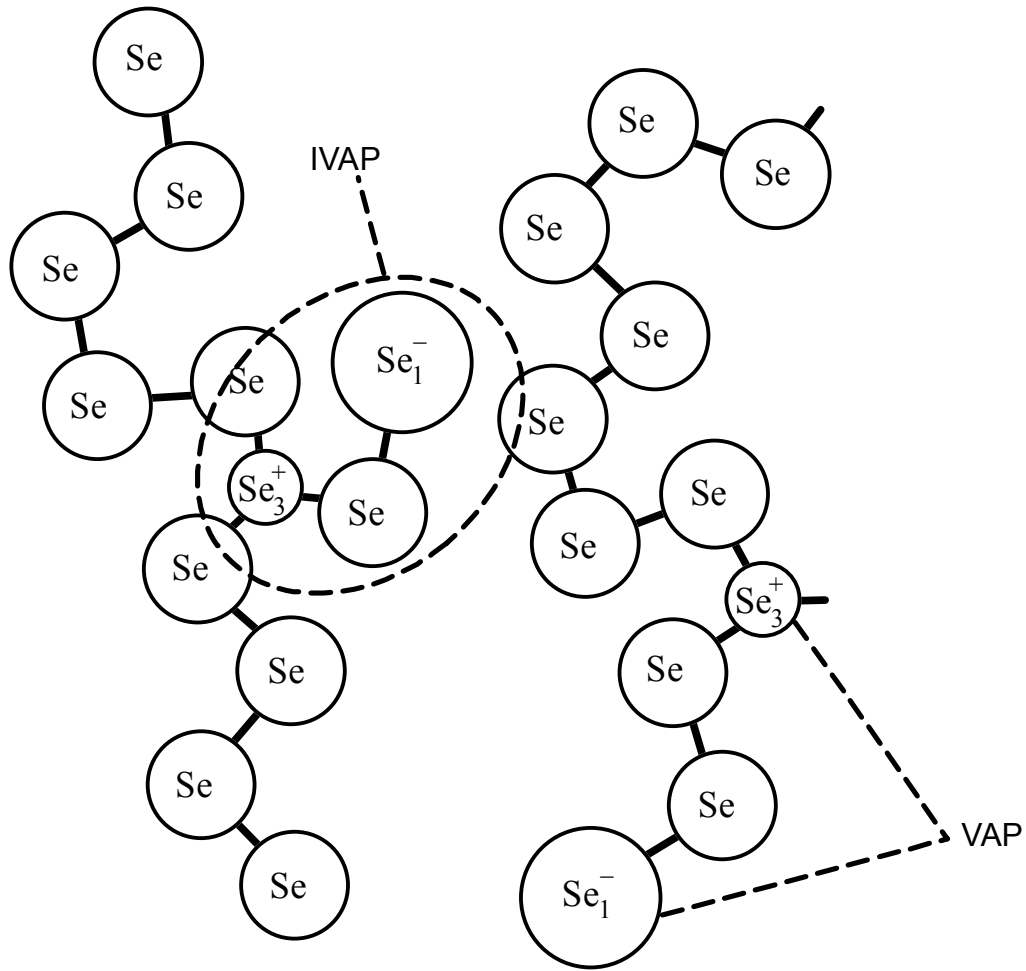
Figure 2.10: Schematic illustration of the *a*-Se structure showing valence alternation pair (VAP) and intimate valence alternation pair (IVAP) defects: Se_1^- and Se_3^+.

The concepts of VAP or IVAP centers and inter-conversions between the diamagnetic charged centers and the paramagnetic defects have been used to explain qualitatively many photoelectric properties of *a*-Se and its alloys. The physics of such processes has been extensively discussed in the literature [34,35,36]. Their existence and the possible defect reactions that can occur in the structure have led to many important predictions

and provided much insight into the behavior of chalcogenide semiconductors. For example, the linear dependence of the steady state photoconductivity on the light intensity for a-Se has been interpreted via photoinduced IVAP-type centers [37].

2.6 Band Model of Amorphous Selenium

According to band theory, the density of states (DOS) diagram is the key to understanding the electrical and optical properties of an amorphous semiconductor. Presently, the accepted model for a-Se is as shown in Figure 2.11 and was developed through various transient photoconductivity and electro-photographic measurements of cycled-up residual and dark discharge [38,39,40,41]. While the energy distribution of the deep localized hole states, with a peak around 0.85eV, was measured using cycled time-of-flight experiments [42], the near-exponentially decaying shallow trap densities, with discrete manifolds at certain energies near the transport bands, was determined from pico-second-resolution transient photoconductivity experiments using the microwave stripline technique [43].

There is experimental evidence that the localized states, both shallow and deep in the mobility gap, are the result of various structural defects and they are thermodynamically stable at room temperature [44]. The concentration of deep traps is known to depend on alloying, doping, and aging, while the exact nature of the shallow traps has not been conclusively determined. However, the shallow traps at around approximately 0.28eV above E_V and 0.35eV below E_C are known to be native defects and their high concentration essentially enable them to control the hole and electron drift mobility within a-Se [45,46,47].
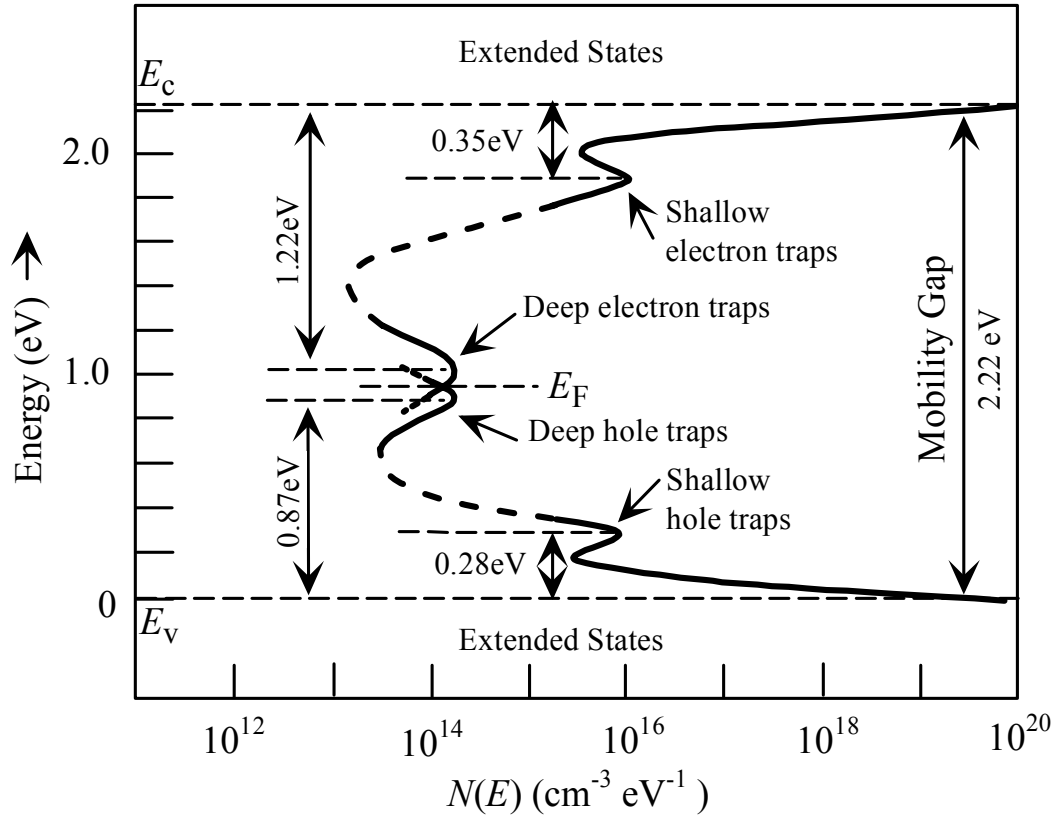
Figure 2.11: Density of states function *N(E)* for *a*-Se. *N(E) is* derived from various optical, time-of-flight, and xerographic measurements [38].

Unfortunately, even though *a*-Se has been extensively studied over many years, there are still various uncertainties and controversies in its density of states function [38,48, 49,50,51,52,53]. Figure 2.12 shows a DOS [53] that is different from the one in Figure 2.11. First of all, there is now a secondary smaller peak at around 0.50eV below E_C. Secondly, the peak that is approximately 0.28eV above E_V in Figure 2.11 is now approximately 0.45eV above E_V. There is also new evidence that points to a drift mobility of holes, μ_h that is controlled by a monotonically decreasing distribution of tail states. This implies that the thermally activated hole drift mobility, μ_h is dependant on the applied electric field. On the contrary, the electron drift mobility was found to be relatively field-independent. Two different peaks have been shown in Figure 2.12 for electron and hole traps above and below the Fermi energy, E_F based on the discharge of the saturated cycled-up xerographic potential [54] and cycled time-of-flight experiments [55].
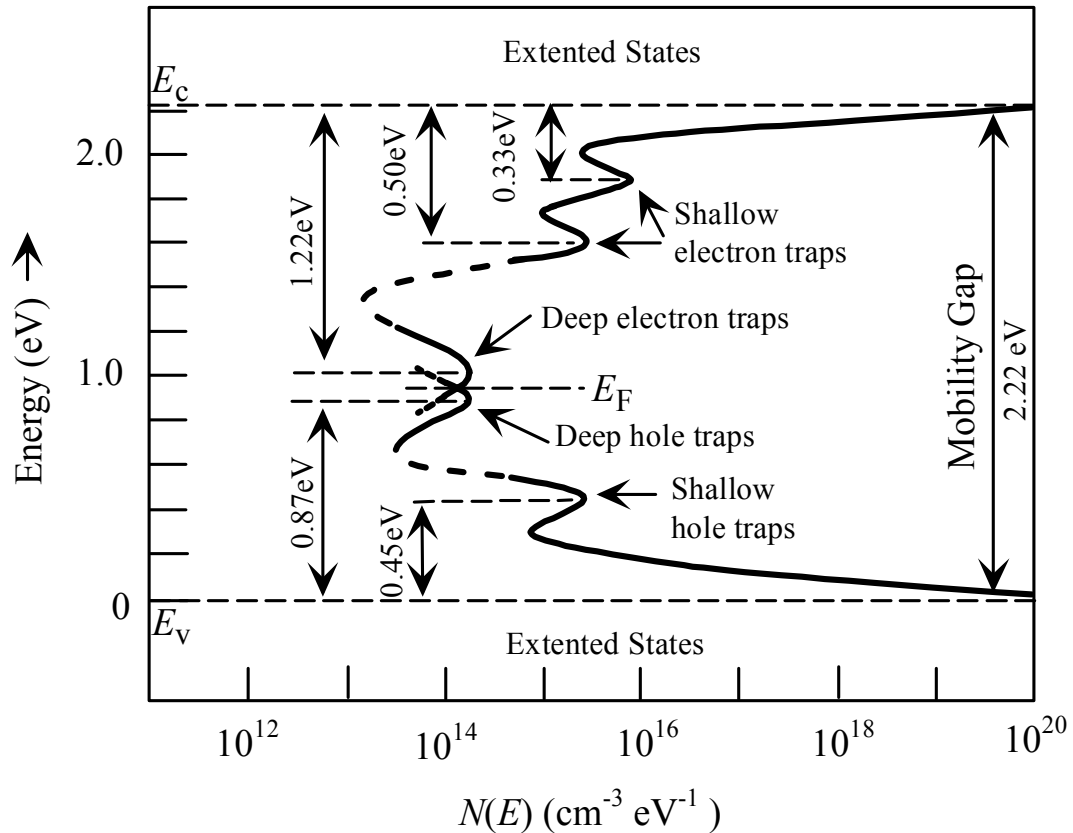
Figure 2.12: A tentative schematic diagram for the density of states of *a*-Se developed recently by the materials group at the University of Saskatchewan [53].

2.7 Electrical Properties of Amorphous Selenium

In a semiconductor such as *a*-Se, the localized states play an important role in conduction and can be investigated by a time-of-flight experiment. The virtue of the time–of–flight (TOF) transient photoconductivity (TP) technique, or TOFTP, measurement lies in its ability to monitor the motion of charge carriers and provides direct evidence of whether the photoinjected charges are making it across a photoreceptor film. The localized states in the *a*-Se act like trap centers that remove charge carriers from conduction, either temporarily by the shallow traps or permanently by the deep traps. These trapping actions result in lower effective drift mobility for both the holes and electrons in the material, which are approximately $\sim 10^{-1}$ cm^2/Vs for holes and $\sim 10^{-3}$ cm^2/Vs for electrons. To put things into perspective, the average drift mobility

in a crystalline semiconductor is of the order of ~10^3 cm^2/Vs, which is a million times higher than those in *a*-Se [56]. Figure 2.13 shows how the nature of charge transport in *a*-Se alloys can be studied from the TOF measurement. The impurity effects in *a*-Se have been well documented and several TOF measurements were successful in identifying the drastic effects of various impurities and alloying elements on the nature of charge transport in *a*-Se. For example, it was shown that when a halogen, even in the range of parts per million, was added to *a*-Se, it would introduce sufficient concentration of electron traps to slow down electron transport. On the other hand, the same halogenation effect was not observed on hole transport in *a*-Se. In fact, halogenation has been reported to improve the hole lifetime [57]. Other than the TOFTP technique, there is also the interrupted field time-of-flight (IFTOF) measurement, which is used to study the nature of trapping and release kinetics in the material at any location.
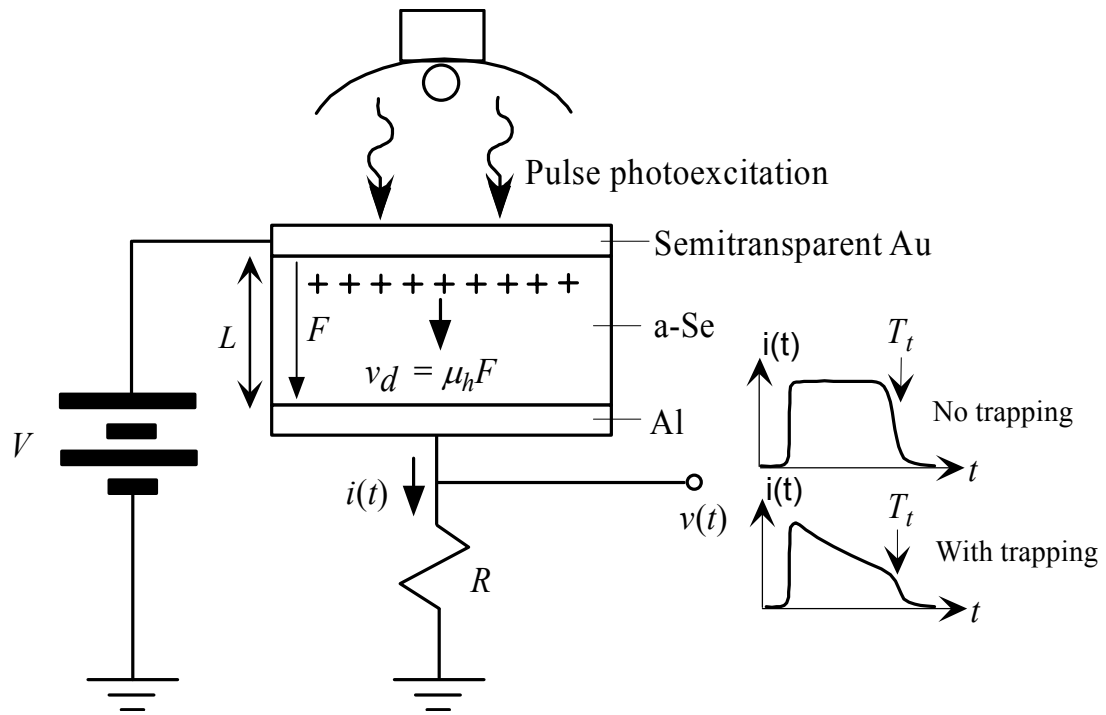
Figure 2.13: Schematic diagram illustrating the principle of the time-of-flight (TOF) measurements. The top electrode is semitransparent. Following pulse photoexcitation, electron-hole pairs are generated within an absorption depth of $1/\alpha(\lambda) << L$. As the holes drift across the sample, they generate an external photocurrent $i(t)$. The shape of the photocurrent $i(t)$ depends on the nature of trapping within the solid. The transit time of the photoinjected holes across the sample thickness L is given by $T_t = L/v_d$, where $v_d = \mu_h F$ is the drift velocity, μ_h is the hole drift mobility, and F is the electric field (V/L) [58].

2.8 Optoelectronic Properties of Amorphous Selenium

The optical absorption coefficient of *a*-Se at around the fundamental absorption edge where $\alpha \geq 10^4 \text{cm}^{-1}$, was found to obey the relationship: $(\alpha h\upsilon) \sim (h\upsilon - E_g)$, where $E_g \approx$ 2.05eV is the optical bandgap at room temperature. A frequency dependence following *Tauc's* law: $(\alpha h\upsilon) \sim (h\upsilon - E_g)^2$ has also been found with an optical bandgap $E_g \approx 1.9 \text{eV}$. This kind of behavior at higher photon energies has been attributed to a sharp rise in the density of states at the band edges. However, the above mentioned behavior starts to disappear when the photon energy is in the Urbach edge. In this region where $\alpha < 10^4 \text{cm}^{-1}$, the absorption coefficient behaves differently and follows the relationship $\alpha = (7.35 \times 10^{-12}) \exp(h\upsilon / 0.058) \text{ eVcm}^{-1}$. This was derived using the Urbach's model originally designed for crystalline semiconductors. A full absorption spectrum of a typical *a*-Se sample can be found in Figure 2.4.

Figure 2.14 shows the dependence of the absorption coefficient, α and the quantum efficiency, η which is defined as the number of electron hole pairs collected per absorbed photon, on the photon energy $h\upsilon$. It is clear that the quantum efficiency only reaches an acceptable value for device applications at high electric fields and photon energies above the fundamental edge. Although the absorption coefficient indicates considerable absorption at photon energies above 2.0eV, the quantum efficiency demonstrates a strong field and photon energy dependence even above the fundamental band edge at $\alpha = 10^4 \text{cm}^{-1}$. The mechanism for the field-dependent quantum efficiency observed for *a*-Se is common to other molecular solids and can be explained by the dissociation of an electron-hole pair. In essence, the theory calculates the probability that an electron-hole pair will diffuse apart under the action of an applied electric field.

According to the dissociation theory, quantum efficiency depends on the applied electric field, F the temperature, T and the initial separation of the photogenerated electron-hole pair or the thermalization length, r_o. It is given by

$$\eta = \eta_0 f(F, T, r_0),$$
2.26

where $f(F, T, r_o)$ is the probability that the electron-hole pair will separate and $\eta_0(h\upsilon)$ is the quantum efficiency of the intrinsic photogeneration processes [57].
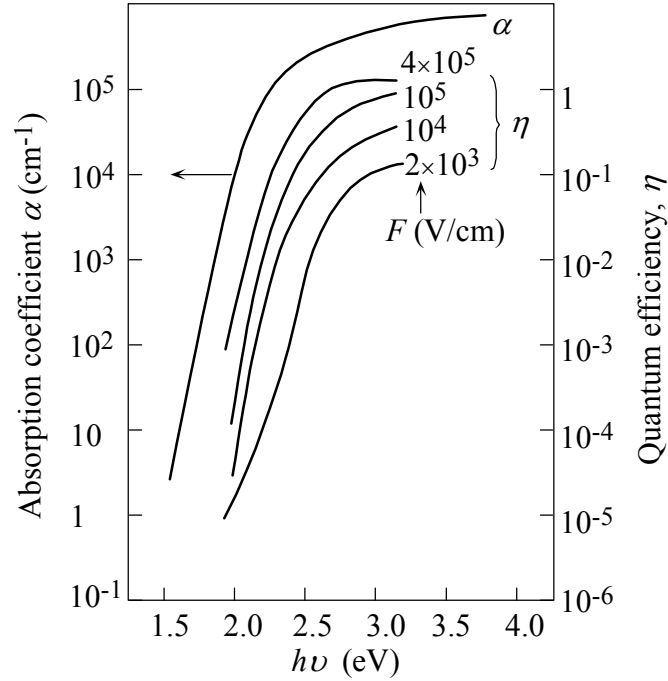
Figure 2.14: The absorption coefficient α, and the quantum efficiency η, as a function of incident photon energy $h\upsilon$, at various applied electric fields, F [57].

The field and photon energy dependence of the quantum efficiency reminds one to consider the applied voltage together with the spectrum of the illumination in the design of a photoreceptor for optimal performance. For example, in xerography, the transit time of photogenerated holes across the thickness of an a-Se based photoreceptor is invariably much shorter than the exposure time. This implies that the photoinduced discharge mechanism is emission limited. As the field in the photoreceptor decays, the photogeneration rate diminishes because quantum efficiency is field dependent. Consequently the total number of photogenerated charge carriers is not simply proportional to the exposure, which makes gray scale images more difficult to replicate.

There is however a challenge to the interpretation of the quantum efficiency in *a*-Se mentioned above. According to a sub-nanosecond transient photoconductivity experiment carried out using a matched microwave stripline technique and a very short laser pulse (25ps at 1.8 to 2.29eV photon energy), the quantum efficiency as inferred from the peak photocurrent in the sub-nanosecond time scale shows no field or temperature dependence. This is in contrast to that inferred from TOF transient photoconductivity and xerographic photoinduced discharge experiments done in the time scale of microseconds and above. It is believed that the apparent field dependence of the quantum efficiency is a carrier supply yield rather than intrinsic to the material. More careful experiments are now needed to clarify the present controversy [57].

2.9 Thermal Properties and Aging (Structural Relaxation)

Being an inorganic polymeric glass, *a*-Se exhibits many of the properties of glassy polymers. Its glass transformation and crystallization behaviors have been extensively studied using the differential scanning calorimeter (DSC) type of differential thermal analysis (DTA) measurements, which involves monitoring the rate of heat flow into the specimen as a function of the sample temperature while the sample is heated at a constant rate. Figure 2.15 shows a typical DSC thermogram on a pure *a*-Se film at a heating rate of 10°C per min. The glass transformation, crystallization, and melting phenomena are clearly visible as endothermic, exothermic, and endothermic peaks, in the diagram respectively [59]. The dependence of the glass transition temperature, T_g on the heating rate r, and the aging time t_A, can be readily explained by the enthalpy vs. temperature behavior of a typical glass-forming material shown in Figure 2.16. A main important note here is that in contrast to the glass transition temperature $T_g(q)$, which depends only on the cooling rate q, the observed glass transition temperature $T_g(r)$, depends both on the heating rate and the initial state, $H_E(T_A)$. This may have implications in device applications.
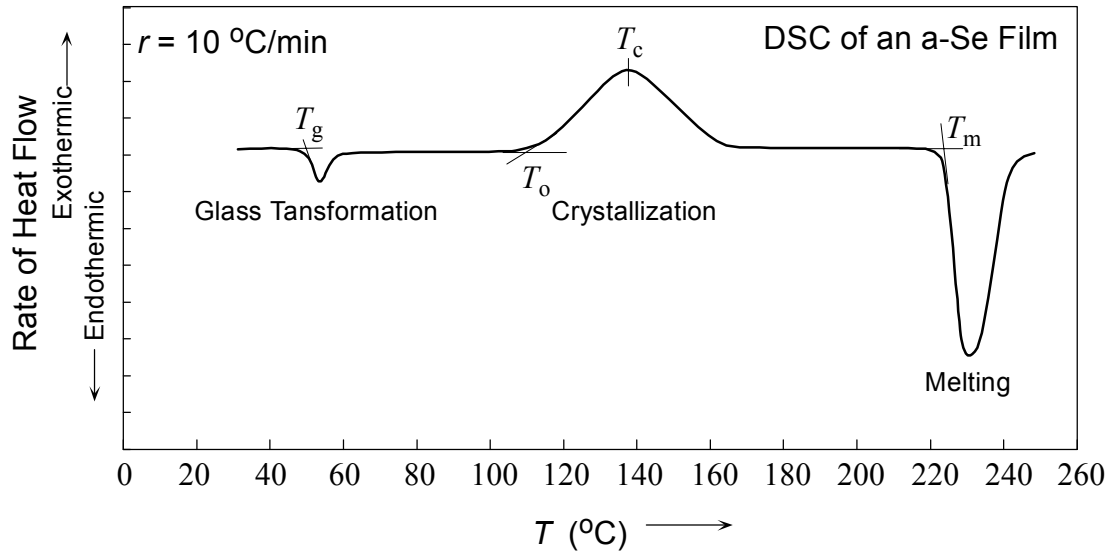
Figure 2.15: A typical DSC thermogram for an *a*-Se film showing the glass transition region, crystallization, and melting transitions. Heating rate $r = 10°C/min$, the glass transformation temperature is T_g, the crystallization onset temperature is T_o, the maximum crystallization rate temperature is T_c, and the melting temperature is T_m [59].

In the case of *a*-Se, a variety of experiments under thermal cycling conditions has indicated that after a prolonged annealing at room temperature, the thermodynamic state of *a*-Se corresponds almost to that of the super-cooled metastable liquid at A in Figure 2.16. The significance of the glass transformation behavior of *a*-Se is that as T_g approached, many physical properties of the film, such as the traveling range, $\mu\tau$ of the hole carriers, exhibit abrupt changes as a result of relaxation phenomena. The mean relaxation time τ, for structural relaxations in *a*-Se has a *Vogel*-type temperature dependence, which behaves like $\tau \propto \exp[A/(T-T_o)]$. This type of relaxation phenomenon is typical of many organic polymers and is consistent with the *Williams-Landel-Ferry* behavior observed for the dielectric relaxation in these materials [59].
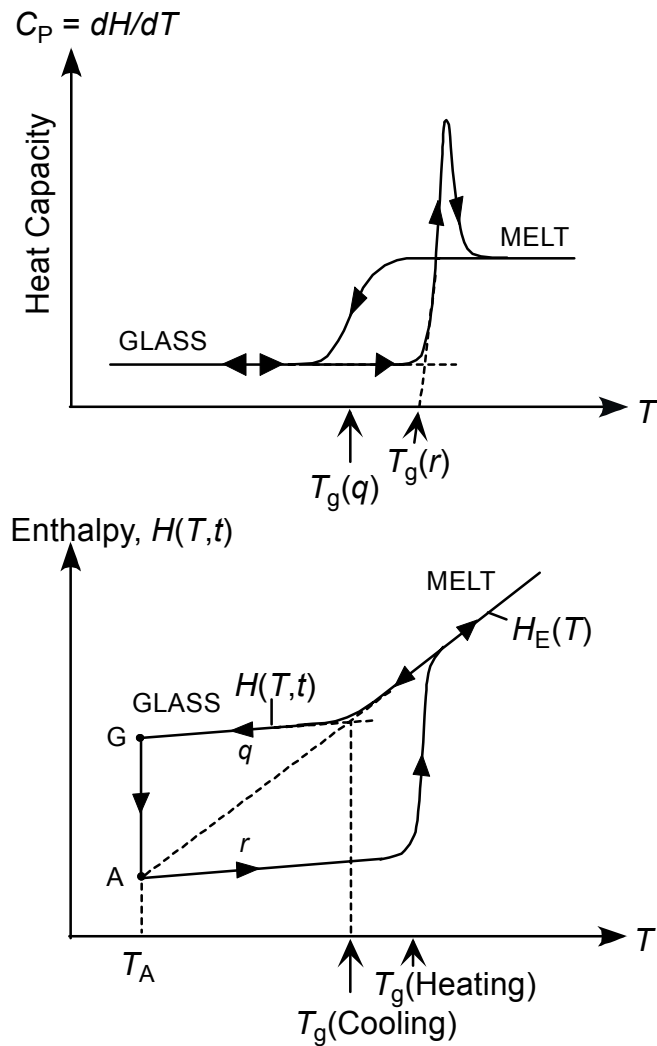
Figure 2.16: Enthalpy H, versus temperature T, for a typical glass-forming liquid. As the melt is cooled at a rate q, eventually the structure goes through a glass transformation at T_g (cooling) or $T_g(q)$. The enthalpy of the glass is higher than the equilibrium liquid-like enthalpy, $H_E(T_A)$ at A. When the glass at point G aged, the structure relaxes towards the equilibrium like metastable state at A. On reheating at a rate r, the glass enthalpy recovers towards $H_E(T)$ where $T=T_g$ (heating) or $T_g(r)$. The upper curve shows the heat capacity versus temperature behavior observed during heating and cooling [59].

Nearly all physical properties of *a*-Se evince an aging behavior, which is just a form of structural relaxation whereby the property changes with time as the film is left to anneal isothermally. For example, it is noted that the *Vickers* micro-hardness of an *a*-Se film will increase from about $25Kg \cdot f \cdot mm^{-2}$ to $35Kg \cdot f \cdot mm^{-2}$ and eventually stabilizes at around this value after aging for several hundred hours after deposition. At room temperature, the whole relaxation normally occurs over a time scale of ~1000 hours (~42 days). The aging behavior has been reported for various properties of *a*-Se, e.g., density, heat capacity, density of structural defects, etc. and is a fundamental property of all glasses. The basic principle of the aging process can be explained by enthalpy-temperature or volume-temperature diagrams as illustrated in Figure 2.16 [59].

The dependence of the electronic properties of *a*-Se on aging can be significant. For example in a recent study, Koughia et al. [53] have shown that the deep electron trap in *a*-Se decreases with aging, as shown in Figure 2.17. The dependence of the optical properties of *a*-Se on aging has not been studied in detail.
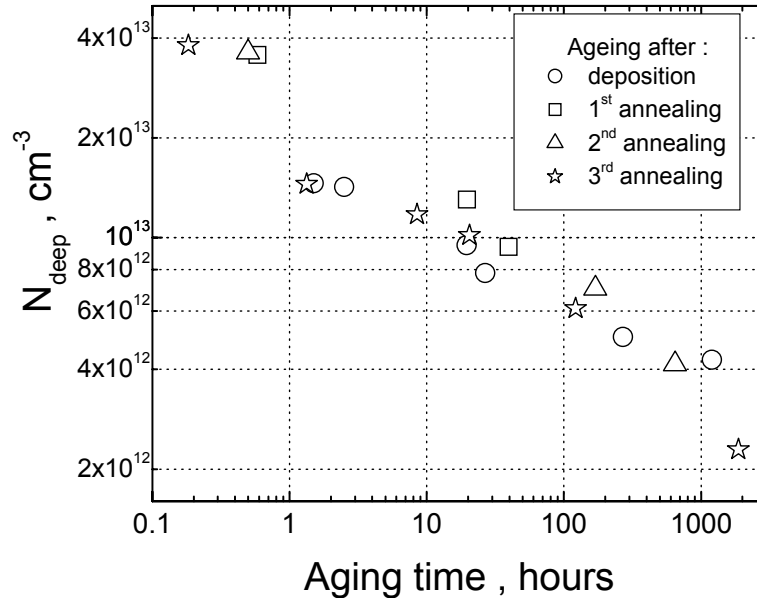
Figure 2.17: Influence of aging-annealing on the deep state concentration in stabilized *a*-Se. The sample was deposited on an unheated substrate. The source material contained 0.5 at. % As and no Cl. Annealing was performed at 40-45°C for 20-40min [53].

Pure *a*-Se is sensitive to crystallization and invariably crystallizes at a rate determined by the nucleation process, the morphology of growth, and the temperature. The isothermal crystallization rate has been found to be well described by the *Avrami* equation. The crystallization growth rate was found to be inversely proportional to the melt viscosity, which is adequately described over a temperature range by *Vogel*-type temperature dependence. Alloying *a*-Se with arsenic has been found to be very effective in retarding the crystallization rate. In fact, once the arsenic content has reached a few percent, the alloy is almost immune to crystallization. Nevertheless, it does have the adverse effect of creating hole traps. This can however be overcome by adding chlorine in parts per millions amounts to compensate for the As-induced traps. Alloying *a*-Se with As also increases the overall glass transformation temperature and makes *a*-Se based films more mechanically stable. Although most *a*-Se based modern photoreceptors are essentially Se-Te alloys or *a*-As_2Se_3, the chlorinated Se:0.5% As alloy is still in use in x-ray imaging applications and often forms the overcoat layer in multilayer Se-Te based photoreceptors. The chlorinated Se: 0.5% As alloy is typically referred as stabilized *a*-Se [59].

2.10 Summary

In order to gain some measure of understanding of the unique electronic and optical properties of an amorphous semiconductor, a theoretical grasp of its energy band structure is required. However, due to the loss of long range order in an amorphous material, the energy band structure can only be mapped from observations obtained from various rigorous experiments. One important difference between a crystalline and amorphous semiconductor is the existence of localized states in the mobility gap ("energy gap"). Amorphous semiconductors have a high degree of short range spatial order in their atomic structure. Their DOS structure is closely related to that of their crystalline counterparts. While some of these localized states are created by defects, the majority of them are created by the loss of long range order and are unique to solids that are amorphous.

The two most important optical constants are the refractive index, n and absorption coefficient, α. The absorption edge of many amorphous semiconductors has the shape shown in Figure 2.3. Many semiconducting glasses have been observed to have an absorption that follows $\alpha\hbar\omega(\omega) \propto (\hbar\omega - E_g^{opt})^r$ in the fundamental absorption edge, where $r = 1$ for a-Se and E_g^{opt} is defined as the Tauc optical gap. In the Urbach region, the absorption follows $\alpha \propto \exp(h\upsilon/\Delta E)$, where ΔE is Urbach width. In the Urbach tail region, the strength and shape of the absorption coefficient were found to depend on the preparation, purity and thermal history of the material, regardless of its thickness.

The refractive index in a lossy material is complex and can be described by the refractive index n and the extinction coefficient, K. The optical constants n and K can be determined by measuring the reflectance from the surface of a material as a function of polarization and the angle of incidence. There are several popular models describing the spectral dependence of the refractive index, n in a material and the most versatile model is the *Sellmeier* equation. The refractive index of a semiconductor usually decreases with increasing energy bandgap E_g and increases with increasing temperature. The *Kramers-*

Kronig dispersion relationship is a very useful equation that allows one to derive the refractive index from the absorption coefficient and vice versa. It was deduced under very general conditions and is valid for amorphous materials and liquids as well as for crystals. It only requires that the material have a relative permittivity that is independent of the applied field. The refraction index at zero frequency, n_o is used as an indicator of changes in the structure and the polarizability of a material.

Recent structural studies on *a*-Se and its alloys favor a "random chain model" as shown in Figure 2.9, in which all the atoms are in twofold coordinated chain structures and the dihedral angle ϕ is constant in magnitude but changes sign randomly. A characteristic of *a*-Se is the presence of some thermodynamically derived charged structural defects, called the valence alternation pairs and intimate valence alternation pair. There is experimental evidence that some localized states, both shallow and deep in the mobility gap, are the result of various structural defects and are thermodynamically stable at room temperature. While the thermally activated hole drift mobility is dependant on the applied electric field, the electron drift mobility is relatively field-independent. The concentration of deep traps is known to depend on alloying, doping, and aging, while the exact nature of the shallow traps has not been conclusively determined. In a semiconductor such as *a*-Se, the localized states play an important role in conduction and can be investigated by a time-of-flight experiment. The average drift mobility in a crystalline semiconductor is a million times higher than those in *a*-Se.

The behavior of the optical absorption coefficient of *a*-Se at around the fundamental absorption edge can be attributed to a sharp rise in the density of states at the band edges. The mechanism for the field-dependent quantum efficiency observed for *a*-Se is common to other molecular solids and can be explained by the dissociation of an initially bound electron-hole pair. Being an inorganic polymeric glass, *a*-Se exhibits many of the properties of glassy polymers. The significance of the glass transformation behavior of *a*-Se is that as T_g is approached, many physical properties of the film, such as the carrier range $\mu\tau$ of the holes carriers, exhibits sharp changes as a result of relaxation phenomena. Nearly all physical properties of *a*-Se evince an aging behavior,

which is just a form of structural relaxation whereby the property changes with time as the film is left to anneal isothermally. It is noted that the *Vickers* micro-hardness of an *a*-Se film increases about 50% after it has been aged for about 42 days. This aging behavior has been reported for various properties of *a*-Se, e.g., density, heat capacity, density of structural defects, etc. and it is a fundamental property of all glasses. Besides aging, pure *a*-Se is also sensitive to crystallization. It invariably crystallizes at a rate determined by the nucleation process, the morphology of growth, and the temperature. The crystallization growth rate is inversely proportional to the melt viscosity and is well described by the *Avrami* equation. Alloying *a*-Se with As has been found to be very effective in retarding the crystallization rate. Nevertheless, it does have the adverse effect of creating hole traps. This can however be overcome by adding chlorine in parts per millions amounts to compensate for the As-induced traps. Alloying As with *a*-Se also increases the overall glass transformation temperature and makes *a*-Se based films more mechanically stable.

3. Sample Preparation and Experimental Procedure

3.1 Introduction

The descriptions of the various ways to prepare different types of a-Se samples for measurement and the method used to obtain the experimental data for the calculation of optical properties are given in this chapter.

In general, amorphous solids (bulk samples), can be made from melt or solutions while amorphous layers (thin films), can be fabricated from the gaseous phase through the condensation of vapors on suitable substrates either through evaporation, cathode sputtering, glow discharge or chemical vapor deposition. In this project, the bulk samples were made from melt and the thin films were made from thermal evaporation under vacuum and cathode sputtering.

This chapter will start off with the fabrication techniques for a bulk sample before the two different processes, thermal evaporation and cathode sputtering, used in the making of thin films will be introduced. It will then finish with the acquisition method used for obtaining the transmission spectrum of both the bulk and the thin film sample.

3.2 Fabrication of Bulk Amorphous Selenium

Bulk amorphous selenium was fabricated in the following manner. First of all, a typical load of 5-10g of selenium pellets of 99.9999% purity was poured into a quartz ampoule. Excess air was then pumped out of the ampoule with a diffusion pump in an ampoule sealing station. The sample in the quartz ampoule was sealed in a vacuum of about 10^{-4} to 10^{-5} torr by carefully melting the opening of the ampoule together with a torch. The vacuum-sealed ampoule was then inserted into a rocking furnace like the one shown in Figure 3.1, heated to a desired temperature and maintained at this temperature for at least 12hrs so that the amorphous solid will be homogeneous and isotropic.
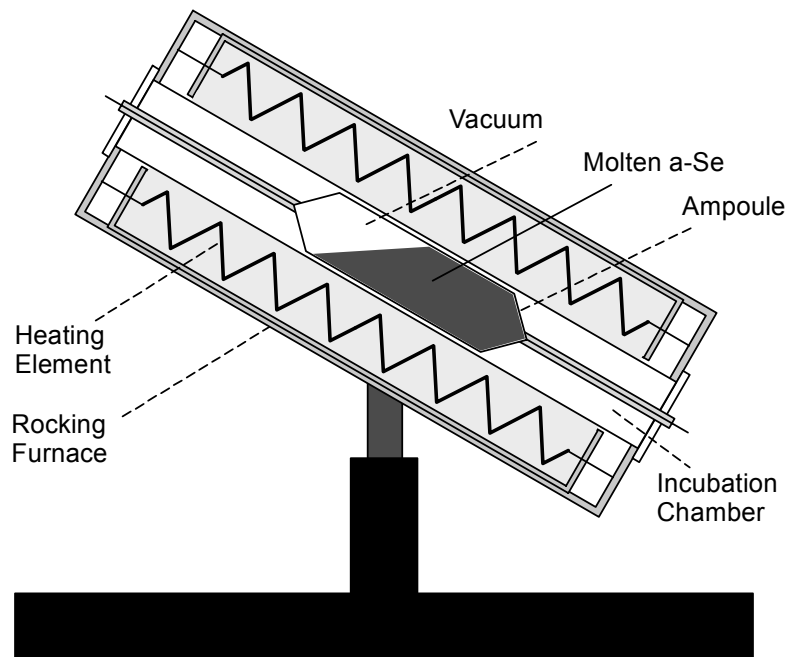
Figure 3.1: Schematic diagram of a rocking furnace.

The melt was then allowed to cool off, either in air or water, at a controlled rate suitable for glass formation. When the melt had solidified into a-Se solid, the ampoule was wrapped in a protective cloth and carefully cracked opened with a hammer. It was done in such a way that the a-Se was broken along its natural stress line into smaller pieces suitable for grinding and polishing.

A broken piece of amorphous selenium solid was then ground down to the desired thickness. This was done with sandpaper and silicon carbide powder, starting from a sandpaper of grit size 320 to silicon carbide powder of grit size 600 and 1000, in descending order of coarseness. In order to ensure that the finished product is flat on both surfaces, the sample has to be sandwiched by two equally flat surfaces. This can be accomplished by sanding the sample on a flat glass slab with the other side bee-waxed to a flat polishing-disk. Both surfaces were then ground down in this way until the desired thickness was reached.

When the sample is visually parallel to the glass slab, it was sent to the polishing machine, which is the *MiniMet* 1000 made by BUEHLER, for polishing. In this station, the sample would go through 3 rounds of polishing in incremental speed set at 10rpm, 15rpm and 30rpm for 10mins, 15mins, and 30mins respectively. A different grade of polishing cloth, starting from a Micro polishing cloth to a Pellon polishing cloth with alumina powder of average particle diameter of 3μm and 0.05 μm was used at each round, in descending order of coarseness. The polishing cycle was repeated until the sample is reasonably smooth and shiny. This is important as a sample with a smooth surface will only suffer a very little amount of light scattering from its surfaces and thus will have minimum amount of error in absorption measurement. The sample is deemed smooth when its transmittance is close to the transmittance value of a thick slab, i.e. no interference fringes in its transmission spectrum, a-Se film at the transparent region, $T >$ 60%.

The table below shows the fabrication conditions for bulk *a*-Se samples. The desired transmittance for a smooth surface is $T_{film} = 70\%$, which is the typical transmittance of a thick *a*-Se film at λ=2000nm. All the samples were quenched in water and the thickness of the sample was measured with a digital precision micrometer called *Digimatic Micrometer* APB-2D, made by Mitutoyo Corp.

Table 3-1: Specifications for glass synthesis. T_m is the furnace temperature, T_q is the quenching temperature, T is the measured transmittance at $\lambda = 2000$nm, P is the ampoule's pressure and d is the measured thickness.

date	Run #	d (mm)	Sample	$P(x10^{-5})$ (torr)	T_m (°C)	Heating Duration (hrs)	T_q (°C)	T (%)
9/26/05	Se500wA	0.900	Bulk *a*-Se	4.0	500	14	20	50
9/26/05	Se500wB	1.053	Bulk *a*-Se	4.0	500	14	20	20
10/2/05	bSe8C	0.339	Bulk *a*-Se	4.0	800	18	20	61
10/16/05	BSeAs	0.265	Bulk *a*-Se 0.5wt% As	4.0	500	17	20	68

3.3 Fabrication of amorphous selenium thin films by thermal evaporation in vacuum

The making of an amorphous selenium thin film by thermal evaporation in vacuum is done in the following way. Firstly, a typical load of 15-25g of selenium pellets of 99.9999% purity was placed in a boat in the system as shown in Figure 3.2. The bell jar was then closed and the system pumped down to around $P \approx 10^{-6}$ torr through a diffusion pump. At this level of air pressure, the entire environment inside the deposition chamber is free of impurities and the sample is ready for deposition.

With the shutter in the closed position, the temperature of the substrate was set to the desired level and the boat was heated till the selenium pellets started to evaporate. Once the evaporation rate stabilized and the substrate was at its desired temperature, the vapor was allowed to come into contact with the substrate. A layer of amorphous selenium would form on the substrate and the thickness of the film was controlled by the shutter with the help of a growth monitor. In this system, the growth monitor uses a quartz crystal to measure the deposition rate. When the desired thickness was reached, the shutter was closed and the system was shut down. The amorphous selenium film was maintained at the substrate temperature until the boat and the chamber cooled down to a level suitable for the film to be removed from the system.

The table below displays the fabrication conditions for the thermal deposition of a-Se thin films. In the table, T_m is the boat (sample heater's) temperature, T_q is the quenching (substrate's) temperature, t_{eva} is the duration of the deposition or the time the shutter remained opened, the rate is the deposition rate, P is the chamber pressure and d is the desired thickness calculated from the growth monitor.

Table 3-2: Fabrication conditions for the thermal deposition of a-Se films. T_m is the boat temperature, T_q is the substrate temperature, t_{eva} is deposition time, the rate is the deposition rate, P is the chamber pressure and d is the thickness of the film.

date	Run	Sample Composition	$P(\times 10^{-6})$ (torr)	T_m (°C)	t_{eva} (s)	rate (nm/s)	T_q (°C)	d (μm)
7/23/04	293	a-Se	1.6	225	42	23.33	51.0	0.98
7/25/04	294	a-Se	1.5	225	80	25.00	2.6	2.00
7/26/04	295	a-Se	1.5	235	191	26.18	3.0	5.00
7/28/04	297	a-Se:67ppm-Cl	1.6	221	260	38.46	2.3	10.00
7/29/04	298	a-Se:67ppm-Cl	1.5	221	65	30.77	3.4	2.00
8/4/04	301	a-Se	1.0	221	240	41.67	3.4	10.00
7/26/05	375	a-Se	2.0	236	70	45.71	51.0	3.20
10/2/05	375C	a-Se (annealing)	2.0	0	0	0.00	51.0	3.90
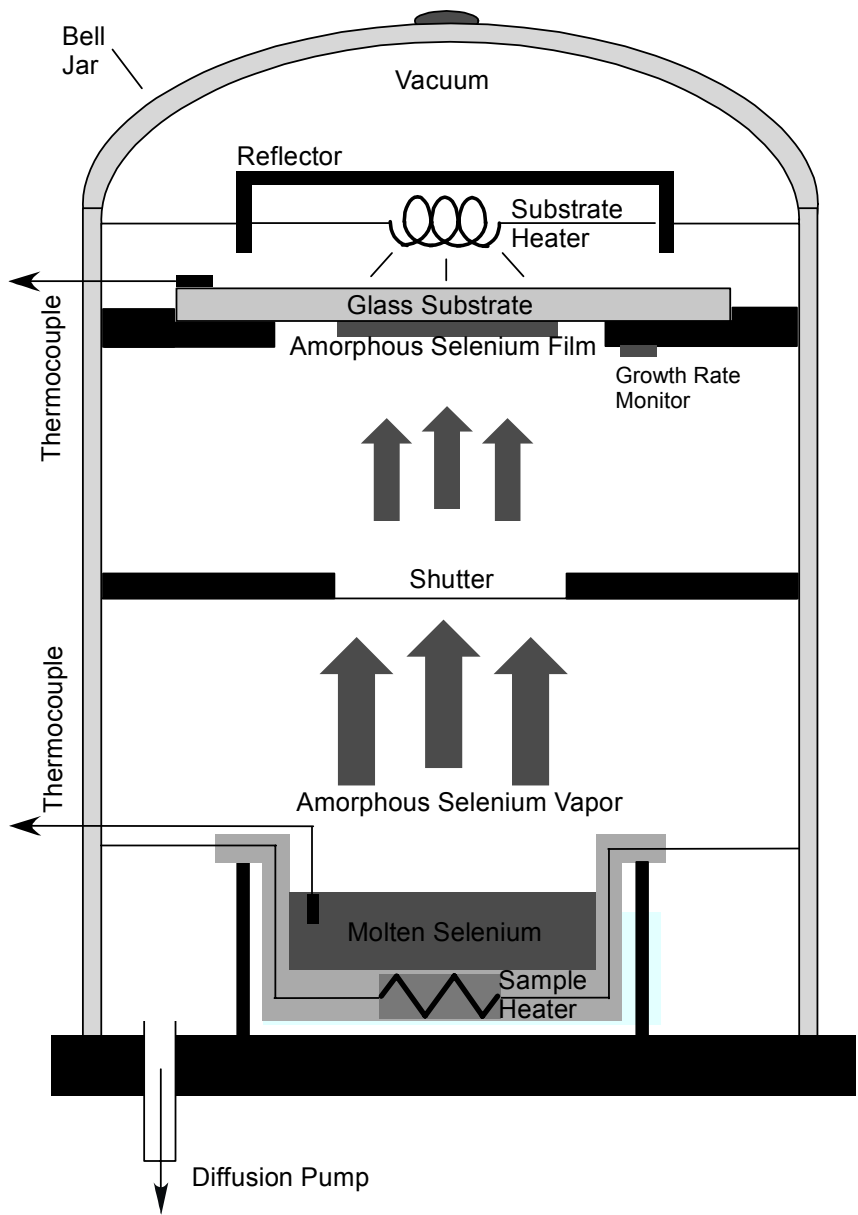
Figure 3.2: Schematic diagram of a thermal deposition system.

3.4 Fabrication of amorphous selenium thin films by cathode sputtering

An amorphous selenium thin film can also be produced by cathode sputtering. This can be done in the following manner using a system as shown in Figure 3.3. Firstly, before any sputtering process can begin, there must be a suitable selenium sputtering target. In this project the target was made by melting selenium pellets in the target holder using either a hot plate in atmospheric pressure under a fume hood, or a heating filament in a thermal evaporation chamber under vacuum like the one shown in Figure 3.2.

The target was then fastened to one of the three sputtering guns and the substrate placed on the turning table in the chamber. The system was pumped down to around 10^{-5} torr using a turbo pump. Once the chamber pressure has reached the desired level, argon gas was let in at a controlled rate. The table was then allowed to turn at the desired rotation speed and the shutter to the selenium target was opened.

At this time, the RF power to the sputtering gun that holds the target was turned on and then fine tuned to deliver maximum power to the load. The sputtering process began as soon as there was no reflected power detected by the system. Layers of amorphous selenium would form on the substrate when the target was bombarded by the Argon plasma. The thickness of the sample can be controlled by the flow rate of the argon gas and the rotational speed of the turn table. It can also be monitored by the thickness monitor that uses a quartz crystal. The RF power was turned off when the desired thickness of the film was reached.

Due to the difficulty of making a good selenium sputtering target, no trial runs have passed the consistency test so far. In almost every 3 to 4 runs, the target would melt during sputtering and a new target would have to be made. A different method of making a more reliable sputtering target has to be devised before any runs can be successful.
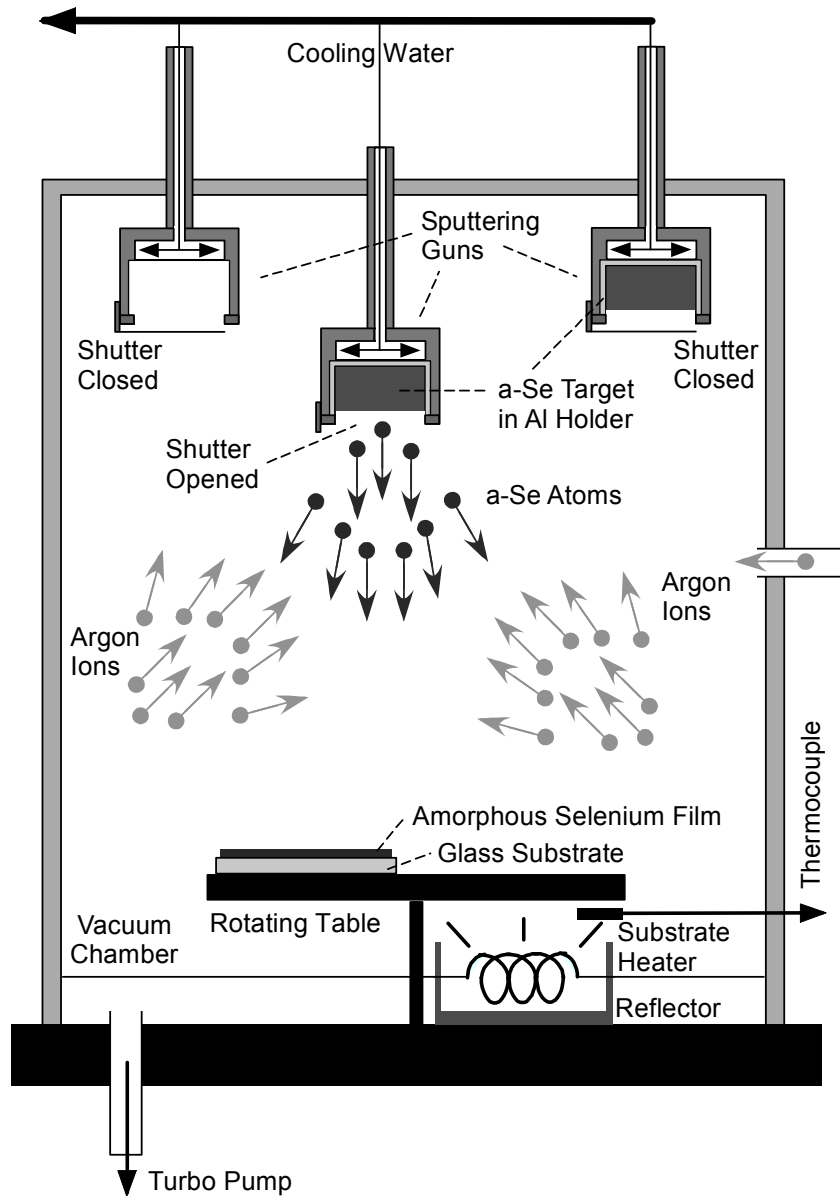
Figure 3.3: Schematic diagram of a magnetron sputtering system.

3.5 Substrate Preparation

Corning 7059 glass was the substrate used for depositing thin films of *a*-Se. Preparation of the substrate involves a cleaning procedure, which removes any unwanted particles and impurities that may be on the glass surface. The beaker and rack, which holds the substrates, were cleaned and rinsed in an ultrasonic cleaner using *extran* MN-1 powder detergent dissolved in deionized water. The Corning 7059 glass slides are then placed in the rack inside the beaker, washed and rinsed for 4 cycles in the ultrasonic cleaning bath using the *extran* MN-1 powder detergent in deionized water. After removing the substrates from the bath, the glass slides were blown dry with high purity filtered air. Complete drying is achieved by baking the substrates in an oven at 30°C for at least 12hrs.

3.6 Transmission Spectrum Measurement

The transmission spectrum of the samples fabricated using the above methods can be obtained from a spectrometer as shown in Figure 3.4.
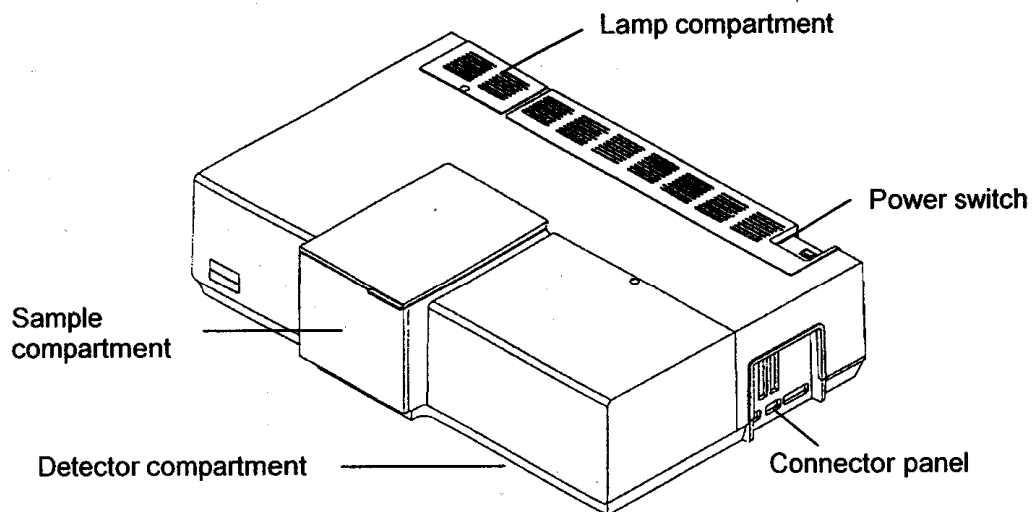
Figure 3.4: Features of the Lambda 900 spectrometer (from Lambda 800/900's manual).

The Lambda 800/900 spectrometer features an all-reflecting, double-monochromator optical system. The components are coated with silica for durability. Holographic gratings are used in the monochromator for the ultra-violet and visible light range and near infrared range. Table 3-3 shows the essential specifications of the system.

Figure 3.5 is a schematic diagram illustrating the operation of a spectrometer. Basically, the instrument has two radiation sources that cover the full operating wavelength of the spectrometer from 185nm to 3300nm, a monochromator that is responsible for passing monochromatic light to the sample, and two photodetectors for measuring the transmittance at different wavelength regions. The deuterium lamp and halogen lamp are the two radiation sources. The later is in charge of the wavelength in the visible to near infrared region, i.e. from 300nm to 3300nm, while the other is in charge of those wavelengths from 185nm to 350nm.

Table 3-3: Operating specifications of the Spectrometer (from Lambda 800/900's manual).

Optics

Beam center height	90 mm above baseplate
Beam cross-section	<u>Slit</u> <u>Width (approx.)</u> <u>Height (approx.)</u> 0.05 nm 0.04 mm x 11.7 mm 0.1 nm 0.09 mm x 11.7 mm 0.5 nm 0.45 mm x 11.7 mm 1 nm 0.89 mm x 11.7 mm 2 nm 1.00 mm x 11.7 mm 5 nm 4.44 mm x 11.7 mm measured at the focal point of the sample beam and the reference beam in the sample compartment at a wavelength of 500 nm.
Beam separation in sample compartment	126 mm
Optical pathlength in sample compartment	200 mm
Grating (Monochromator)	Holographic gratings with 1440 lines/mm UV/Vis 360 lines/mm NIR
Radiation sources	Pre-aligned deuterium and halogen lamps
Detector	A photomultiplier for the UV/Vis range A Peltier-cooled PbS for the NIR range

Abscissa

Wavelength range	185 to 3300 nm UV/Vis/NIR, 900 nm UV/VIS with N_2 purging down to 175 nm
Wavelength accuracy	±0.8 nm UV/Vis ±0.32 nm NIR

Wavelength reproducibility	<0.02 nm UV/Vis range, <0.08 nm NIR range, (0.008 nm UV/Vis range, standard deviation for 10 measurements) (0.04 nm NIR range, standard deviation for 10 measurements)
Spectral bandwidth	0.05 nm to 5.00 nm in 0.01 nm increments UV/Vis range 0.2 nm to 20 nm in 0.04 nm increments NIR range
Integration time	0.04 s to 10 s in 0.04 s increments

Ordinate

Photometric range	Transmission 0% to 200% (display range) Absorbance −6.000 to 6.000 (display range) 1 to 9999 (concentration units)
Photometric accuracy	Absorbance ±0.003; Transmission ± 0.08% at Absorbance = 1 Absorbance ±0.002; Transmission ±0.05% at Absorbance = 0.5 (measured with NIST (NBS) 930 filters)
Stray radiation	Absorbance > 2 (at 200 nm with Potassium Chloride (KCl) solution) Transmission < 0.00008% (at 220 nm, 340 nm and 370 nm; according to ASTM E-387; 1% attenuator in the reference beam) Transmission < 0.002% (measured at 1690 nm with Chloroform ($CHCl_3$); 4 cm pathlength)
Baseline flatness	Absorbance ±0.001 (corrected; 200 nm to 3000 nm, 4 nm slit, Energy 1 NIR, 2 s integration time)

Noise level	Absorbance < 0.00007 at 1500 nm and absorbance = 0
	Absorbance < 0.000050 RMS, at 500 nm; absorbance = 0; 2 s integration time
	Absorbance < 0.000300 RMS, at 500 nm; absorbance = 2; 2 s integration time
	Absorbance < 0.000100 RMS, at 190 nm absorbance = 0; 2 s integration time
Absorbance Zero Stability (drift)	Absorbance < 0.0002 per hour (after warm up at 500 nm, absorbance = 0, 2 nm slit, 2 s integration time)

The monochromator uses reflection gratings and entrance-and-exit slits to pass monochromatic light to the sample. The transmittance of the monochromatic light that passed through the sample is measured by a photomultiplier operating in the ultraviolet and visible region and a lead sulfide detector operating in the near infrared region. One thing to note here is that all transmittance values shown by the instrument are in relative terms. It shows what percentage of light, from 0% to 100%, gets transmitted through the sample with respect to another parallel and unobstructed reference beam.
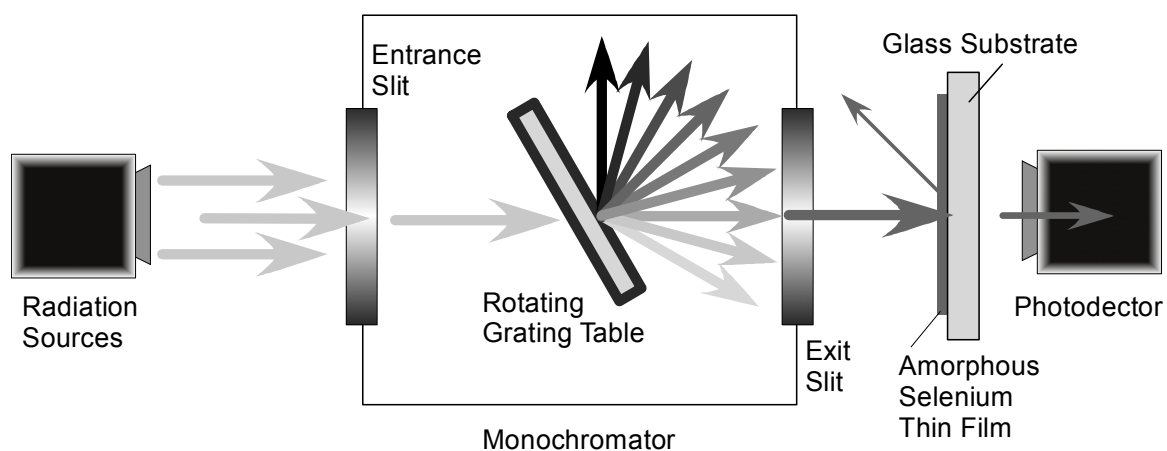
Figure 3.5: Schematic diagram of a spectrophotometer.

4. Analysis of Transmission Spectra: Standard and Improved Swanepoel Techniques

4.1 Introduction

Basically, the amount of light that gets transmitted through a thin film material depends on the amount of reflection and absorption that takes place along the light path. Depending on the material, the transmission spectrum will have two distinctive features, it will either have interference fringes or it will not.
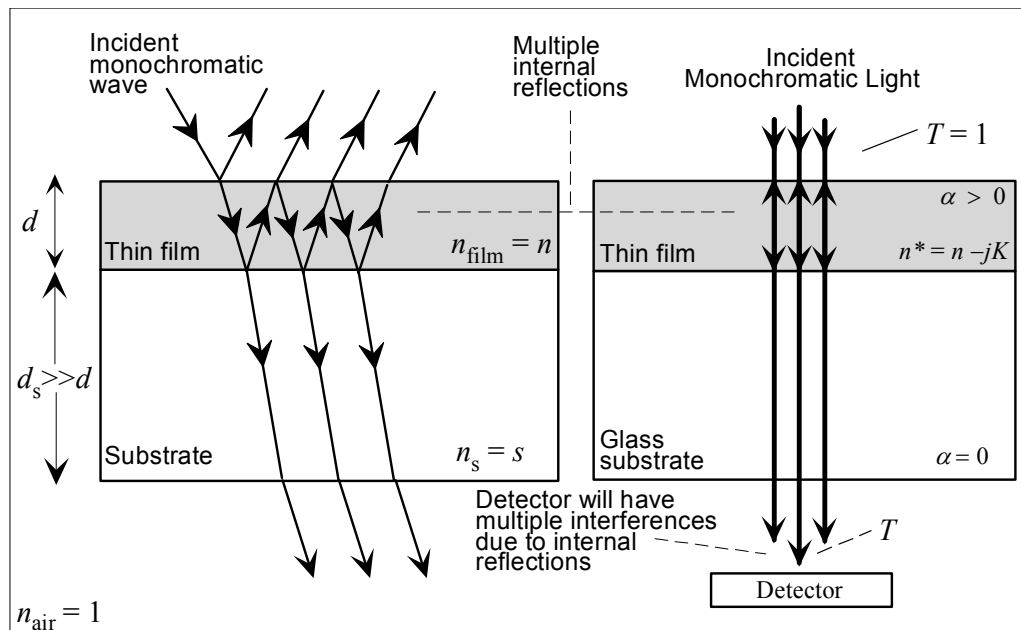
Figure 4.1: Schematic sketch of the typical behavior of light passing through a thin film on a substrate. On the left, oblique incidence is shown to demonstrate the multiple internal reflections. In most measurements, the incident beam is nearly normal to the film as shown on the right.

If the material is a thin film with moderate absorption, there will then be multiple interferences at the transmitted side of the sample, as illustrated in Figure 4.1. This will show up later as interference fringes on the transmission spectrum obtained from a spectrometer. In many instances, the optical constants are conveniently measured by examining the transmission through a thin film deposited on a transparent glass or other (e.g. sapphire) substrate. Figure 4.2 shows a spectrum taken from a thin film on glass substrate. The classic reference on the optical properties of thin films has been the book by Heavens [60]; the book is still useful in clearly describing what experiments can be carried out, and has a number of useful derivations such as the reflectance and transmittance through thin films in the presence of multiple reflections. Since then numerous research articles and reviews have been published including Poelmen and Smet [61], and Swanepoel [62]. They have all critically reviewed how a single transmission spectrum measurement can be used to extract the optical constants of a thin film.
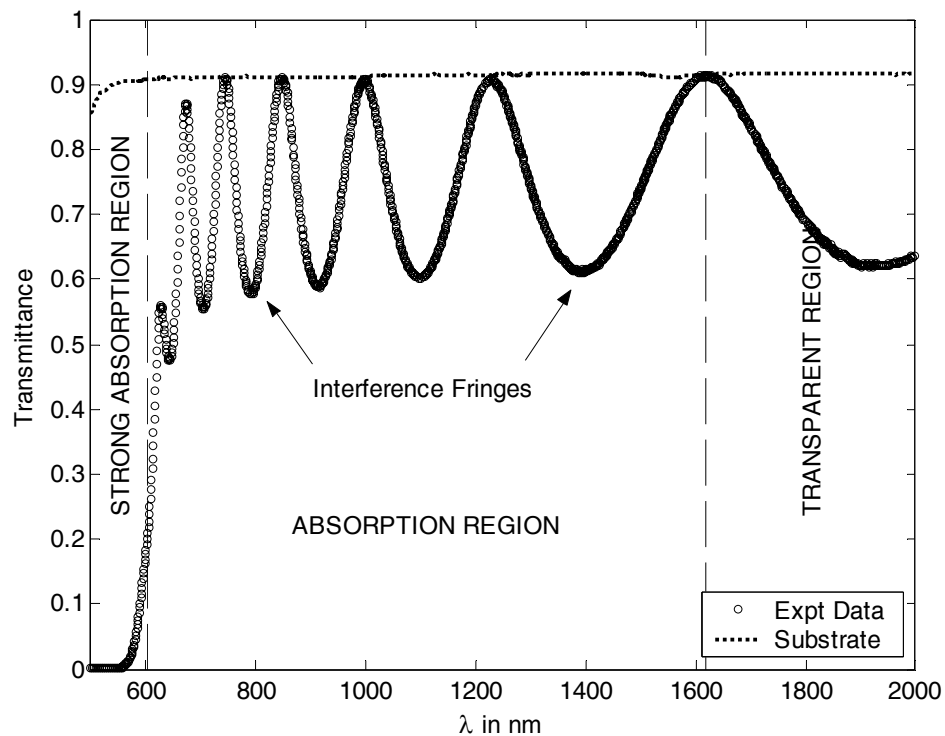
Figure 4.2: An example of a typical transmission spectrum of a 0.969μm thick *a*-Se thin film that has been vacuum coated onto a glass substrate held at a substrate temperature of 50°C during the deposition.

However, if the material is not a thin film on a substrate, there will then be no interferences at the transmitted side of the material and the spectrum will not display any interference fringes. This is as shown in Figure 4.3. In this case, its optical properties can be derived by taking into account of multiple reflections at both surfaces of the sample. This will be elaborated in the next section.
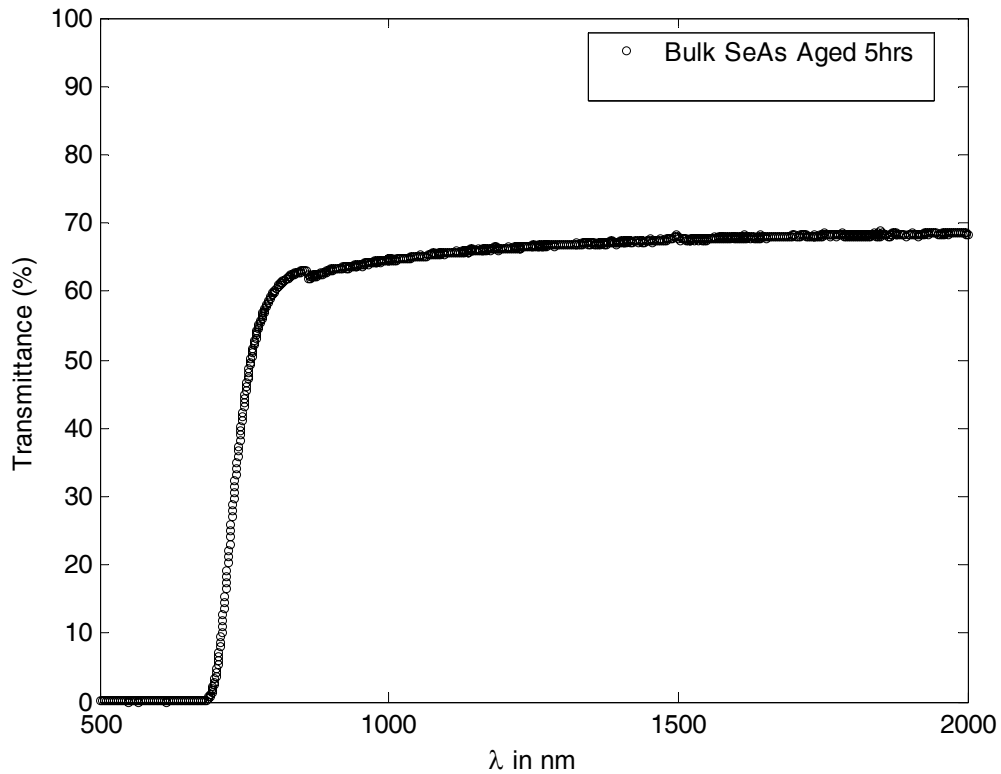
Figure 4.3: An example of a typical transmission spectrum of a 265μm thick a-Se sample doped with 0.5 wt% of As melted at T_m=500°C and water quenched at T_q=20°C .

4.2 Transmission Spectrum with No Interference Fringes

When light gets transmitted through a material at normal incident with multiple reflections at both surfaces of the material, as illustrated in Figure 4.4, the absorptivity, the reflectance and the transmittance can be expressed by the following relationships [63]:

$$T = \frac{(1-r)^2 e^{-\alpha d}}{1 - r^2 e^{-2\alpha d}},$$
(4.1)

$$R = r + \frac{(1-r)^2 r e^{-2\alpha d}}{1 + r^2 e^{-2\alpha d}},$$
(4.2)

$$A = (1-r)\frac{1 - e^{-\alpha d}}{1 - r e^{-\alpha d}}$$
(4.3)

with: $$r = \frac{(n-1)^2 + k^2}{(n+1)^2 + k^2}$$
(4.4)

and $$\alpha = \frac{4\pi k}{\lambda},$$
(4.5)

where r is the reflectivity in a single reflection, α is the absorption coefficient, k is the extinction coefficient or also called the absorption constant, d is the thickness and n is the refractive index. By definition the absorptivity $A = I_A / I_o$, the reflectance $R = I_R / I_o$ and the transmittance $T = I_T / I_o$, where I_A, I_R and I_T are the intensities of the respective absorption, reflection and transmission activities, and I_o is the original intensity of the light.
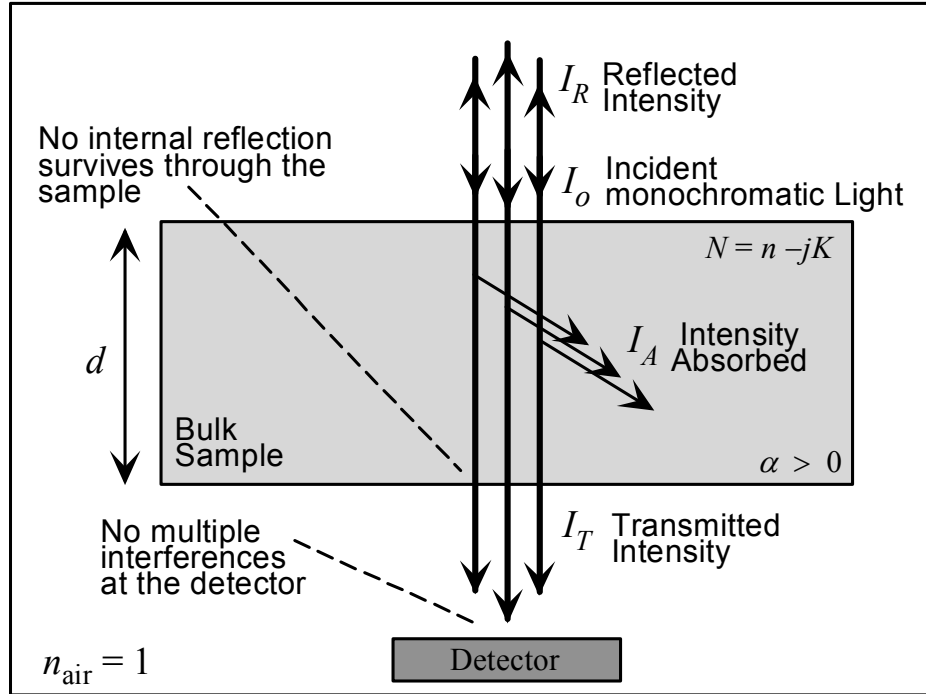
Figure 4.4: Light transmitted through a bulk sample.

4.2.1 Absorption Coefficient of a Thick sample with No Interference Fringes

Using the above equations for a system as shown in Figure 4.4, the absorption coefficient can be obtained as follows:

If $y = e^{-\alpha d}$, then from equation (4.1),

$$(Tr^2)y^2 + (1-r)^2 y - T = 0.$$ (4.1a)

Solving this quadratic equation for y,

$$\alpha = \frac{-1}{d} \ln \left[\frac{-(1-r)^2 + \sqrt{(1-r)^4 + 4(Tr)^2}}{2Tr^2} \right].$$ (4.5a)

So if $\alpha d \gg 1$, the Reflectance R will be equal to the reflectivity in a single reflection r and the absorption coefficient can thus be calculated using equation (4.5b), where

$$\alpha = \frac{-1}{d} \ln \left[\frac{-(1-R)^2 + \sqrt{(1-R)^4 + 4(TR)^2}}{2TR^2} \right].$$ (4.5b)

However if $\alpha\lambda \leq 1$, from equation (4.5) the extinction coefficient will be $k \leq 0.1$, then

$$r \approx \left(\frac{n-1}{n+1}\right)^2.$$

4.4a

In this case, the absorption coefficient can also be calculated from equation (4.5a) using the measured transmittance value T and thickness d of the sample, and a predetermined knowledge of refractive index n. The refractive index can either be sourced from any published data on the material obtained by a different experimental method or in this project, from the refractive index of thin film described in section 4.3.

There will be an upper limit beyond which the values are invalid when the absorption coefficient is determined from a transmission measurement. This limit depends on the sensitivity of the spectrometer and can be estimated by replacing equation (4.1) with an approximation, $T = (1-r)^2\exp(-\alpha d)$, since $\exp(-2\alpha d)$ decays faster than $\exp(-\alpha d)$. With this approximation, a ratio of T/T_o, where T_o is the transmittance value at zero absorption region, can be calculated to give an estimation of the minimum level of transmittance that must be detected by the spectrometer for a given absorption coefficient and thickness. Given $T = (1-r)^2\exp(-\alpha d)$, a ratio of T/T_o gives

$$T = T_o(e^{-\alpha d}).$$

4.1b

For example, in order to study absorption coefficient in the $\alpha = 10^3 cm^{-1}$ region, a sample that is 400μm thick would require the spectrometer to be able to detect transmittance value at around 4×10^{-16}% with respect to the transmittance value at zero absorption region T_o. This is too high a sensitivity requirement for a spectrometer in use today. A typical sensitivity setting in high (Absorbance = 100%) absorption region will be around 0.08% of T_o and 0.05% of T_o in low (Absorbance = 0.2%) absorption region. This will set an upper detectable absorption limit of a sample that is 400μm thick at around $\alpha = 200$ cm^{-1} and a lower detectable absorption limit of a sample that is 400μm thick at around $\alpha = 0.01$ cm^{-1}.

4.2.2 Optical Bandgap of a Thick Sample with No Interference Fringes

Due to the limitation of the transmission sensitivity and the typical thickness of a bulk sample, the upper obtainable limit of the absorption coefficient will probably always be $\alpha_{cal} < 10^4 cm^{-1}$. Thus the optical bandgap can only be found by using the definition recommended by Stuke [64]. According to Stuke, the doubling of the thermal activation energy from conductivity measurements in the absorption spectrum can often be attributed to an absorption coefficient in the order of $10^4 cm^{-1}$. The optical bandgap is taken to be the photon energy at $\alpha = 10^4 cm^{-1}$ from the linear portion of the absorption coefficient curve by plotting the logarithm of the absorption coefficient against the photon energy.
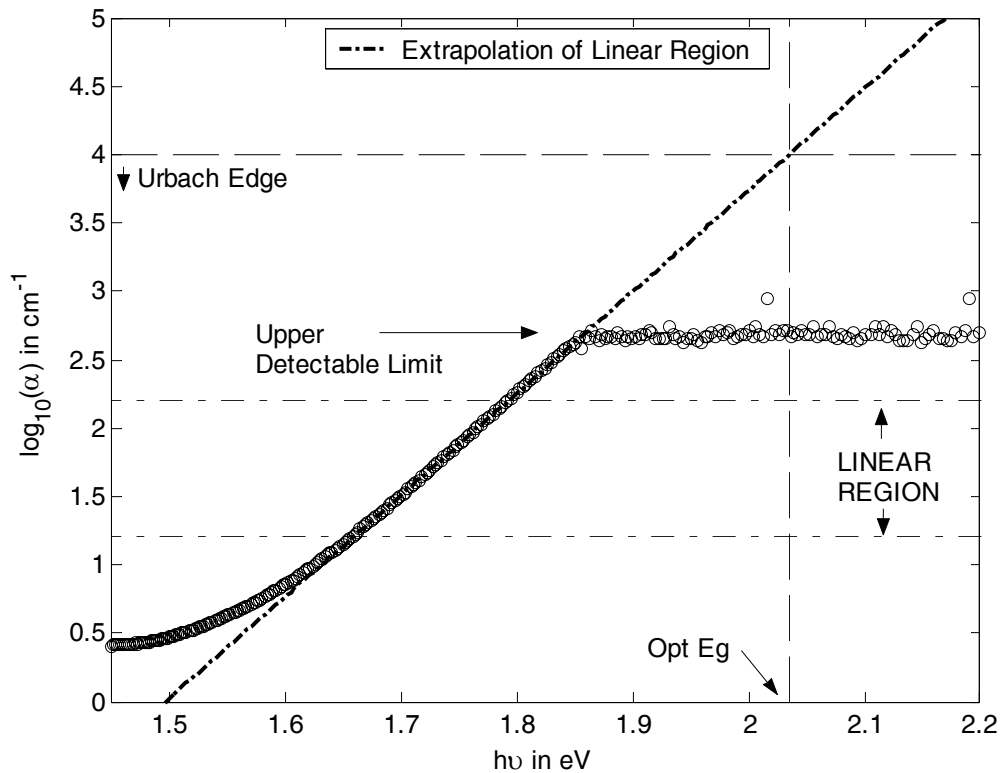
Figure 4.5: Determination of the optical bandgap of a 265μm thick *a*-Se sample doped with 0.5 wt% of As melted at T_m=500°C and water quenched at T_q=20°C.

For any sample that reaches the upper detection limit of its absorption coefficient, extrapolation of the linear portion, anywhere below the upper limit, to the point of $\alpha = 10^4 \text{cm}^{-1}$ has to be constructed before the optical bandgap can be obtained. This is illustrated in Figure 4.5. The extrapolated linear line can also be fitted to a model as shown below in equation (4.5c) for easy reference.

$$\alpha = C \exp(h\upsilon / \Delta E),$$
4.5b

where $h\upsilon$ is the photon energy and ΔE represent the slope of the extrapolated line.

4.3 Transmission Spectrum of a Thin Film
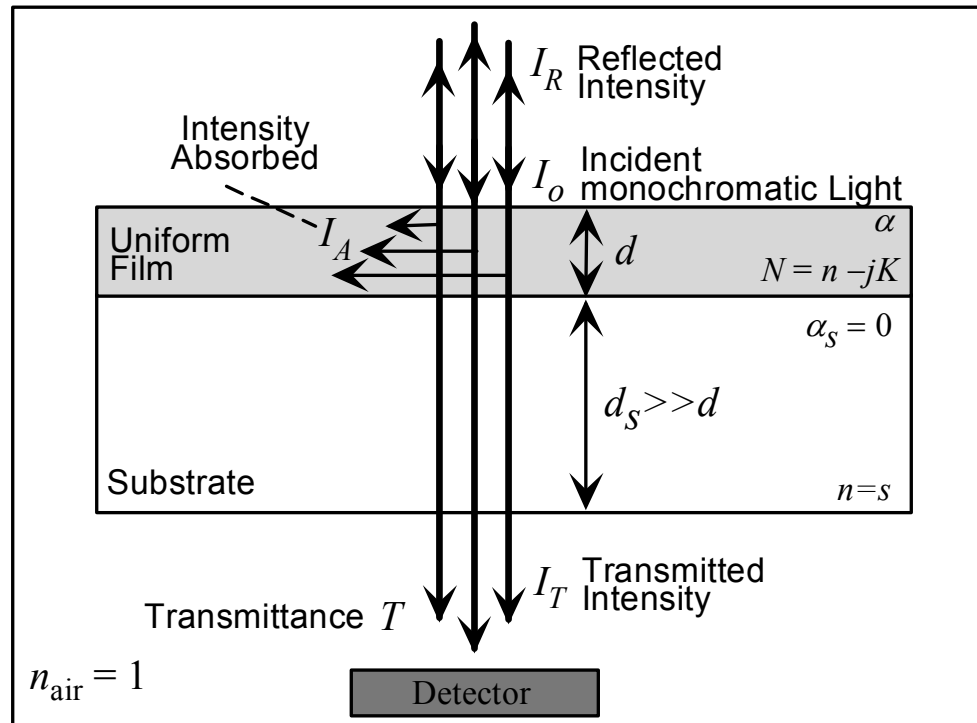
Figure 4.6: Light transmitted through an absorbing thin film on a thick finite transparent substrate.

In this method developed by Swanepoel [62], the author has showed that for a uniform film as shown in Figure 4.6, with thickness d, refractive index n and absorption coefficient α, deposited on a substrate with a refractive index s, the transmittance can be expressed as

$$T = \frac{Ax}{B - Cx\cos\varphi + Dx^2},$$ 　　　　　4.6

where

$$A = 16n^2 s,$$ 　　　　　4.6a

$$B = (n+1)^3(n+s^2),$$ 　　　　　4.6b

$$C = 2(n^2 - 1)(n^2 - s^2),$$ 　　　　　4.6c

$$D = (n-1)^3(n-s^2),$$ 　　　　　4.6d

$$\varphi = 4\pi n d / \lambda,$$ 　　　　　4.7

$$x = \exp(-\alpha d),$$ 　　　　　4.8

and n, s, and α are all function of wavelength, λ.

From equation (4.6), it is not difficult to see that at $\cos(\varphi) = \pm1$, the extremes of the interference fringes will have values around,

Maxima: $$T_M = \frac{Ax}{B - Cx + Dx^2},$$ 　　　　　4.6e

Minima: $$T_m = \frac{Ax}{B + Cx + Dx^2}.$$ 　　　　　4.6f

However, for a film with a wedge-like cross-section as shown in Figure 4.7, equation (4.6) must be integrated over the thickness of the film for it to more accurately describe the transmission spectrum [65]. The transmittance then becomes,

$$T_{\Delta d} = \frac{1}{\varphi_2 - \varphi_1} \int_{\varphi_1}^{\varphi_2} \frac{Ax}{B - Cx\cos\varphi + Dx^2} dx$$ 　　　　　4.9

with

$$\varphi_1 = \frac{4\pi n(\overline{d} - \Delta d)}{\lambda},$$ 　　　　　4.9a

$$\varphi_2 = \frac{4\pi n(\overline{d} + \Delta d)}{\lambda},$$ 　　　　　4.9b

where n, s, and α are all function of wavelength λ, $d = \overline{d} \pm \Delta d$, $\overline{d}$ is the average thickness of the film and Δd is the variation of the thickness throughout the illumination

area. The steps taken to solve both types of film, uniform or non-uniform, in some parts are very similar and they are described in the following sections.
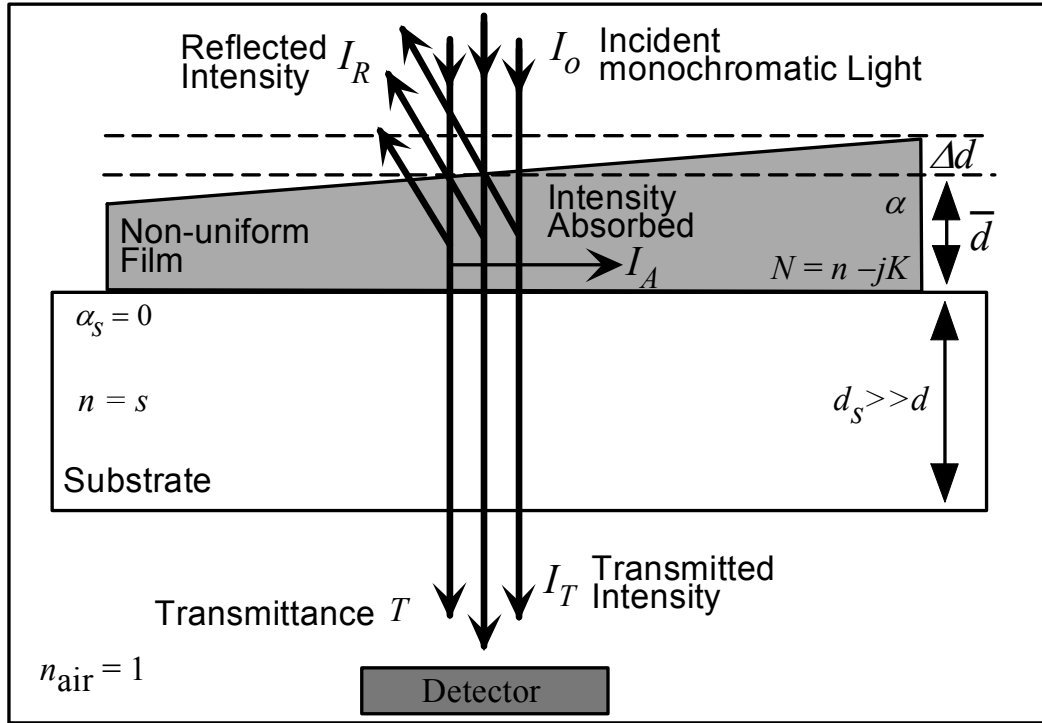
Figure 4.7: Light transmitted through an absorbing thin film with a variation in thickness on a thick finite transparent substrate.

4.3.1 Refractive index of Substrate

Before optical properties of any thin films can be extracted, the refractive index of their substrate must first be calculated using Equations (4.1) and (4.4a) developed earlier in Section 4.2.1. It can be seen that for a glass substrate with very negligible absorption in the range of the operating wavelengths, for example $K \leq 0.1$ and $\alpha \leq 10^{-2} \text{cm}^{-1}$, the transmittance can be simplified to,

$$T = \frac{(1-r)^2}{1-r^2},$$

4.1c

where

$$r = \left[\frac{(n-1)}{(n+1)} \right]^2.$$

4.4a

Rearranging for *n*,

$$n = \frac{1}{T} + \sqrt{\left(\frac{1}{T^2} - 1\right)}.$$

4.10

Thus by rearranging the equation (4.1c) for *n*, the refractive index of the substrate can be obtained from the transmittance measured from the spectrophotometer. With this refractive index, the next step will be to construct two envelopes around the maximas and minimas of the interference fringes in the transmission spectrum.

4.3.2 Envelop Construction
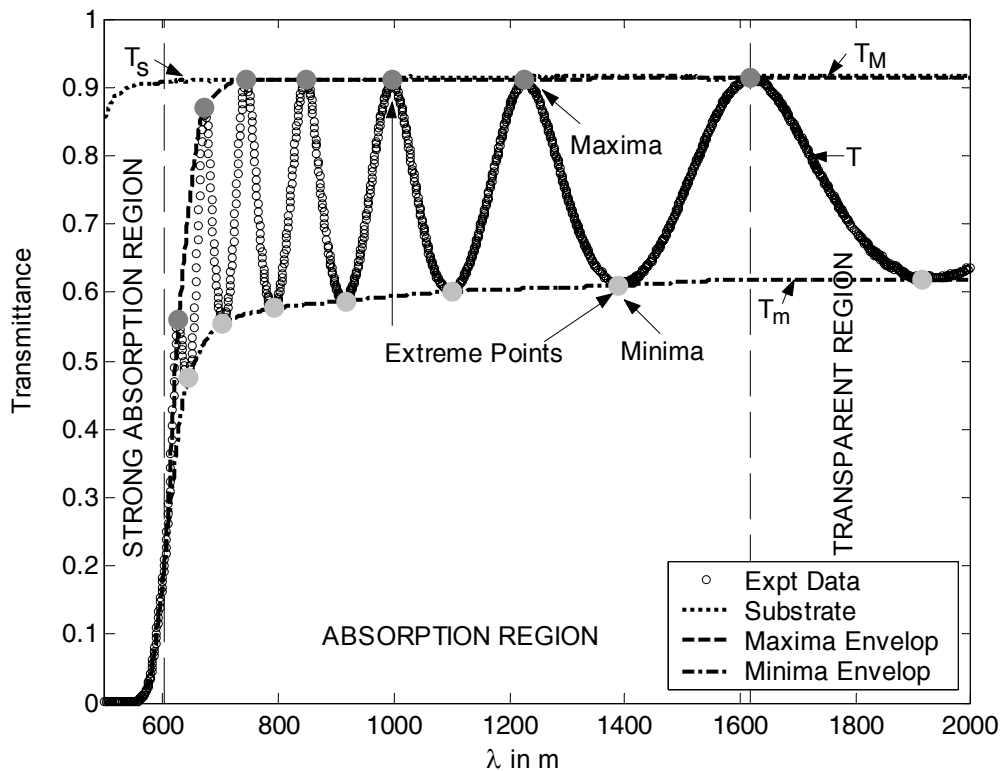
Figure 4.8: The construction of envelopes in the transmission spectrum of a uniform *a-*Se thin film of 0.9687μm.

To construct the two envelopes, the extreme points of the interference fringes in the transmission spectrum must first be located. These points are then used to construct the two envelopes, $T_M(\lambda)$ and $T_m(\lambda)$, that pass tangentially through the maximas and minimas of $T(\lambda)$ as shown in Figure 4.8. From the two figures, it can be seen that, the transmission spectrum is divided into three regions according to their transmittance value namely: the transparent region, where $T(\lambda)$ is greater or equal to 99.99% of the substrate's transmittance value, $T_s(\lambda)$, the strong absorption region, where $T(\lambda)$ is typical smaller than 20%, and lastly the absorption region, which lies between the two regions.

Using the two envelopes at different transmission regions, depending on the shape of the envelopes, the desired optical properties of the thin film can be extracted using either Equation (4.6) or (4.9). These steps will be described in the next few sections.

4.3.3 Thin Film with Uniform Thickness

4.3.3.1 Refractive Index

The refractive index of the thin film with uniform thickness can be calculated from the two envelopes, $T_M(\lambda)$ and $T_m(\lambda)$, by considering the extremes of the interference fringes:

$$\text{Maxima:} \qquad T_M = \frac{Ax}{B - Cx + Dx^2}, \qquad\qquad 4.6e$$

$$\text{Minima:} \qquad T_m = \frac{Ax}{B + Cx + Dx^2}. \qquad\qquad 4.6f$$

Subtracting the reciprocal of equation (4.6e) from equation (4.6f) yields an expression that is independent of the absorbance, x,

$$\frac{1}{T_m} - \frac{1}{T_M} = \frac{2C}{A}, \qquad\qquad 4.11$$

where

$$A = 16n^2 s, \qquad\qquad 4.6a$$

$$C = 2(n^2 - 1)(n^2 - s^2). \qquad\qquad 4.6c$$

Rearranging it for n,

$$n = \sqrt{(N + \sqrt{(N^2 - s^2)})} \, , \qquad\qquad\qquad\qquad\qquad 4.11a$$

where

$$N = 2s \left[\frac{T_M - T_m}{T_M T_m} \right] + \frac{s^2 + 1}{2} \, , \qquad\qquad\qquad\qquad 4.11b$$

T_M and T_m, are the two envelopes constructed from the measured transmission spectrum and s, is the refractive index of the substrate.

Since equation (4.11) will not be valid in the strong absorption region, where there are no maxima and minima, the calculated refractive index has to be fitted to a well established dispersion model, such as the Sellmeier equation, for extrapolation to shorter wavelengths before it can be used to obtain other optical constants. This is illustrated in Figure 4.9, where the calculated refractive indices of a 0.9687μm a-Se thin film was fitted to a Sellmeier dispersion model with two terms. The following are just some common dispersion models for the refractive index,

Sellmeier: $\qquad n = \sqrt{A_s + \dfrac{B_s \lambda^2}{\lambda^2 - C_s^2}} \, , \qquad\qquad\qquad 4.12$

Cauchy: $\qquad n = A_c + \dfrac{B_c}{\lambda} + \dfrac{C_c}{\lambda^2} \, , \qquad\qquad\qquad 4.13$

where A_s, B_s, and C_s are fitting parameters of Sellmeier equation, and A_c, B_c, and C_c are fitting parameters of Cauchy equation.
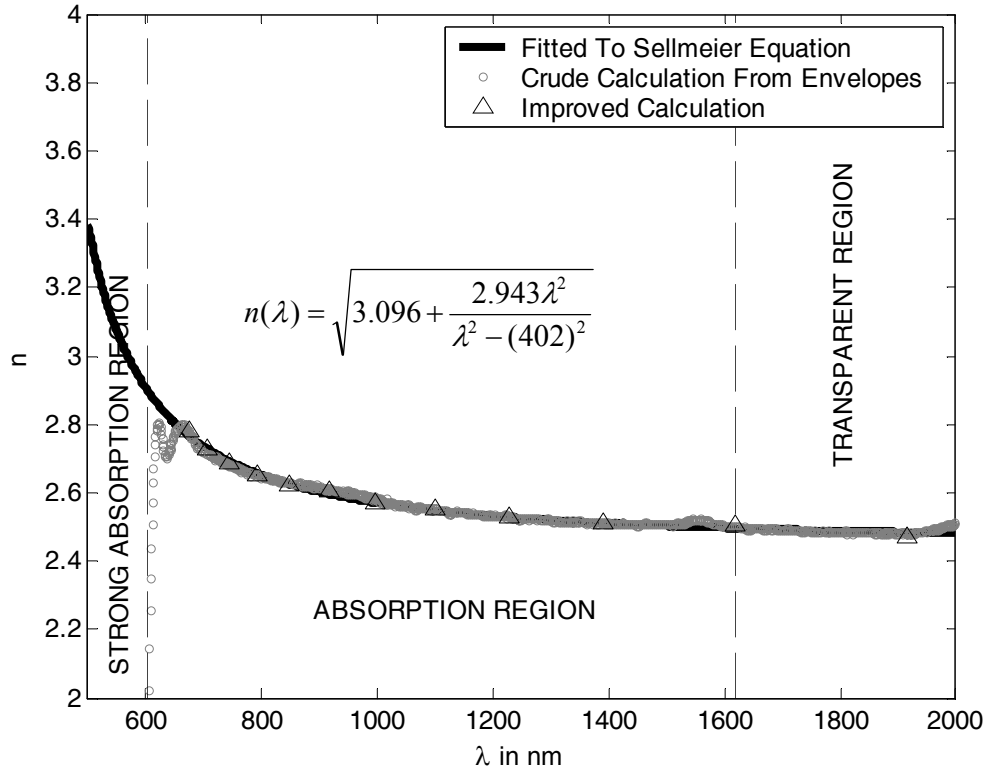
Figure 4.9: The fitting of the calculated refractive index of an 0.969μm *a*-Se thin film to the Sellmeier equation. The improved calculation will be explained later in the section.

4.3.3.2 Thickness

Using the calculated refractive index at any adjacent maximas (or minimas), the thickness can be easily calculated. From Equations (4.6) and (4.7), it can be seen that the transmittance will reach a local maximum (or minimum) whenever $\varphi = 2m\pi$, where $m = 0,1,2,3,\dots$ is any integer if T is a maxima or $m = 0.5, 1.5, 2.5, \dots$ is any half integer if T is a minima. Substituting φ into equation (4.7) and rearranging it for m we will have,

$$m = \frac{2nd}{\lambda}.$$

4.14

Thus the difference between any two adjacent maximas (or minimas) will be,

$$\frac{2n_{m+1}d}{\lambda_{m+1}} - \frac{2n_m d}{\lambda_m} = (m+1) - m \text{ and}$$

$$d_{\text{crude}} = \frac{\lambda_m \lambda_{m+1}}{2(\lambda_m n_{m+1} - \lambda_{m+1} n_m)},$$

4.15

75

where λ_m and λ_{m+1}, are the wavelengths at any two adjacent maximas (or minimas), and n_m and n_{m+1}, are the refractive indices at the corresponding wavelengths.

4.3.3.3 Absorption Coefficient

The absorption coefficient can be obtained from equation (4.8) once the absorbance, x, is extracted from the transmission spectrum. This can be done by rearranging equation (4.6e) into a quadratic equation in x and solving this quadratic equation for x. In other words, from the equation (4.6e) we will have,

$$(T_M D)x^2 - (T_M C + A)x + T_M B = 0.$$ 4.16

Solving this quadratically we have,

$$x = \frac{E_M - \sqrt{E_M^2 - (n^2 - 1)^3 (n^2 - s^4)}}{(n-1)^3 (n - s^2)},$$ 4.17

where

$$E_M = \frac{8n^2 s}{T_M} + (n^2 - 1)(n^2 - s^2),$$ 4.17a

T_M is the maxima envelope constructed from the measured transmission spectrum and, n and s, are the refractive index of the film and substrate respectively. Thus from equation (4.8) we have,

$$\alpha = -\frac{\ln(x)}{d_{ave}},$$ 4.18

where x is the absorbance and d_{ave} is the average of those thicknesses calculated from equation (4.15) for each set of adjacent maximas (or minimas).

4.3.3.4 Improved Accuracy

The accuracy of the thickness, the refractive index, and the absorption coefficient can all be further improved by iteratively applying equation (4.14) in a systematic manner as follows:

First of all, a set of order number m for the interference fringes was calculated using equation (4.14),

$$m = \frac{2n_e d_{ave}}{\lambda_e},$$
<div align="right">4.14a</div>

where n_e and λ_e are the values taken at the extreme point of the interference fringes and d_{ave} is the average of d_{crude} from equation (4.15).

This order number m was rounded either to the nearest integer if the n_e and λ_e taken were at a maxima or the nearest half-integer if the n_e and λ_e taken were at a minima. It is then used to obtain a new corresponding set of thicknesses d' by rearranging equation (4.14a) into,

$$d' = \frac{m\lambda_e}{2n_e}.$$
<div align="right">4.14b</div>

A new average thickness d_{new} from d' can now be calculated and used for a new refractive index by rearranging equation (4.14a) into

$$n'_e = \frac{m\lambda_e}{2d_{new}}.$$
<div align="right">4.14c</div>

This refractive index was then fitted to a dispersion model for extrapolation into the strong absorption region so that a new absorption coefficient α can be calculated from equation (4.17) and (4.18). These optical constants were substituted into equation (4.6) to regenerate the transmission spectrum $T_{cal}(\lambda)$, so that the root mean square error (RMSE) can be determined from the experimental spectrum T_{exp} as follows:

$$\text{RMSE} = \sqrt{\frac{\sum_{i=1}^{q}\left(T_{expi} - T_{cali}\right)^2}{q}},$$
<div align="right">4.19</div>

where T_{exp} is the transmittance of the experimental or measured spectrum, T_{cal} is the transmittance of the regenerated spectrum using the optical constants obtained from the Swanepoel method and q is the range of the measurement.

Keeping these optical constants that have just been determined aside, the whole process starting from equation (4.14a) must now be repeated for another set of optical constants and its corresponding RMSE. In other words, the new set of order numbers will be,

$$m' = \frac{2n_e d'_{\mathrm{ave}}}{\lambda_e} ,$$ 4.14d

where d'_{ave} is the new average thickness calculated by ignoring the first two d_{crude} values from equation (4.15). Using these new order numbers, there will eventually be another RMSE that corresponds to this new average thickness. When this was done, the process is repeated for yet another RMSE but this time the first four d_{crude} values calculated from equation (4.15) will be ignored during averaging. The iteration ends when there is no more d_{crude} to ignore and the set of optical constants that most accurately regenerated the transmission spectrum can be isolated using the RMSE values.

The tables below illustrate briefly the process of how all the parameters of an a-Se thin film of 0.9687μm thick can be improved systematically and Figure 4.10 shows the regenerated transmission spectrum of this sample using the extracted optical constants determined from the Swanepoel method.

Table 4-1: Iteration=0: d_{ave} = the average of d_{crude} from row # 1 to 12

No.	λ_e (in nm)	T_M	T_m	n_e	d_{crude} (μm)	m	d' (μm)	n'_e
1	627	0.56	0.4	2.7699	1.7469	9.5	1.0752	2.777
2	643	0.71	0.47	2.7278	1.2803	9	1.0607	2.6979
3	673	0.87	0.53	2.7804	0.9428	8.5	1.0287	2.6669
4	704	0.9	0.55	2.7117	0.9913	8	1.0385	2.6257
5	744	0.91	0.57	2.6792	1.0028	7.5	1.0413	2.6014
6	791	0.91	0.58	2.6478	1.0003	7	1.0456	2.5814
7	847	0.91	0.58	2.6278	0.9945	6.5	1.0475	2.5667
8	917	0.91	0.59	2.6112	0.9465	6	1.0535	2.5651
9	996	0.91	0.59	2.5893	0.931	5.5	1.0578	2.5539
10	1100	0.91	0.6	2.5512	0.9726	5	1.0779	2.5641
11	1226	0.91	0.61	2.5288	0.9663	3.5	1.0908	2.5721
12	1390	0.91	0.61	2.5092	0.9836	4	1.1079	2.5921
13	1617	0.92	0.61	2.4986	N.A.	3.5	1.1325	2.6385
14	1915	0.92	0.62	2.4835	N.A.	3	1.1566	2.6784
				d_{ave} (1-12)	1.0632		RMSE	0.22

Table 4-2: Iteration=1: d_{ave} = the average of d_{crude} from row # 3 to 12

No.	λ_e (in nm)	T_M	T_m	n_e	d_{crude} (μm)	m'	d' (μm)	n'_e
1	627	0.56	0.4	2.7699	1.7469	9	1.0186	2.8953
2	643	0.71	0.47	2.7278	1.2803	8.5	1.0018	2.8042
3	673	0.87	0.53	2.7804	0.9428	8	0.9682	2.7624
4	704	0.9	0.55	2.7117	0.9913	7.5	0.9736	2.7091
5	744	0.91	0.57	2.6792	1.0028	7	0.9719	2.6721
6	791	0.91	0.58	2.6478	1.0003	6.5	0.9709	2.638
7	847	0.91	0.58	2.6278	0.9945	6	0.967	2.6075
8	917	0.91	0.59	2.6112	0.9465	5.5	0.9657	2.5877
9	996	0.91	0.59	2.5893	0.931	5	0.9616	2.5551
10	1100	0.91	0.6	2.5512	0.9726	3.5	0.9701	2.5397
11	1226	0.91	0.61	2.5288	0.9663	4	0.9696	2.5161
12	1390	0.91	0.61	2.5092	0.9836	3.5	0.9694	2.4961
13	1617	0.92	0.61	2.4986	N.A.	3	0.9707	2.4889
14	1915	0.92	0.62	2.4835	N.A.	2.5	0.9639	2.4564
				d'_{ave} (3-12)	0.9732		RMSE	0.0092

Table 4-3: Iteration=5: d_{ave} = the average of d_{crude} from row # 11 to 12

No.	λ_e (in nm)	T_M	T_m	n_e	d_{crude} (µm)	m'	d' (µm)	n'_e
1	627	0.56	0.4	2.7699	1.7469	9	1.0186	2.8953
2	643	0.71	0.47	2.7278	1.2803	8.5	1.0018	2.8042
3	673	0.87	0.53	2.7804	0.9428	8	0.9682	2.7624
4	704	0.9	0.55	2.7117	0.9913	7.5	0.9736	2.7091
5	744	0.91	0.57	2.6792	1.0028	7	0.9719	2.6721
6	791	0.91	0.58	2.6478	1.0003	6.5	0.9709	2.638
7	847	0.91	0.58	2.6278	0.9945	6	0.967	2.6075
8	917	0.91	0.59	2.6112	0.9465	5.5	0.9657	2.5877
9	996	0.91	0.59	2.5893	0.931	5	0.9616	2.5551
10	1100	0.91	0.6	2.5512	0.9726	3.5	0.9701	2.5397
11	1226	0.91	0.61	2.5288	0.9663	4	0.9696	2.5161
12	1390	0.91	0.61	2.5092	0.9836	3.5	0.9694	2.4961
13	1617	0.92	0.61	2.4986	N.A.	3	0.9707	2.4889
14	1915	0.92	0.62	2.4835	N.A.	2.5	0.9639	2.4564
				d'_{ave} (11-12)	0.9749		RMSE	0.0145
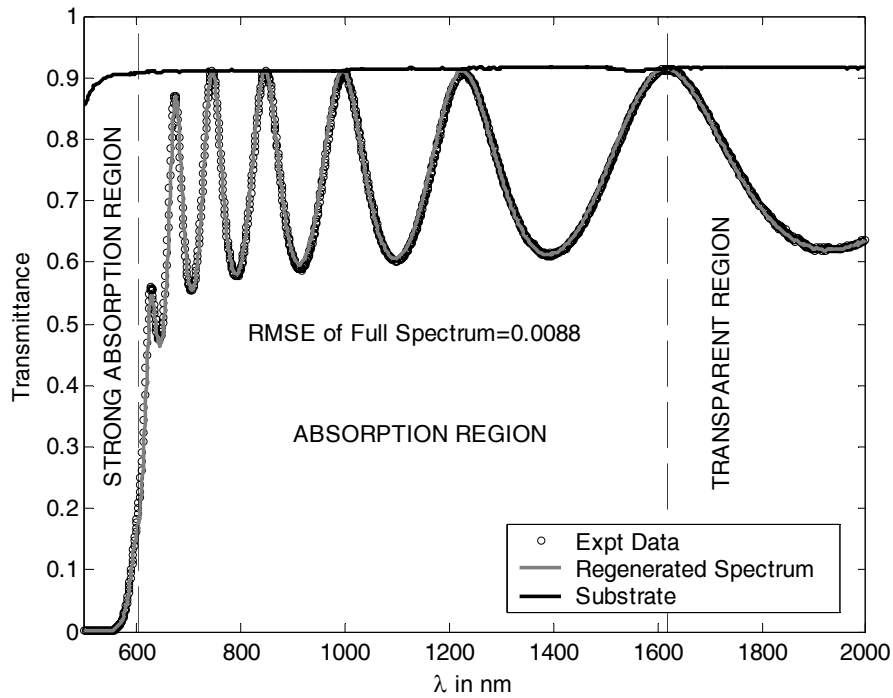
Figure 4.10: Transmission spectrum of both the measured values and the regenerated values of an 0.969µm *a*-Se thin film using the Swanepoel method.

4.3.4 Thin Film with Non-Uniform Thickness

4.3.4.1 Roughness

According to Swanepoel, the integral in Equation (4.9) in the transparent region where $x = 1$ will work out to be,

$$T_{\Delta d} = \left(\frac{\lambda}{4\pi n \Delta d} \frac{a}{\sqrt{1-b^2}} \right)$$
$$\times \left[\tan^{-1} \left(\frac{1+b}{\sqrt{1-b^2}} \tan \frac{\varphi_2}{2} \right) - \tan^{-1} \left(\frac{1+b}{\sqrt{1-b^2}} \tan \frac{\varphi_1}{2} \right) \right]$$

4.19

where

$$a = \frac{A}{B+D},$$

4.19a

$$b = \frac{C}{B+D},$$

4.19b

with

$$\varphi_1 = \frac{4\pi n(\bar{d} - \Delta d)}{\lambda},$$

4.9a

$$\varphi_2 = \frac{4\pi n(\bar{d} + \Delta d)}{\lambda},$$

4.9b

$$A = 16n^2 s,$$

4.6a

$$B = (n+1)^3(n+s^2),$$

4.6b

$$C = 2(n^2-1)(n^2-s^2),$$

4.6c

$$D = (n-1)^3(n-s^2),$$

4.6d

n, s, and α are all function of wavelength, λ, $d = \bar{d} \pm \Delta d$, $\bar{d}$ is the average thickness of the film and Δd is the roughness of the film.

Since the integration can not be carried out from one branch of the tangent to another, it can not be used directly in this form. The equation was thus modified by considering the maxima and minima, which are both continuous function of λ, in a case by case basis.

As a result we will have,

Maxima: $\qquad T_{Md} = \dfrac{\lambda}{2\pi n \Delta d} \dfrac{a}{\sqrt{1-b^2}} \tan^{-1}\left[\dfrac{1+b}{\sqrt{1-b^2}} \tan\left(\dfrac{2\pi n \Delta d}{\lambda}\right)\right],$ $\qquad\qquad$ 4.20a

Minima: $\qquad T_{md} = \dfrac{\lambda}{2\pi n \Delta d} \dfrac{a}{\sqrt{1-b^2}} \tan^{-1}\left[\dfrac{1-b}{\sqrt{1-b^2}} \tan\left(\dfrac{2\pi n \Delta d}{\lambda}\right)\right],$ $\qquad\qquad$ 4.20b

As long as $0 < \Delta d < \lambda/4n$, the refractive index, n and the roughness, Δd can both be obtained simultaneously by solving Equations (4.20ab) numerically.

Although Swanepoel did not recommend using the refractive index acquired here for any calculation because α is never zero, there were instances where it was used for the calculation of thickness directly [66].

4.3.4.2 Average Thickness, Refractive Index and Absorption Coefficient outside of Strong Absorption Region

Since Equations (4.20a) and (4.20b) are only valid in the region of zero absorption, the refractive index outside of the transparent region must be obtained in another way. Theoretically, a direct integration of equation (4.9) over both Δd and x must be performed, however this would be analytically too difficult. Nevertheless an approximation to the integration in equation (4.9) is possible and is given by,

$$T_{\Delta d} = \frac{1}{\varphi_2 - \varphi_1} \int_{\varphi_1}^{\varphi_2} \frac{Ax}{B - Cx\cos\varphi + Dx^2} dx .$$ $\qquad\qquad$ 4.9

If $\Delta d << d$, the absorbance x can be assumed to have some constant average value just over the range of integration with respect to the roughness Δd. Therefore if $0 < x \leq 1$,

$$T_{\Delta d} \approx \left(\frac{\lambda}{4\pi n \Delta d} \frac{a}{\sqrt{1-b^2}}\right) $$
$$\times \left[\tan^{-1}\left(\frac{1+b}{\sqrt{1-b^2}} \tan\frac{\varphi_2}{2}\right) - \tan^{-1}\left(\frac{1+b}{\sqrt{1-b^2}} \tan\frac{\varphi_1}{2}\right)\right]$$ $\qquad\quad$ 4.19

Once again, this equation can be modified by considering the maxima and minima envelopes separately and we have,

Maxima: $$T_{Mx} = \frac{\lambda}{2\pi n \Delta d} \frac{a_x}{\sqrt{1-b_x^2}} \tan^{-1}\left[\frac{1+b_x}{\sqrt{1-b_x^2}} \tan\left(\frac{2\pi n \Delta d}{\lambda} \right) \right],$$ 4.21a

Minima: $$T_{mx} = \frac{\lambda}{2\pi n \Delta d} \frac{a_x}{\sqrt{1-b_x^2}} \tan^{-1}\left[\frac{1-b_x}{\sqrt{1-b_x^2}} \tan\left(\frac{2\pi n \Delta d}{\lambda} \right) \right],$$ 4.21b

where $$a = \frac{Ax}{B+Dx^2},$$ 4.21c

$$b = \frac{Cx}{B+Dx^2},$$ 4.21d

n and s are both the refractive index of the film and substrate respectively and Δd is the roughness of the film.

As long as $0 < x \leq 1$, numerically there will only be one unique solution for the two desired optical properties, which is the refractive index n and the absorbance x. They can both be obtained when Equations (4.21a) and (4.21b) are solved simultaneously using the average roughness, $\Delta \bar{d}$, calculated from (4.20ab). However, given that Equations (4.21a) and (4.21b) are not valid in the strong absorption region, because there are no interferences fringes, the absorption coefficient α_{ns} calculated from the absorbance x is obtained as follows,

$$\alpha_{ns} = -\frac{\ln(x)}{\bar{d}_{ave}},$$ 4.18a

where x is the absorbance obtained from Equations (4.21a) and (4.21b) and $\bar{d}_{ave}$ is the average thickness of $\bar{d}$ which is itself obtained from equation (4.15) as shown,

$$\bar{d} = \frac{\lambda_1 \lambda_2}{2(\lambda_1 n_2 - \lambda_2 n_1)},$$ 4.15

where λ_1 and λ_2, are the wavelengths at two adjacent maximas (or minimas), and n_1 and n_2, are the corresponding refractive indices at these wavelengths.

For the absorption coefficient in the strong absorption region, the calculated refractive index must first be fitted to a dispersion model, such as the Sellmeier or Cauchy equation, for extrapolation to shorter wavelengths before they can be used to obtain any absorption coefficient in this region. Figure 4.11 shows the Cauchy fitted refractive index of a sample with a simulated spectrum.

The plot shows the refractive index n versus λ in nm, with the fitted Cauchy equation:

$$n(\lambda) = 2.587 + \frac{24.61}{\lambda} + \frac{2.876 \times 10^5}{\lambda^2}$$

Legend: Fitted To Cauchy Equation; ○ Crude Calculation From Envelopes; △ Improved Calculation. Labeled regions: STRONG ABSORPTION REGION and ABSORPTION REGION.
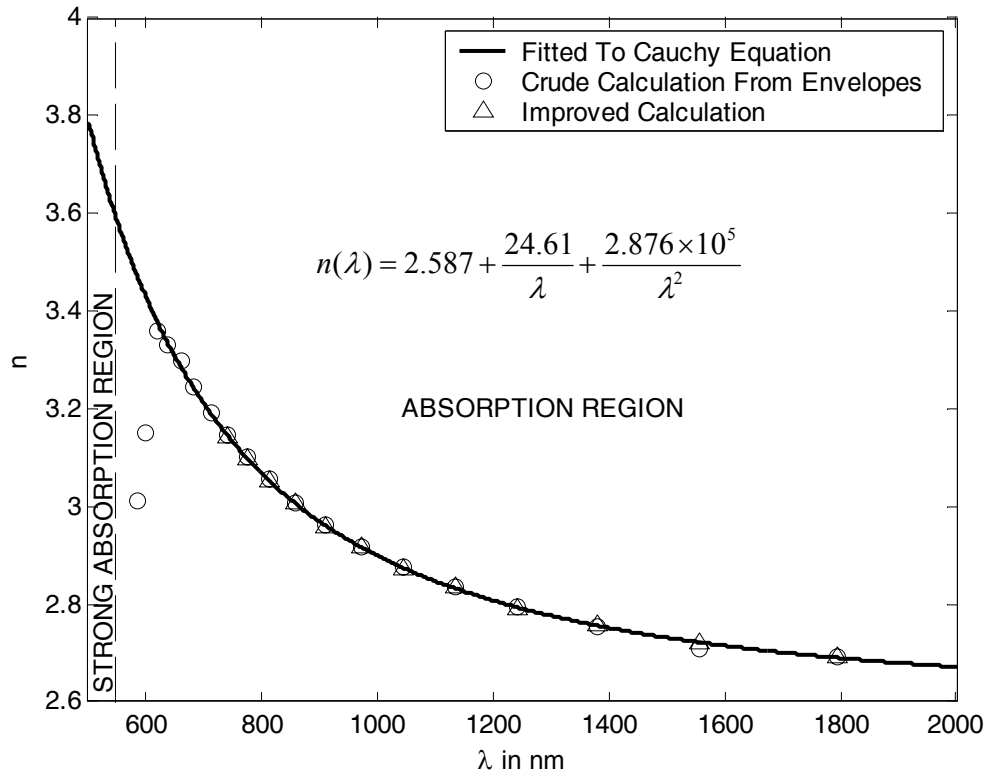
Figure 4.11: The refractive index of a sample with $\bar{d} = 1.0\mu m$ and $d = 30nm$, and n fitted to a Cauchy equation.

4.3.4.3 Absorption Coefficient in Strong Absorption

According to Swanepoel, in the region of strong absorption, the interference fringes are smaller and the spectrum approaches the interference-free transmission sooner. Since the transmission spectrums in this region are the same for any films with the same average thickness, regardless of its uniformity, the absorption coefficient of a non-uniform film can be derived from Equations (4.6e) and (4.6f) as follows: Given

$$T_M = \frac{Ax}{B - Cx + Dx^2},$$
$$\text{4.6e}$$

$$T_m = \frac{Ax}{B + Cx + Dx^2},$$
$$\text{4.6f}$$

then
$$\frac{1}{T_M} + \frac{1}{T_m} = \frac{2(B + Dx^2)}{Ax}$$

or
$$(T_i D)x^2 - Ax + T_i B = 0,$$
$$\text{4.22}$$

Solving quadratic equation (4.22a) for x, we will have,

$$x_s = \frac{A - \sqrt{(A^2 - 4T_i^2 BD)}}{2T_i D},$$
$$\text{4.23}$$

where

$$T_i = \frac{2T_M T_m}{T_M + T_m},$$
$$\text{4.23a}$$

T_M *and* T_m are the envelopes constructed from the measured spectrum.

Once the absorbance is obtained, the absorption coefficient will just be,

$$\alpha_s = -\frac{\ln(x_s)}{\bar{d}_{ave}},$$
$$\text{4.22c}$$

where x_s is the absorbance obtained from Equations (4.22) and $\bar{d}_{ave}$ is the average thickness of $\bar{d}$ from equation (4.15).

4.3.4.4 Improved Accuracy

The accuracy of the thickness and refractive index can be further improved in exactly the same way as described in section 4.3.3.4 for a uniform film. As for the absorption coefficient, Equations (4.21a), (4.21b) and (4.23) were used for the computation of the refractive index *n* and the absorbance *x* instead of Equations (4.11) and (4.17). Figure 4.12 shows the regenerated transmission spectrum of a simulated sample with non uniform thickness using the optical constants calculated from the Swanepoel method.
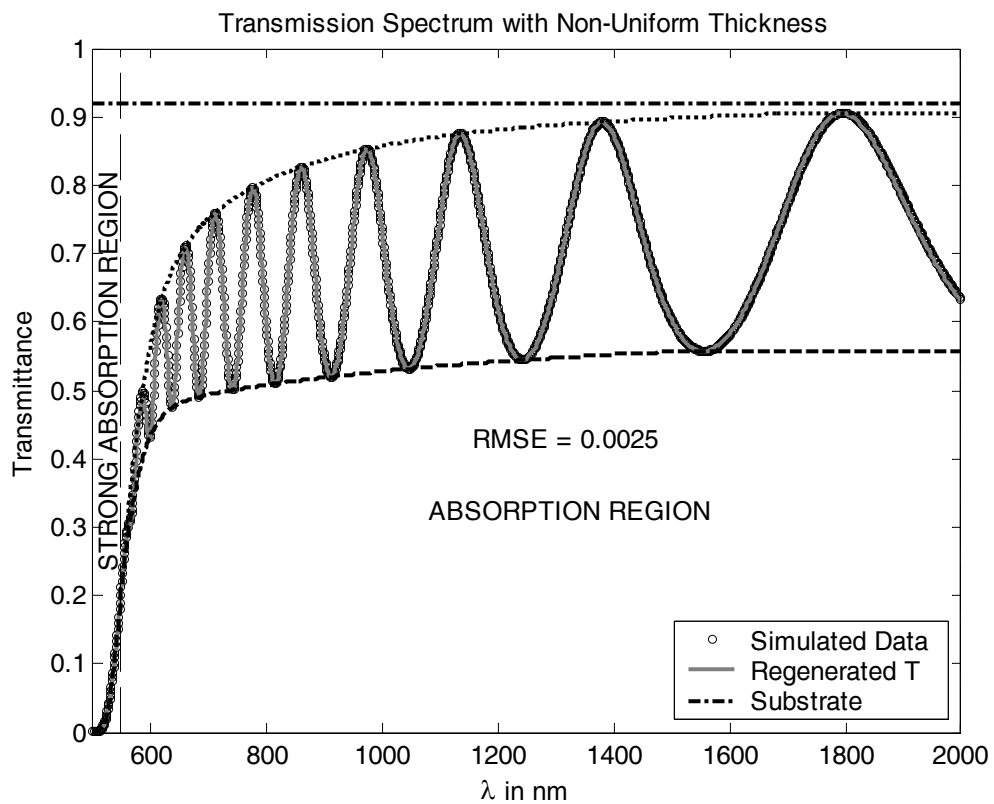
Figure 4.12: A regenerated transmission spectrum of a sample with an average thickness of 1.0μm, average Δ*d* of 30 nm, and a refractive index fitted to the Cauchy equation shown in Figure 4.11.

4.3.5 Optical Bandgap

Depending on its thickness, there are two ways to obtain the optical bandgap of a thin film material. If the thickness is too thick, which is usually anything greater than 10μm, then due to the limitations of the spectrometer, the extracted absorption coefficient will have values $\alpha < 10^4 \text{cm}^{-1}$. In this case, the method used to locate the optical bandgap will be the same as the one used for a bulk sample. In another words, the optical bandgap will be taken to be the photon energy at $\alpha = 10^4 \text{cm}^{-1}$ from the linear portion of the absorption coefficient curve. For any sample that reaches the upper detection limit of its absorption coefficient, extrapolation of the linear portion, anywhere below the upper limit, to the point at $\alpha = 10^4 \text{cm}^{-1}$ has to be done before the optical bandgap can be obtained. This is as shown in Figure 4.5.

However, if the thickness of the sample is in the range of values where the absorption coefficient is mostly $\alpha \geq 10^4 \text{cm}^{-1}$, then according to Tauc [67], it will have a frequency dependency in such a way that:

$$\alpha \hbar \omega(\omega) \sim (\hbar \omega - E_g^{opt})^r \tag{4.25}$$

where r is a constant of the order of 1. This equation was derived from considering, the observed absorption behavior in the high absorption region together with the density of states from the Mott-CFO model and the hypothesis from Davis and Mott, which argued against any factors enhancing the absorption in amorphous solids. The exponent r in Equation (4.25) is obtained by fitting the absorption coefficient extracted from the Swanepoel technique to the Equation (4.25). Once the exponent is known, a plot of $(\alpha \hbar \omega)^{1/r}$ against $\hbar \omega$ can be constructed. In this plot, the optical bandgap was taken to be the intersection of the extrapolated linear portion of $(\alpha \hbar \omega)^{1/r}$ and the x-axis. This is illustrated in Figure 4.13.
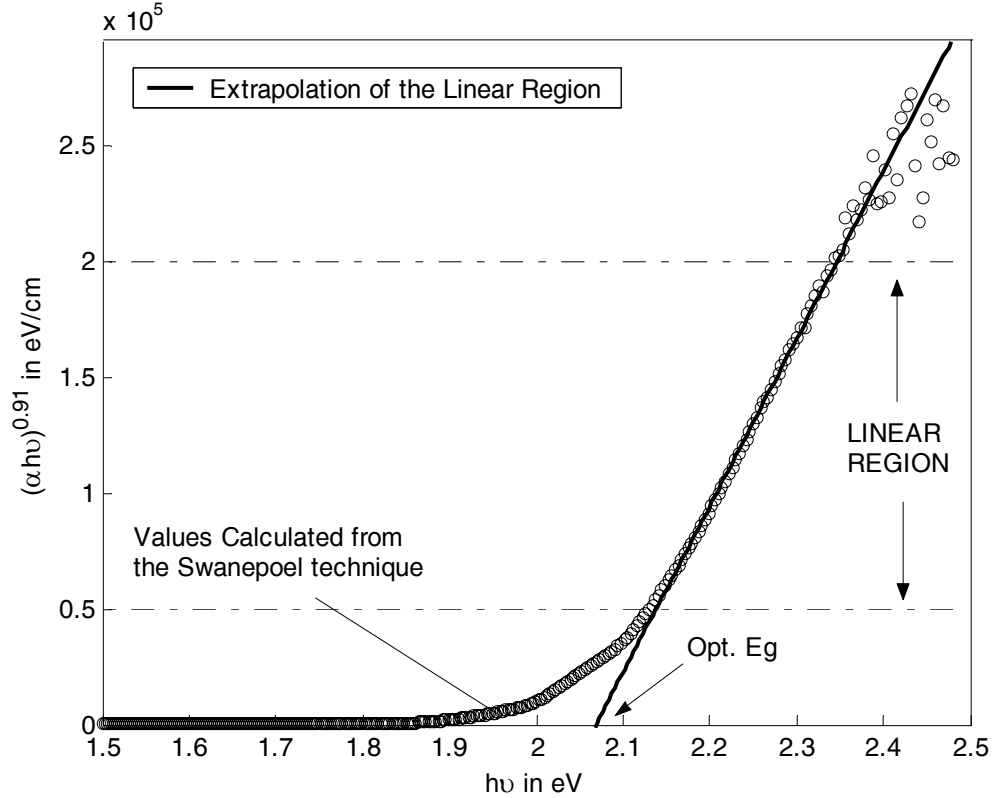
Figure 4.13: Determination of the Optical bandgap in the $\alpha \geq 10^4 \text{cm}^{-1}$ region for an *a*-Se film $0.9687\mu m$ thick.

4.4 Error Analysis

Since all the optical properties described in this work are extracted from the envelopes of the transmission spectrum, the accuracy of our calculation would be strongly dependent on the reliability of the transmittance values. For a thin film with an uniform thickness, the error in the calculation of the optical properties extracted using the Swanepoel technique can be computed in the following way [68, 69]. According to reference [69], the relative error in the refractive index of a uniform film is,

$$\frac{\Delta n}{n} = \frac{-\Delta T}{T}\left(\frac{T_M + T_m}{T_M - T_m}\right)\left(\frac{2(n^2 - s)}{(n^2 - 1)}\frac{(n^2 + s)}{(n^2 - s^2)}\right) \tag{4.26}$$

where $\Delta T/T$ is the photometric accuracy of the spectrometer if no sample mask is used in the measurement. Otherwise, $\Delta T/T$ is the relative error of the noise signal in the transmittance of a blank sample, i.e. a mask with no sample on it. T_M and T_m of Equation

(4.26) are the envelopes, n is the calculated refractive index and s is the refractive index of the substrate.

In this project, the majority of our measurements were done with a mask behind the sample and the noise in the measured transmittance of our spectrometer was calculated to be $\Delta T/T = 0.178\%$ for $500\text{nm} < \lambda < 2000\text{nm}$. Using the results obtained for a hot deposited pure a-Se film of about 976nm thick, we will have a maximum relative error of $\Delta n/n = 0.244\%$ in the refractive index. Since the thickness is from Equation (4.14), the relative error in the thickness will be,

$$\frac{\Delta d}{d} = \frac{\Delta n}{n} \tag{4.27}$$

So the maximum relative error of our thickness calculation is also $\Delta d/d = 0.244\%$.

The Swanepoel method was also checked for precision by measuring the transmission spectrum of a hot deposited $2.3\mu\text{m}$ a-Se film 10 consecutive times and comparing the results obtained. The table below shows the mean, the standard deviation and the relative error for the refractive index n, the optical bandgaps, Eg_T and Eg_U and Urbach width, ΔE.

Table 4-4: The precision of the Swanepoel technique, Sample: a-Se film, $T_s = 51°C$, $d = 2.3\mu\text{m}$

RUN #	d (μm)	n (at λ = 2000nm)	Eg_T (eV)	Eg_U (eV)	ΔE (eV)
1	2.311	2.642	1.999	2.020	0.0726
2	2.311	2.642	1.999	2.020	0.0728
3	2.312	2.640	1.999	2.020	0.0731
4	2.310	2.643	1.999	2.020	0.0733
5	2.310	2.642	2.000	2.020	0.0730
6	2.311	2.643	1.999	2.020	0.0735
7	2.307	2.646	1.998	2.020	0.0735
8	2.310	2.643	1.999	2.019	0.0728
9	2.311	2.642	1.998	2.020	0.0735
10	2.310	2.643	1.999	2.020	0.0739
Mean	2.310	2.642	1.999	2.020	0.0732
Standard Deviation	1.333×10^{-3}	1.343×10^{-3}	5.082×10^{-4}	3.302×10^{-4}	4.083×10^{-4}
Relative Error	0.058%	0.051%	0.025%	0.016%	0.558%

4.5 Summary

Basically, the amount of light that gets transmitted through a thin film material depends on the amount of reflection and absorption that takes place along the light path. There will be interference fringes on the transmission spectrum if it is a thin film with moderate absorption coefficient. The absorption coefficient of a thick sample can be obtained either from the measured reflectance or by using the transmittance and thickness of the sample. The refractive index is assumed to be the same as those from a thin film. In the $\alpha < 10^4 \text{cm}^{-1}$ region, the optical bandgap of a thick sample is taken to be the photon energy at 10^4cm^{-1} from an extrapolation of the linear portion of the absorption coefficient when it is plotted semi-logarithmically against the photon energy. In the $\alpha \geq 10^4 \text{cm}^{-1}$ region, the optical bandgap is obtained by fitting α to the generalized Tauc equation, $\alpha h\upsilon = A(h\upsilon - E_g)^r$.

For a thin film with interference fringes in its transmission spectrum, two equations derived by Swanepoel accurately described the spectrum. Basically all the optical constants can be calculated from these two equations using the envelopes constructed from the minima and maxima of the transmission spectrum. All the optical constants are further improved by taking different averages iteratively.

For a non-uniform film, the thickness variations must first be determined before the other optical constants can be calculated. This can be done by solving the respective equations simultaneously in a numerical way. With the roughness known, the refractive index and the absorbance can both be determined and the refractive index can be fitted to a dispersion model for values at shorter wavelengths. The optical constants were improved in exactly the same way as that for a uniform film.

The Swanepoel technique was applied to all the thin a-Se films in this work. The chapter considered one film as an example of the technique and how the improved version can provide a reasonably accurate set of optical constants as a function of wavelength. The Sellmeier dispersion equation was used to model the refractive index vs photon energy

dependence. The best fit to the absorption coefficient vs $h\upsilon$ data above the Urbach edge did not follow the standard Tauc relation but indicated a behavior in which ($\alpha h\upsilon$) increases linearly with $h\upsilon$ in agreement with other work on a-Se [15]. The Urbach tail was obtained from a semi-logarithmic plot of α vs $h\upsilon$ in $\alpha < 10^4 \text{cm}^{-1}$ region.

Various computer algorithms that can be used to obtain n and K were based on the Swanepoel technique and they are available in the literature [70, 71, 72]. Marquez et. al. [73] discuss the application of Swanepoel technique to a wedge-shaped As_2S_3 thin film and make use of the fact that a non-uniform wedge-shaped thin film has a compressed transmission spectrum. There are also numerous useful applications of the Swanepoel technique for extracting the optical constants of thin films; some selected recent examples are [74,75,76,77,78,79,80,81,82,83].

5. The Dependence of the Optical Properties on Thickness, Thermal Annealing and Aging

This chapter is divided into 5 sections. The first section deals with the thermal relaxation of the optical properties of amorphous selenium films. The second section reports on the dependence of the optical properties of pure amorphous selenium films on the film thickness and the last 3 sections describe how the optical properties changes with the doping of 67ppm of chlorine, the deposition temperature and time.

All the thin films under investigation were prepared by vacuum evaporation techniques as described in Section 3.3 and were kept in complete darkness between measurements at an ambient temperature of $T_{room} \approx 20°C$. Their transmission spectra were obtained from a spectrophotometer shown in Figure 3.4 and their optical properties were extracted using the analytical methods described in Chapter 4.

5.1 The Thermal Relaxation of the Optical Properties of Amorphous Selenium

In this part of the experiment, the transmission spectrum of a virgin (as-evaporated) film, deposited at a substrate temperature of T_s=51°C, was taken regularly for a week before it was put into the vacuum chamber shown in Figure 3.2. The film was then thermally annealed in vacuum for an hour at T_a=51°C using the substrate heater. The annealing temperature is above the glass transition temperature of a-Se, which is about 40°C.

Table 5.1 compares the optical properties of the virgin (as-evaporated) and annealed (thermally relaxed) a-Se films according to their aging times. From Table 5.1, it can be seen that there is a significant decrease, an average of 15%, in the film thickness when the film was annealed for an hour. Moreover, the optical bandgap Eg_T and the refractive

index at long wavelengths have also increased by an average of 0.23% and 0.45% respectively. The optical bandgap Eg_U, on the other hand is relatively constant and deviates less than 0.04% after annealing.

Table 5-1: Thermal relaxation of the optical properties of a-Se films deposited at T_s=51°C.

Aged (hrs)	SAMPLE	d (um)	Δd (nm)	Eg_T (eV)	Eg_U (eV)	n (at λ=2000nm)	RMSE
1.08	As deposited a-Se T_s=51°C	3.940±0.009	0	1.994	2.049	2.441±0.006	1.20%
1.17	Annealed a-Se T_a=51°C 1hr	3.349±0.008	0	1.997	2.049	2.456±0.006	1.10%
	Relative Change (%)	-15.00%		0.19%	-0.03%	0.62%	
50	As deposited a-Se T_s=51°C	3.939±0.009	0	1.996	2.051	2.442±0.006	1.20%
52	Annealed a-Se T_a=51°C 1hr	3.355±0.008	0	2.001	2.050	2.452±0.006	1.10%
	Relative Change (%)	-14.84%		0.25%	-0.08%	0.38%	
126	As deposited a-Se T_s=51°C	3.939±0.009	0	1.995	2.052	2.443±0.006	1.20%
120	Annealed a-Se T_a=51°C 1hr	3.356±0.008	0	2.000	2.051	2.452±0.006	1.10%
	Relative Change (%)	-14.79%		0.26%	-0.02%	0.36%	
AVE	As deposited a-Se T_s=51°C	3.939	0	1.995	2.051	2.442	1.20%
AVE	Annealed a-Se T_a=51°C 1hr	3.353	0	1.999	2.050	2.453	1.10%
	Relative Change (%)	-14.88%		0.23%	-0.04%	0.45%	

The decrease in the thickness signifies a decrease in the free volume and an increase in the density. This agrees with what has been reported in the literature for thermally relaxed chalcogenide films [84]. According to the authors [84], this thermally induced structural relaxation phenomenon is linked to the polymerization of molecular fragments embedded in the structure of the as-evaporated films. Since a-Se is thought to contain a mixture of ring and chain-like structures, it is not unusual to expect incompatible molecular clusters of chain or ring-like regions to form on the substrate when the film was made. The presence of such molecular clusters will lower the degree of cohesiveness between structural layers and thus increase the free volume in the material. This kind of molecular clustering is likely to be thermally unstable. As in the case of the thermally relaxed amorphous chalcogenide films in [84], the concentration of the incompatible clusters in a-Se film should also be greatly reduced through polymerization and cross-linking with the amorphous network during annealing. Put differently, the amorphous phase is reconfigured during annealing. When there are fewer incompatible

molecular clusters in the film, the free volume decreases and the thickness of the film shrinks.

Table 5-2: The parameters of curve fitting n to the *Wemple-DiDominico* relationship.

$$n_{\mathrm{WD}}^2 = 1 + \frac{E_o E_d}{E_o^2 - (h\upsilon)^2}$$

Aged (hrs)	SAMPLE	n_{WD} (at λ=2000nm)	E_o (eV)	E_d (eV)	RMSE of FIT (abs)
1.08	As deposited a-Se T_s=51°C	2.434	3.78	18.09	0.035
1.17	Annealed a-Se T_a=51°C 1hr	2.449	3.78	18.40	0.033
	Relative Change (%)	0.60%	0.21%	1.67%	
50	As deposited a-Se T_s=51°C	2.436	3.78	18.14	0.037
52	Annealed a-Se T_a=51°C 1hr	2.445	3.78	18.30	0.033
	Relative Change (%)	0.37%	0.00%	0.90%	
126	As deposited a-Se T_s=51°C	2.436	3.78	18.15	0.036
120	Annealed a-Se T_a=51°C 1hr	2.444	3.79	18.33	0.033
	Relative Change (%)	0.34%	0.16%	1.00%	
AVE	As deposited a-Se T_s=51°C	2.435	3.778	18.127	0.036
AVE	Annealed a-Se T_a=51°C 1hr	2.446	3.783	18.343	0.033
	Relative Change (%)	0.44%	0.12%	1.19%	

Table 5-2 shows the parameters obtained from fitting the Sellmeier represented refractive index to the *Wemple-DiDominico* dispersion relationship. The interesting thing to note here is that it shows an increase in the dispersion energy, E_d with annealing. From the *Wemple-DiDominico* relationship given in equation (2.18), the dispersion energy, $E_d = \beta N_c Z_a N_e$, where N_c is the effective coordination number of the cation nearest-neighbor to the anion. Since it is believed that there are charged centers, Se_1^- and Se_3^+, termed valence alternation pairs (VAP and IVAP), present in an a-Se structure, any decrease in the thickness would certainly enhance the interactions between structural layers and contribute to an increase in N_c. So any gain in the dispersion energy E_d after the film was annealed can be attributed to the drop in the thickness. Table 5-2 therefore provides additional evidence of the densification of the a-Se structure when it is annealed. When comparing the oscillator energy, E_o in Table 5-2 to Eg_T in Table 5.1 it was realized that $E_o \approx 1.9 \times Eg_T$. This is close to the value found in the literature [22, 84].

Table 5-3: Fitting parameters of the Sellmeier Dispersion Equation used for the extrapolation of the refractive index to shorter wavelengths in *a*-Se films.

Aged (hrs)	SAMPLE	n (at λ=2000nm)	$n^2 = A + \dfrac{B\lambda^2}{\lambda^2 - C^2}$		
			A (abs)	B (abs)	C (x10^{-9}) (abs)
1.08	As deposited *a*-Se T$_s$=51°C	2.441±0.006	4.184	1.678	465
1.17	Annealed *a*-Se T$_a$=51°C 1hr	2.456±0.006	4.301	1.636	469
	Relative Change (%)	0.62%	2.80%	-2.53%	0.86%
50	As deposited *a*-Se T$_s$=51°C	2.442±0.006	4.198	1.672	465
52	Annealed *a*-Se T$_a$=51°C 1hr	2.452±0.006	4.293	1.623	470
	Relative Change (%)	0.38%	2.27%	-2.88%	1.08%
126	As deposited *a*-Se T$_s$=51°C	2.443±0.006	4.213	1.659	466
120	Annealed *a*-Se T$_a$=51°C 1hr	2.452±0.006	4.326	1.590	472
	Relative Change (%)	0.36%	2.68%	-4.14%	1.29%
AVE	As deposited *a*-Se T$_s$=51°C	2.442	4.198	1.670	465
AVE	Annealed *a*-Se T$_a$=51°C 1hr	2.453	4.307	1.616	470
	Relative Change (%)	0.45%	2.58%	-3.18%	1.07%

Table 5-3 shows the fitting parameters for the refractive index obtained for the virgin and annealed *a*-Se films. Besides having an effect on the physical properties, annealing also affects the refractive index. Table 5-3 shows an increase in the refractive index at λ = 2000nm for all cases of aging time. The increase in the refractive index was across the entire spectral region under investigation and the dispersion model that best describes this refractive index is the Sellmeier Equation and it is graphically as shown in Figure 5.1.

This result again agrees with what has been reported for thermally relaxed chalcogenide films e.g. [84]. According to reference [84], the increase in the refractive index is related to the structural densification through the Lorentz–Lorenz (also referred to as Clausius-Mossotti) relationship as shown below:

$$\frac{n^2-1}{n^2+2} = \frac{1}{3\varepsilon_o}\sum_j N_j\alpha_{p_j}$$

5.1

where ε_o is the vacuum permittivity and N_j the number of polarizable units of type *j* per volume unit, with polarizability $\alpha_{p,j}$.
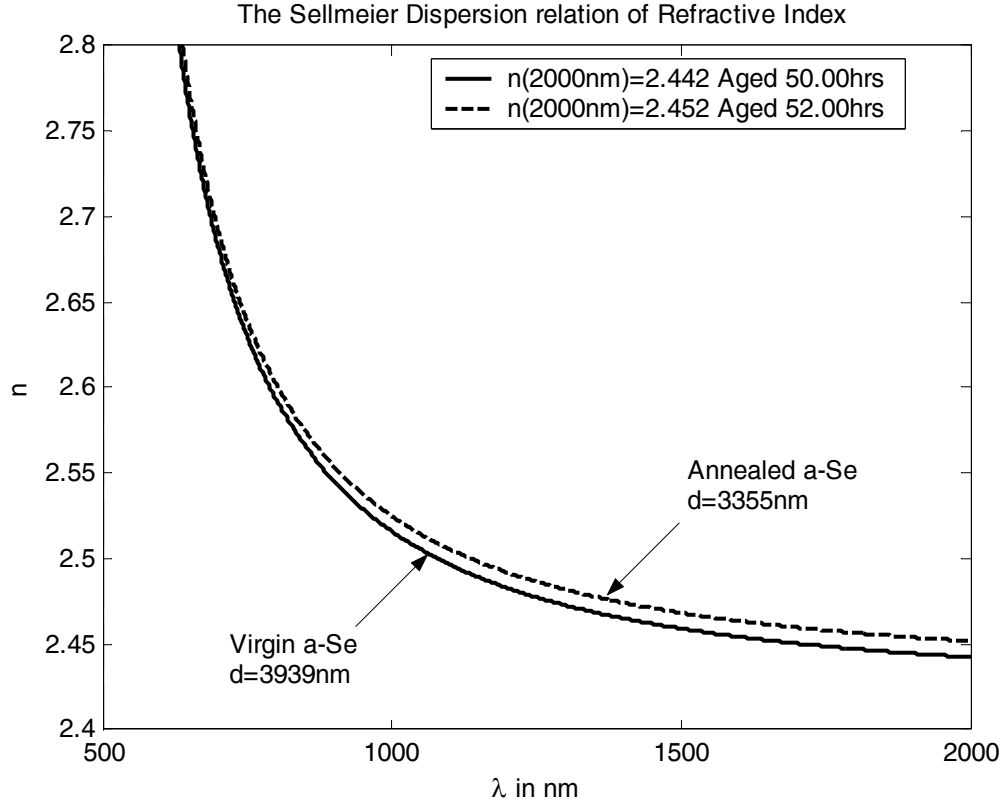
Figure 5.1: Thermal relaxation of the refractive index of an aged *a*-Se film.

It can be seen from this relationship that any increase in the concentration of polarizable units, N_j, after annealing (due to the thermally induced volume contraction), would lead to an increase in the refractive index. According to the author [84], Equation (5.1) can be rewritten to show the relationship between the changes in n and in the mass density ρ (or equivalently, the average film thickness) by neglecting possible changes in the polarizability:

$$\frac{\Delta n}{n} = \frac{(n^2 - 1)(n^2 + 2)}{6n^2} \frac{\Delta \rho}{\rho} \quad , \qquad\qquad 5.2a$$

$$\frac{\Delta n}{n} = \frac{-(n^2 - 1)(n^2 + 2)}{6n^2} \frac{\Delta \overline{d}}{\overline{d}} \quad . \qquad\qquad 5.2b$$

However, the relative changes found in the thickness after annealing do not account completely for the corresponding increases in the refractive index. In Table 5.1, the

average percentage change in the thickness was -14.88%. But according to equation (5.2b), the thickness needs only to shrink by 0.41% for it to cause an average increase of 0.45% in the refractive index. The differences between the experimentally-obtained relative changes for the refractive index and those derived from equation (5.2b) suggest that, apart from densification, notable changes in the effective polarizability of the material must be occurring as a consequence of the rearrangement of the bonds [84]. In other words, the polarizability, $\alpha_{p,j}$ must be changing.

Other than the thickness and the refractive index, Eg_T of the amorphous selenium film was found to increase slightly after the film was annealed. Although the changes are small compared to the other two properties, they are nonetheless noticeable graphically. Figure 5.3 and Figure 5.4 show how the extrapolated linear lines meant for locating the Eg_T and Eg_U were constructed respectively and Table 5-4 compare the results obtained from these two figures. It was noted from Table 5-4 that the optical bandgaps Eg_U and Eg_T would both change by an average of 0.04% and 0.23% respectively, after annealing. Although the relative changes in the optical bandgap Eg_U are very small, the Urbach width ΔE has increased by an average 2.21%. Additional evidence of an enlarged optical bandgap can be found in Figure 5.2. Figure 5.2 shows the transmission spectrum of the amorphous selenium films before and after annealing. It is obvious that the transmittance values from λ =585nm to 630nm for all cases of aging durations have increased and the entire transmission curve in this region has shifted horizontally to shorter wavelengths. This means that more radiation in this region is now able to pass through the sample and the optical bandgap at the fundamental absorption edge appears to have increased.
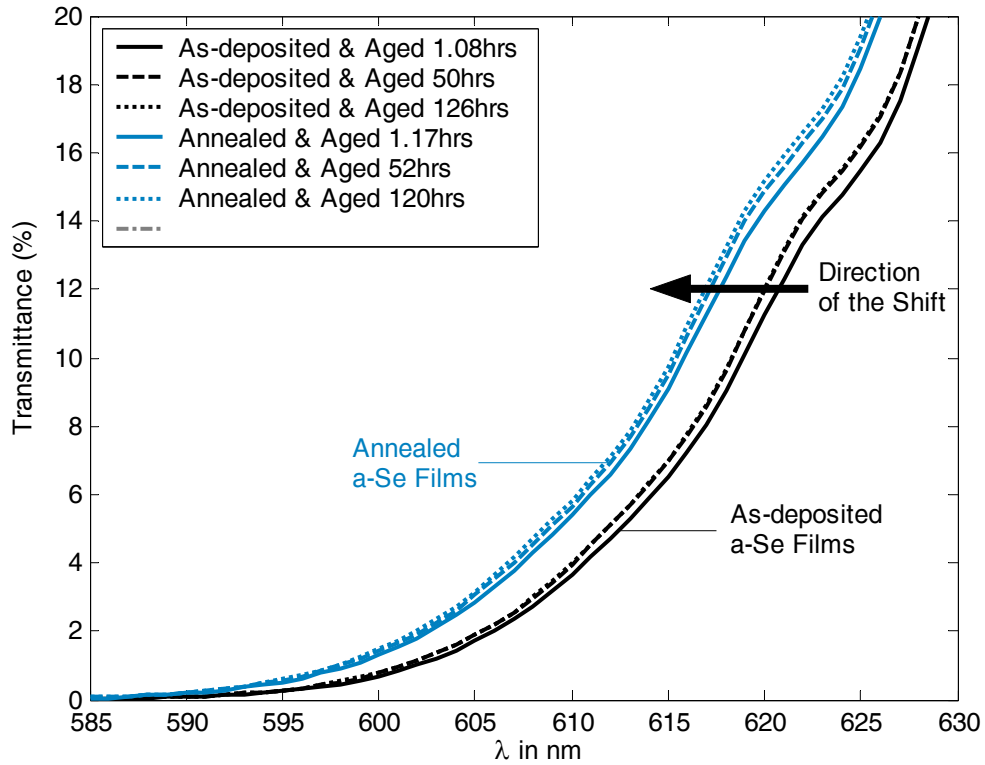
Figure 5.2: The shifting of the transmission spectrum in the strong absorption region of an annealed *a*-Se film.

Table 5-4: Fitting parameters from models used for the determination of the optical bandgaps in annealed *a*-Se films.

Aged (hrs)	SAMPLE	$\alpha h\upsilon = A(h\upsilon - Eg_T)$ ($\alpha \geq 10^4\,\text{cm}^{-1}$)		$\alpha = C\exp(h\upsilon/\Delta E)$ ($\alpha < 10^4\,\text{cm}^{-1}$)			RMSE
		A (x10^5) (eV/cm)	Eg_T (eV)	Eg_U (eV)	C (x10^{-10}) (cm^-1)	ΔE (eV)	
1.08	As deposited *a*-Se T$_s$=51°C	3.291	1.994	2.049	1.878	0.065	1.20%
1.17	Annealed *a*-Se T$_a$=51°C 1hr	3.534	1.997	2.049	4.026	0.066	1.10%
	Relative Change (%)	7.37%	0.19%	-0.03%	114.33%	2.47%	
50	As deposited *a*-Se T$_s$=51°C	3.317	1.996	2.051	1.884	0.065	1.20%
52	Annealed *a*-Se T$_a$=51°C 1hr	3.613	2.001	2.050	3.358	0.066	1.10%
	Relative Change (%)	8.92%	0.25%	-0.08%	78.24%	1.85%	
126	As deposited *a*-Se T$_s$=51°C	3.257	1.995	2.052	1.843	0.065	1.20%
120	Annealed *a*-Se T$_a$=51°C 1hr	3.536	2.000	2.051	3.824	0.066	1.10%
	Relative Change (%)	8.57%	0.26%	-0.02%	107.48%	2.31%	
AVE	As deposited *a*-Se T$_s$=51°C	3.289	1.995	2.051	1.868	0.065	1.20%
AVE	Annealed *a*-Se T$_a$=51°C 1hr	3.561	1.999	2.050	3.736	0.066	1.10%
	Relative Change (%)	8.29%	0.23%	-0.04%	99.95%	2.21%	
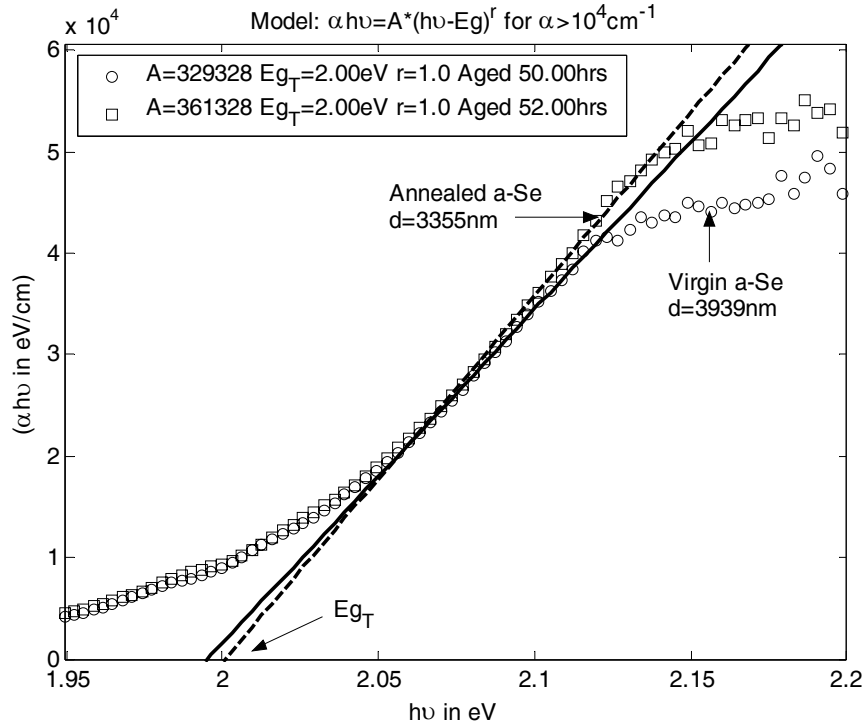
Figure 5.3: The optical bandgap Eg_T of as-deposited and annealed a-Se films.
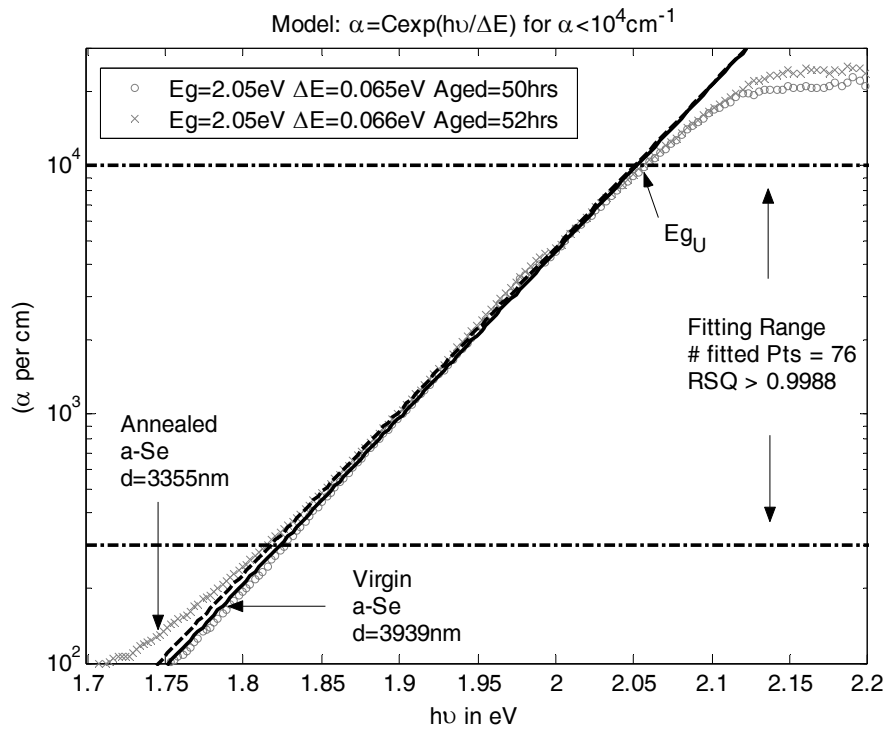
Figure 5.4: The optical bandgap Eg_U of as-deposited and annealed a-Se films.

5.2 The Thickness Dependence of the Optical Properties of Amorphous Selenium

In this part of the experiment, the transmission spectra of a-Se films of different thickness, and substrate temperature were taken regularly over a two-month period. Their optical properties at different aging times, measured after they were removed from the evaporator, were then compared so that variations with respect to thickness can be determined.

Table 5-5 records the average value of these measurements. From Table 5-5, it can be seen that Eg_T decreases as the thickness of the a-Se film, cold or hot deposited, increases. However, it should be emphasized that the determination of Eg_T for the thicker samples, average $d = 3939$nm and $d = 4764$nm, are both near the upper absorption limit of the spectrometer and thus the results obtained may involve some experimental artifacts and are probably incorrect. Figure 5.5 illustrates how the Eg_T was determined for the two cold deposited a-Se films of different thickness. From Table 5-5, one will also notice that the effect of thickness on the optical bandgap Eg_U is not as strong as on Eg_T. The maximum average deviation due to thickness in Eg_U is less than 0.7%.

Figure 5.6 illustrates how the Eg_U was determined for the two cold deposited a-Se films. Although the refractive index seems to be decreasing when the thickness increases, this is occurring at a difference in the thickness of more than 100%. This tells us that most likely, the thickness is not having a very significant effect on the refractive index.

Table 5-5: The Influence of thickness on the optical properties of a-Se films deposited at different substrate temperatures.

d (μm)	SAMPLE	Eg_T (eV)	Eg_U (eV)	ΔE (eV)	n (at λ =2000nm)	Aged (hrs)	RMSE
0.976	a-Se film T_s=51°C	2.059	2.036	0.068	2.479	0-1488	0.92%
3.939		1.995	2.050	0.068	2.442	0-126	1.20%
	Average Change	-3.15%	0.68%	0.26%	-1.46%		
2.000	a-Se film T_s=3°C	2.035	2.042	0.067	2.500	0-1416	0.80%
4.764		1.986	2.048	0.067	2.470	0-1392	1.03%
	Average Change	-2.40%	0.29%	0.28%	-1.22%		
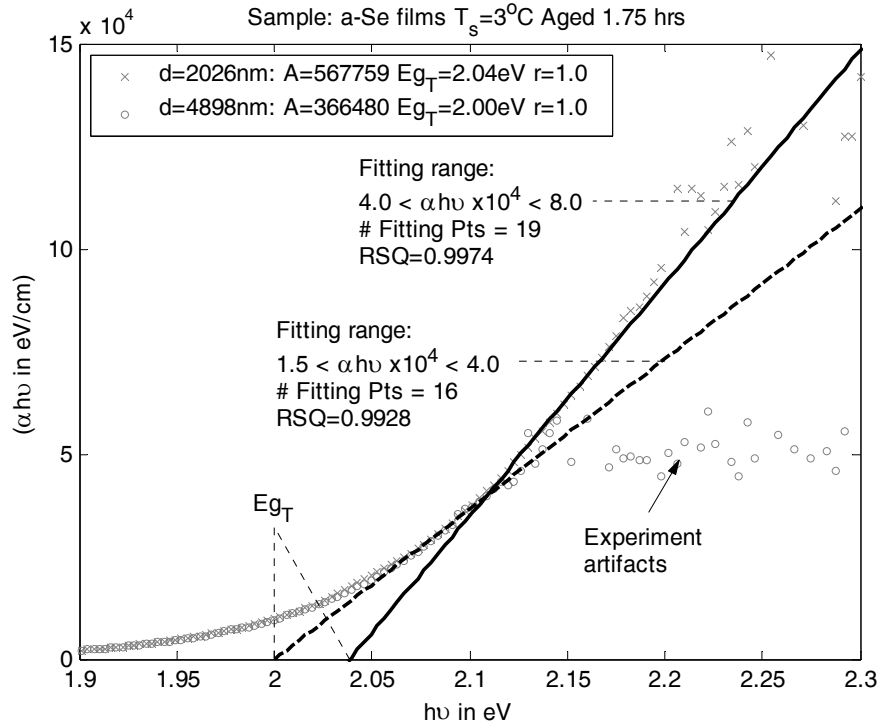
Figure 5.5: The determination of Eg_T in the $\alpha > 10^4 \text{cm}^{-1}$ region for pure *a*-Se films at $T_s = 3°C$.
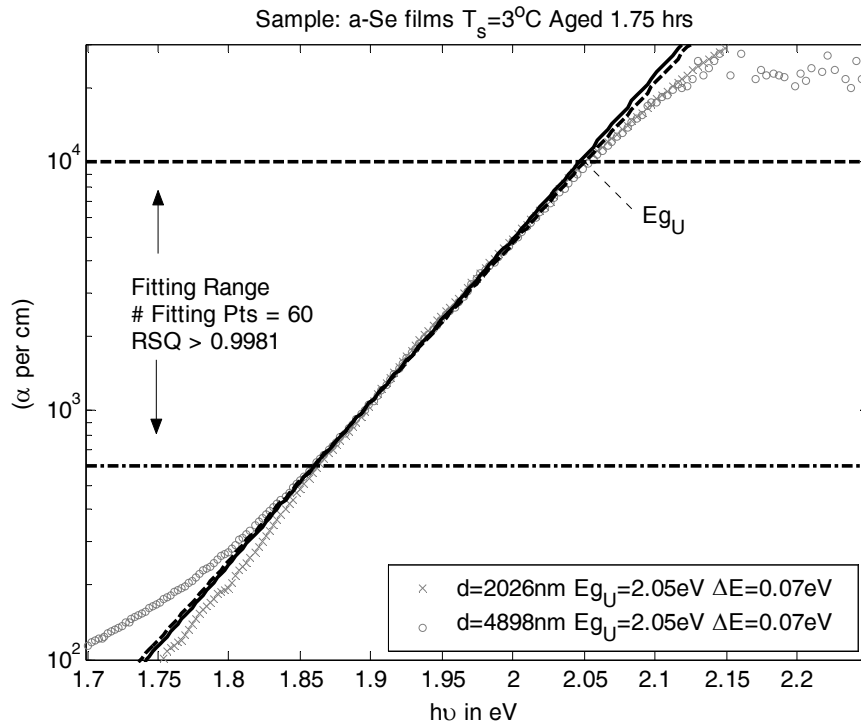
Figure 5.6: The determination of Eg_U in the $\alpha < 10^4 \text{cm}^{-1}$ region for pure *a*-Se films at $T_s = 3°C$.

Table 5-6 shows the Sellmeier coefficients of the refractive index calculated for the *a*-Se films of different deposition temperature. These are the average values of the aging films. We can see from the table that the refractive index of hot or cold deposited *a*-Se films decrease when the thickness increases. Unfortunately, equation (5.2b) cannot be used to explain the decrease in *n* with increasing thickness, as it was derived from the fundamental dependence of *n* on the concentration of polarizable atoms or molecules *N*. Although the influence of thickness on the optical properties of amorphous films and chalcogenide films have been reported by several authors, the exact nature of how the thickness influence their optical properties is still being studied [85, 86].

Table 5-6: The influence of thickness on the Sellmeier coefficients obtained for the *a*-Se films deposited at different substrate temperature.

d (μm)	SAMPLE	*n* (at λ =2000nm)	$n^2 = A + \dfrac{B\lambda^2}{\lambda^2 - C^2}$			Aging (hrs)
			A (abs)	*B* (abs)	*C* ($\times 10^{-9}$) (abs)	
0.976	*a*-Se film T$_s$=51°C	2.479	4.450	1.596	479	0-1488
3.939		2.442	4.202	1.667	466	0-126
	Average Change	-1.46%	-5.58%	4.45%	-2.73%	
2.000	*a*-Se film T$_s$=3°C	2.500	3.703	2.773	480	0-1416
4.764		2.470	4.300	1.708	462	0-1392
	Average Change	-1.22%	16.14%	-38.41%	-3.58%	

5.3 The Influence of Chlorine on Amorphous Selenium Films

Table 5-7 records the effect of chlorine on the optical properties of a-Se films deposited at T_s=3°C. It can be seen from the table that while the two optical bandgaps, Eg_T and Eg_U, remain relatively unchanged, the refractive index would decrease by an average of 0.43% and the Urbach width would decrease by an average of 2.52%. Table 5-8 shows the coefficients of the Sellmeier dispersion equation used in fitting the refractive index of the a-Se film and a-Se:67ppm-Cl film calculated from the Swanepoel technique. From the results obtained, it looks like doping 67ppm of chlorine to a-Se film has no significant effect on its optical properties. Figure 5.7 and Figure 5.8 illustrates how the optical bandgap Eg_U and optical bandgap Eg_T were determined for the pure and doped a-Se films.

Table 5-7: The influence of chlorine on the optical properties of the a-Se films deposited at T_s=3°C with Δd = 0nm.

Aged (hrs)	SAMPLE	d (μm)	Eg_T (eV)	Eg_U (eV)	ΔE (eV)	n (λ=2000nm)	RMSE
1.75	a-Se film T$_s$=3°C	2.026±0.005	2.039	2.045	0.064	2.472±0.006	0.86%
1.50	a-Se:67ppm-Cl T$_s$=3°C	2.305±0.005	2.037	2.044	0.064	2.467±0.006	0.65%
	% CHANGE		-0.06%	-0.02%	0.47%	-0.21%	
3.75	a-Se film T$_s$=3°C	2.017±0.005	2.037	2.044	0.063	2.483±0.006	0.83%
3.57	a-Se:67ppm-Cl T$_s$=3°C	2.303±0.005	2.039	2.045	0.065	2.469±0.006	0.64%
	% CHANGE		0.10%	0.04%	2.53%	-0.57%	
432.0	a-Se film T$_s$=3°C	1.972±0.005	2.034	2.035	0.068	2.523±0.006	0.77%
336.0	a-Se:67ppm-Cl T$_s$=3°C	2.251±0.005	2.028	2.033	0.065	2.530±0.006	0.99%
	% CHANGE		-0.29%	-0.08%	-4.41%	0.28%	
0-1416	a-Se film T$_s$=3°C	2.000	2.035	2.042	0.067	2.500	0.80%
0-1329	a-Se:67ppm-Cl T$_s$=3°C	2.285	2.035	2.041	0.065	2.490	0.79%
	% CHANGE		0.01%	-0.05%	-2.52%	-0.43%	
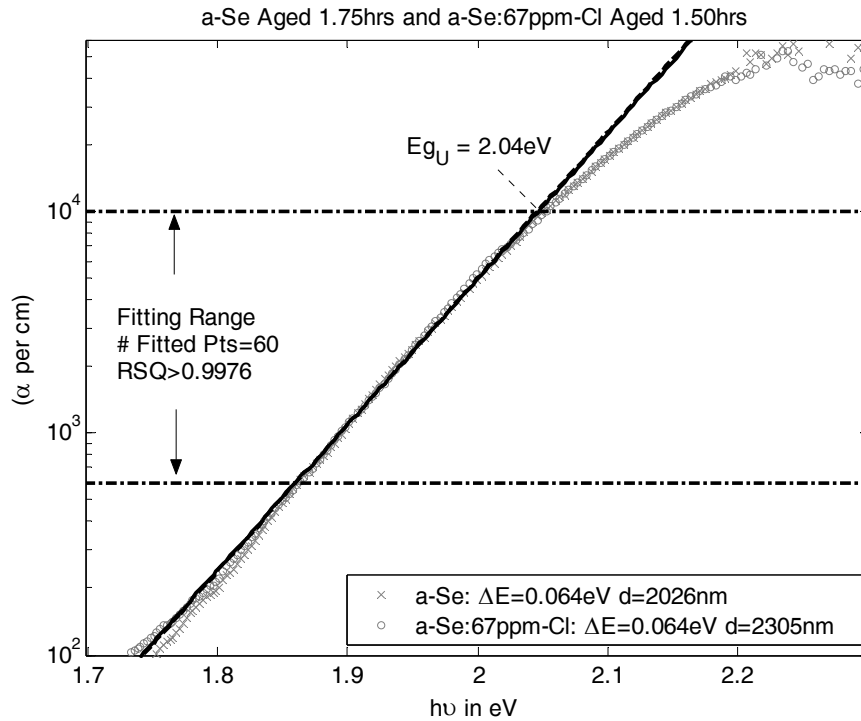
Figure 5.7: The determination of Eg_U for pure and doped a-Se films with T_s=3°C
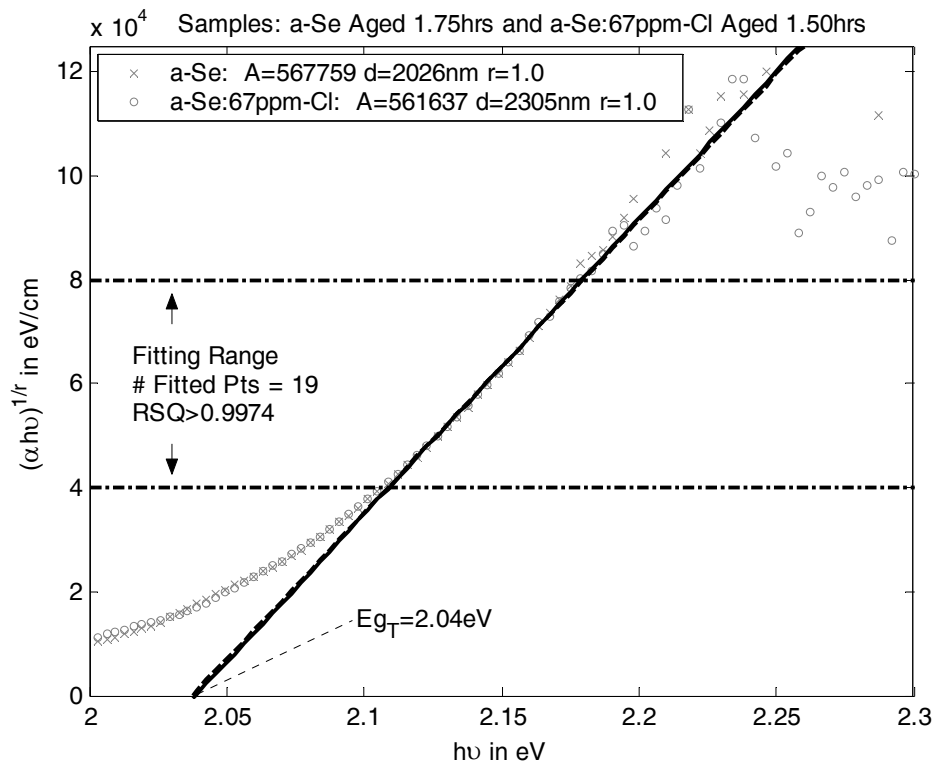
Figure 5.8: The determination of Eg_T for pure and doped a-Se films with T_s=3°C

Table 5-8: Fitting parameters of the Sellmeier Dispersion Equation used for the extrapolation of the refractive index to shorter wavelengths in *a*-Se films.

Aged (hrs)	SAMPLE	n (at λ=2000nm)	$n^2 = A + \dfrac{B\lambda^2}{\lambda^2 - C^2}$		
			A (abs)	B (abs)	C (x10^{-9}) (abs)
1.75	*a*-Se film T$_s$=3°C	2.472±0.006	4.647	1.377	483
1.50	*a*-Se:67ppm-Cl T$_s$=3°C	2.467±0.006	4.445	1.547	475
	% CHANGE	-0.21%	-4.34%	12.31%	-1.66%
3.75	*a*-Se film T$_s$=3°C	2.483±0.006	4.694	1.387	483
3.57	*a*-Se:67ppm-Cl T$_s$=3°C	2.469±0.006	4.437	1.565	474
	% CHANGE	-0.57%	-5.47%	12.79%	-1.86%
432.00	*a*-Se film T$_s$=3°C	2.523±0.006	4.784	1.489	482
336.00	*a*-Se:67ppm-Cl T$_s$=3°C	2.530±0.006	4.663	1.640	476
	% CHANGE	0.28%	-2.51%	10.14%	-1.24%
0-1416	*a*-Se film T$_s$=3°C	2.500	4.694	1.474	480
0-1329	*a*-Se:67ppm-Cl T$_s$=3°C	2.490	4.507	1.597	474
	% CHANGE	-0.43%	-3.98%	8.32%	-1.14%

5.4 The Influence of the Deposition Temperature on the Amorphous Selenium Films

From section 5.2, we saw that pure *a*-Se films, hot and cold deposited, behave in a similar fashion with thickness. Table 5-9 records the effect of substrate temperature on the optical properties of pure *a*-Se films. As can be seen in this table, all the optical properties, i.e. Eg_T, Eg_U, and *n*, remain relatively unchanged when the deposition temperature increases from T_s=3°C to 51°C. The maximum deviations due to increase in the deposition temperature, excluding the Urbach width ΔE, are less than 0.25%. Table 5-10 shows the coefficients of the Sellmeier dispersion equation obtained from fitting the equation to the refractive index of the *a*-Se films at different deposition temperatures. Figure 5.9 and Figure 5.10 illustrate how the optical bandgap Eg_U and the optical bandgap Eg_T at different deposition temperatures were determined.

Table 5-9: The influence of the deposition temperature on the optical properties of pure *a*-Se films.

Aged (hrs)	SAMPLE	*d* (µm)	Δ*d* (nm)	*Eg$_T$* (eV)	*Eg$_U$* (eV)	Δ*E* (eV)	*n* (at *λ*=2000nm)	RMSE (abs)
1.75	*a*-Se film T$_s$=3°C	4.898±0.011	0	2.002	2.051	0.068	2.426±0.006	1.10%
1.58	*a*-Se T$_s$=51°C	3.940±0.009	0	1.993	2.049	0.065	2.442±0.006	1.20%
	% CHANGE			-0.47%	-0.06%	-4.70%	0.65%	
22.00	*a*-Se film T$_s$=3°C	4.842±0.011	0	1.998	2.049	0.065	2.445±0.006	0.77%
32.00	*a*-Se T$_s$=51°C	3.938±0.009	0	1.996	2.051	0.065	2.443±0.006	1.20%
	% CHANGE			-0.10%	0.11%	-0.46%	-0.09%	
74.00	*a*-Se film T$_s$=3°C	4.736±0.011	0	1.998	2.049	0.065	2.450±0.006	0.72%
126.00	*a*-Se T$_s$=51°C	3.939±0.009	0	1.995	2.052	0.065	2.443±0.006	1.20%
	% CHANGE			-0.15%	0.13%	-0.15%	-0.27%	
0-74.0	*a*-Se film T$_s$=3°C	4.830	0	1.999	2.050	0.066	2.440	0.86%
0-126.0	*a*-Se T$_s$=51°C	3.939	0	1.995	2.051	0.065	2.443	1.20%
	% CHANGE			-0.24%	0.06%	-1.82%	0.09%	
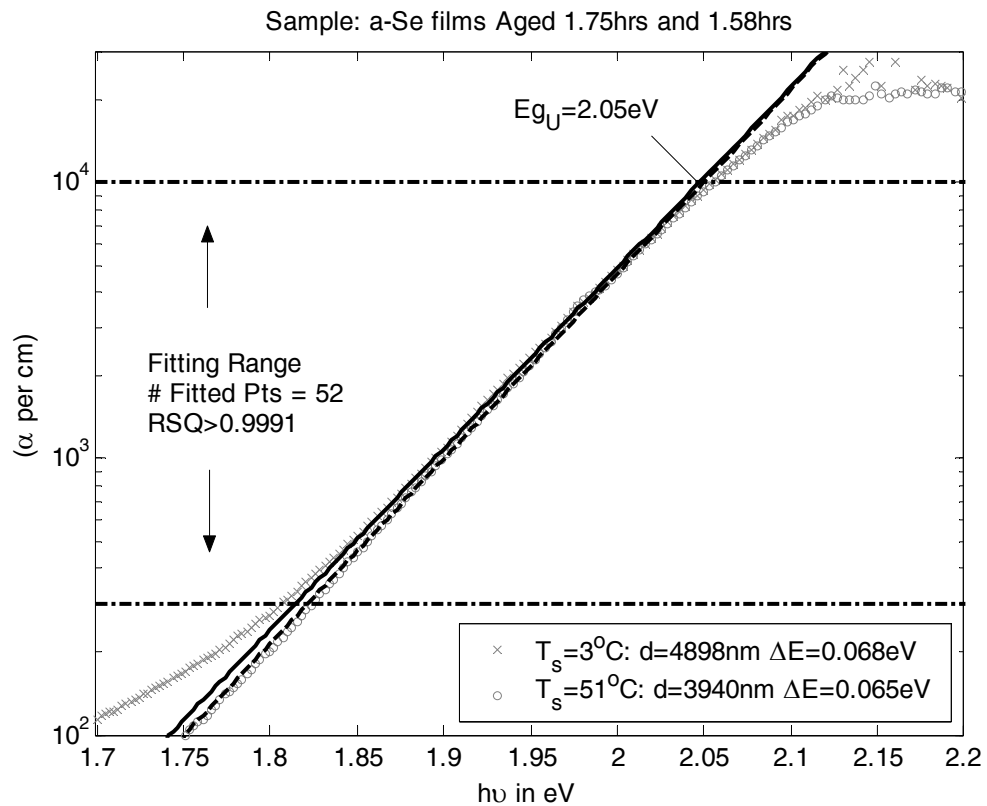
Figure 5.9: The determination of the optical bandgap *Eg$_U$* for cold and hot deposited *a*-Se films.
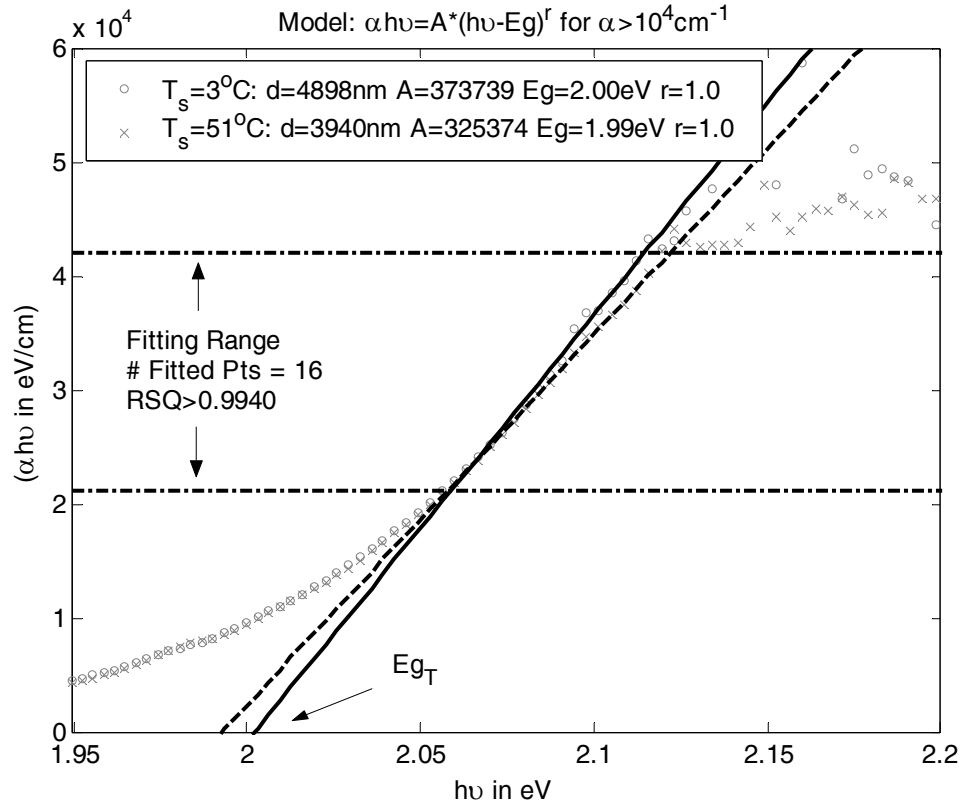
Figure 5.10: The determination of Eg_T for cold and hot deposited a-Se films.

Table 5-10: Fitting parameters of the Sellmeier Dispersion Equation used for the extrapolation of the refractive index to shorter wavelengths in a-Se films.

			$n^2 = A + \dfrac{B\lambda^2}{\lambda^2 - C^2}$		
Aged (hrs)	SAMPLE	n (at λ=2000nm)	A (abs)	B (abs)	C (x10^{-9}) (abs)
1.75	a-Se film T_s=3°C	2.426±0.006	4.237	1.560	466
1.58	a-Se T_s=51°C	2.442±0.006	4.219	1.649	467
	% CHANGE	0.65%	-0.42%	5.69%	0.21%
22.00	a-Se film T_s=3°C	2.445±0.006	4.254	1.632	465
32.00	a-Se T_s=51°C	2.443±0.006	4.223	1.651	467
	% CHANGE	-0.09%	-0.74%	1.20%	0.43%
74.00	a-Se film T_s=3°C	2.450±0.006	4.178	1.725	461
126.00	a-Se T_s=51°C	2.443±0.006	4.213	1.659	466
	% CHANGE	-0.27%	0.84%	-3.85%	1.08%
0-74.0	a-Se film T_s=3°C	2.440±0.006	4.223	1.639	464
0-126.0	a-Se T_s=51°C	2.443±0.006	4.218	1.653	467
	% CHANGE	0.09%	-0.11%	0.85%	0.57%

5.5 The Time Dependence (Aging Effect) of the Optical Properties of Amorphous Selenium

In this part of the experiment, the transmission spectrum of the *a*-Se films of different purity and substrate temperature were taken regularly over roughly a two month period. All the films were kept at room temperature at about 20°C and stored in a Petri dish wrapped in aluminum foil. This ensures that the film receives no external stimulation and is in complete darkness in between measurements. Their optical properties at different aging times were then extracted and checked for variations with respect to time. Table 5-11 and Table 5-12 show the optical properties of a number of aging *a*-Se and *a*-Se:67ppm-Cl films deposited at different substrate temperatures. In general, the thickness would shrink with time and the refractive index would increase with time for a cold deposited pure or doped *a*-Se film. The two optical bandgaps would also decrease slightly.

Table 5-11: Optical properties of aging *a*-Se and *a*-Se:67ppm-Cl films.

Aged (hrs)	SAMPLE	*d* (um)	Δ*d* (nm)	Eg_T (eV)	Eg_U (eV)	*n* (at λ=2000nm)	RMSE (abs)
1.75	*a*-Se film T_s=3°C	2.026±0.005	0	2.039	2.045	2.472±0.006	0.86%
19.75		2.019±0.005	0	2.040	2.046	2.480±0.006	0.61%
432		1.972±0.005	0	2.034	2.035	2.523±0.006	0.77%
	% CHANGE	-2.68%		-0.23%	-0.48%	2.06%	
1.50	*a*-Se:67ppm-Cl T_s=3°C	2.305±0.005	0	2.037	2.044	2.467±0.006	0.65%
3.57		2.303±0.005	0	2.039	2.045	2.469±0.006	0.64%
336		2.251±0.005	0	2.028	2.033	2.530±0.006	0.99%
1320		2.224±0.005	0	2.028	2.031	2.558±0.006	1.40%
	% CHANGE	-3.55%		-0.47%	-0.64%	3.69%	
1.08	*a*-Se T_s=51°C	3.940±0.009	0	1.994	2.048	2.441±0.006	1.20%
4.58		3.939±0.009	0	1.993	2.049	2.442±0.006	1.20%
32.00		3.938±0.009	0	1.996	2.050	2.443±0.006	1.20%
126		3.939±0.009	0	1.994	2.051	2.443±0.006	1.20%
	% CHANGE	-0.04%		0.03%	0.11%	0.08%	
1.17	*a*-Se T_a=51°C 1hr	3.349±0.008	0	1.997	2.051	2.456±0.006	1.10%
33.00		3.344±0.008	0	1.999	2.051	2.459±0.006	1.10%
120		3.356±0.008	0	1.999	2.053	2.452±0.006	1.10%
576		3.362±0.008	0	1.999	2.050	2.454±0.006	0.94%
	% CHANGE	0.53%		0.03%	-0.06%	-0.19%	

Table 5-12: Fitting parameters of the Sellmeier Equation of aging *a*-Se and *a*-Se:67ppm-Cl films.

				$$n^2 = A + \frac{B\lambda^2}{\lambda^2 - C^2}$$		
Aged (hrs)	SAMPLE	*d* (um)	n (at L)	A (abs)	B (abs)	$(C \times 10^{-9})$ (abs)
1.75	*a*-Se film T_s=3°C	2.026	2.472	4.647	1.377	483
19.75		2.019	2.480	4.572	1.491	477
432.00		1.972	2.523	4.784	1.489	482
	% CHANGE	-2.68%	2.06%	2.94%	8.10%	-0.21%
1.50	*a*-Se:67ppm-Cl T_s=3°C	2.305	2.467	4.445	1.547	475
3.57		2.303	2.469	4.437	1.565	474
336.00		2.251	2.530	4.663	1.640	476
1320.00		2.224	2.558	4.750	1.693	475
	% CHANGE	-3.45%	3.60%	7.05%	8.20%	0.21%
1.08	*a*-Se T_s=51°C	3.940	2.441	4.184	1.678	465
4.58		3.939	2.442	4.205	1.664	466
32.00		3.938	2.443	4.223	1.651	467
126.00		3.939	2.443	4.213	1.659	466
	% CHANGE	-0.01%	0.02%	0.18%	-0.31%	0.00%
1.17	*a*-Se T_a=51°C 1hr	3.349	2.456	4.301	1.636	469
33.00		3.344	2.459	4.293	1.656	469
120		3.356	2.452	4.310	1.606	471
576		3.362	2.454	4.277	1.651	467
	% CHANGE	0.53%	-0.19%	-0.38%	-0.32%	-0.43%

From Table 5-12, it can be seen that there are only noticeable changes in the thickness for cold-deposited films. When the film is annealed or deposited at a higher substrate temperature, there is very little change, less than 0.5%, in the thickness during aging. As it was discussed in section 5.1, most of the incompatible molecular clusters in the hot-deposited or the annealed films were most likely polymerized or cross-linked into the amorphous network. There is thus not much more reduction in the free volume when they are left to anneal at a room temperature of 20°C. Figure 5.11 shows the difference in the amount of changes found in the thickness of an aging *a*-Se and *a*-Se:67ppm-Cl film deposited at different substrate temperatures. Besides the thickness, Table 5-12 also shows a noticeable increase in the refractive index in those films that were deposited at T_s=3°C. Films that are either annealed or deposited at T_s=51°C would only show a small increase in their refractive index.
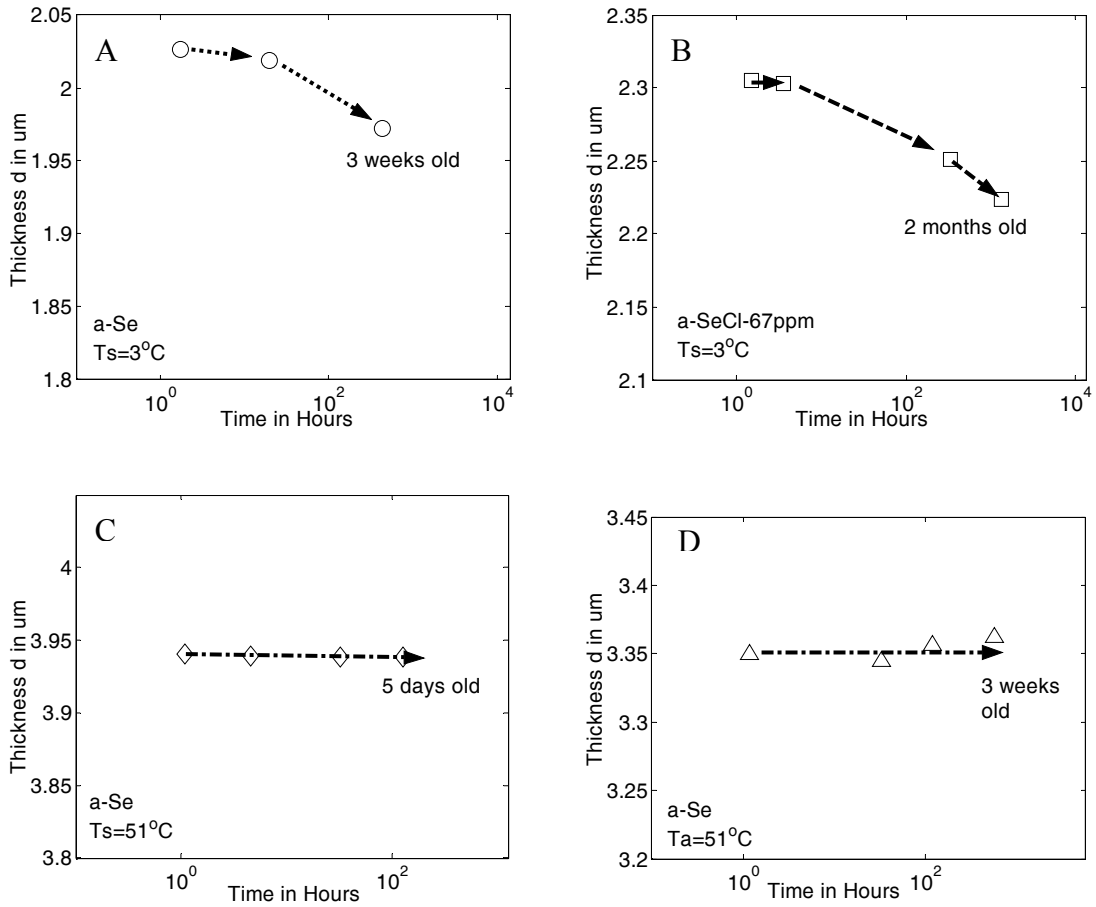
Figure 5.11: The time dependence of the thickness for *a*-Se and *a*-Se:67ppm-Cl films of different substrate temperature, purity level, and heat treatment. (A) *a*-Se film T_s=3°C, (B) *a*-Se:67ppm-Cl film T_s=3°C, (C) *a*-Se film T_s=51°C, and (D) annealed *a*-Se film T_a=51°C.

Unlike an annealed film, the increase in the refractive index with aging is across the entire spectral region from λ =500 to 2000nm and is probably due to the densification of the film alone and not the rearrangement of the bonds in the material. This can be seen from Equation (5.2b) above where a change of $\Delta d/d$ = -3.55% predicts a $(\Delta n/n)_{cal}$ = 3.52%, which is very close to the value we have obtained. Figure 5.12 shows how the refractive index of different aging *a*-Se and *a*-Se:67ppm-Cl films change with time and Figure 5.13 shows the wavelength dispersion of the refractive index of a cold deposited *a*-Se film.

Figure 5.12: The refractive index of aging *a*-Se and *a*-Se:67ppm-Cl films, deposited at a substrate temperature of T_s=3°C and T_s=51°C, and annealed at T_a=51°C for an hour.

Figure 5.13: The dispersion of the refractive index of aging *a*-Se films (d_{ave}=2000nm).

Table 5-13: Fitting parameters from models used for the determination of the optical bandgaps in aging *a*-Se films.

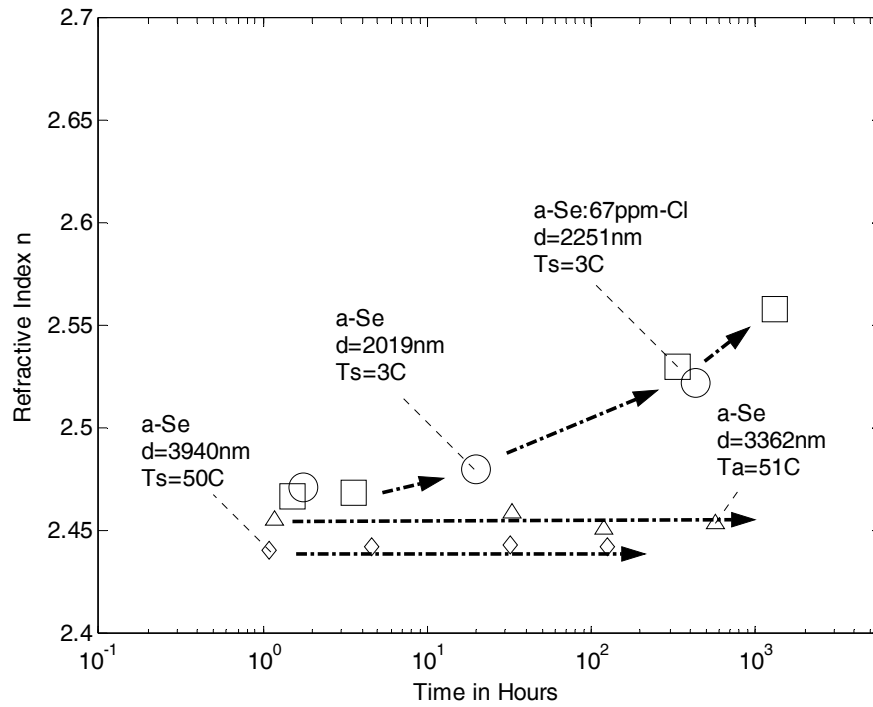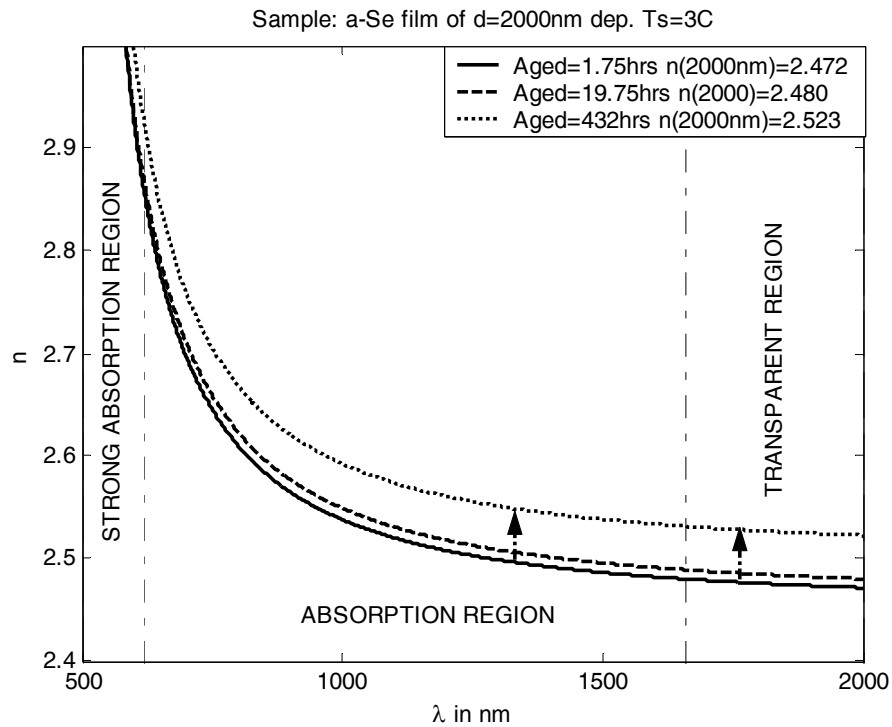| Aged (hrs)	SAMPLE	$\alpha h\upsilon = A(h\upsilon - Eg_T)$ ($\alpha \geq 10^4\,\text{cm}^{-1}$)		$\alpha = C\exp(h\upsilon/\Delta E)$ ($\alpha < 10^4\,\text{cm}^{-1}$)			RMSE (%)
		A (x10^5) (eV/cm)	Eg_T (eV)	Eg_U (eV)	C (x10^{-12}) (cm^-1)	ΔE (meV)	
1.75	*a*-Se film T$_s$=3°C	5.68	2.039	2.045	143	64.1	0.86%
19.75	*d*=1.8-2.0μm	5.79	2.040	2.046	110	63.6	0.61%
432		5.71	2.034	2.035	1022	68.0	0.77%
	% CHANGE	0.63%	-0.23%	-0.48%	614.58%	6.08%	
1.50	*a*-Se:67ppm-Cl T$_s$=3°C	5.62	2.037	2.044	1.67	0.064	0.65%
3.57	*d*=2.2-2.3μm	5.70	2.039	2.045	2.11	0.065	0.64%
336		5.52	2.028	2.033	2.67	0.065	0.99%
1320		5.54	2.028	2.031	2.40	0.065	1.40%
	% CHANGE	-1.42%	-0.47%	-0.64%	43.71%	0.62%	
1.08	*a*-Se T$_s$=51°C	3.29	1.994	2.048	130	0.065	1.20%
4.58	*d*=3.9μm	3.23	1.993	2.049	126	0.064	1.20%
32.00		3.32	1.996	2.050	126	0.065	1.20%
126		3.24	1.994	2.051	133	0.065	1.20%
	% CHANGE	-1.52%	0.03%	0.11%	2.31%	0.15%	
1.17	*a*-Se T$_a$=51°C 1hr	352	1.997	2.051	742	0.066	1.10%
33.00	*d*=3.3μm	353	1.999	2.051	463	0.067	1.10%
120		352	1.999	2.053	711	0.066	1.10%
576		363	1.999	2.050	437	0.067	0.94%
	% CHANGE	3.13%	0.13%	-0.05%	-41.11%	0.30%	

In contrast to the refractive index and the thickness, the changes in the two optical bandgaps, Eg_T and Eg_U for the two cold deposited pure and doped *a*-Se films are quiet small. This can be seen in Table 5-13, where the parameters used for the determination of the two optical bandgaps can be found. Nevertheless, the downward trend was noticeable in the plots used to obtain the two optical bandgap energies. This agrees with the *Hervé-Vandamme* relationship, equation (2.20), which says that when the optical bandgap energy decreases, its refractive index increases. Figure 5.15 to Figure 5.17 shows the decrease in the optical bandgap energy obtained at $\alpha = 10^4$ cm^{-1} from the Urbach edge and at $\alpha h\upsilon = 0$ cm^{-1} in the Tauc plot with $r = 1$.
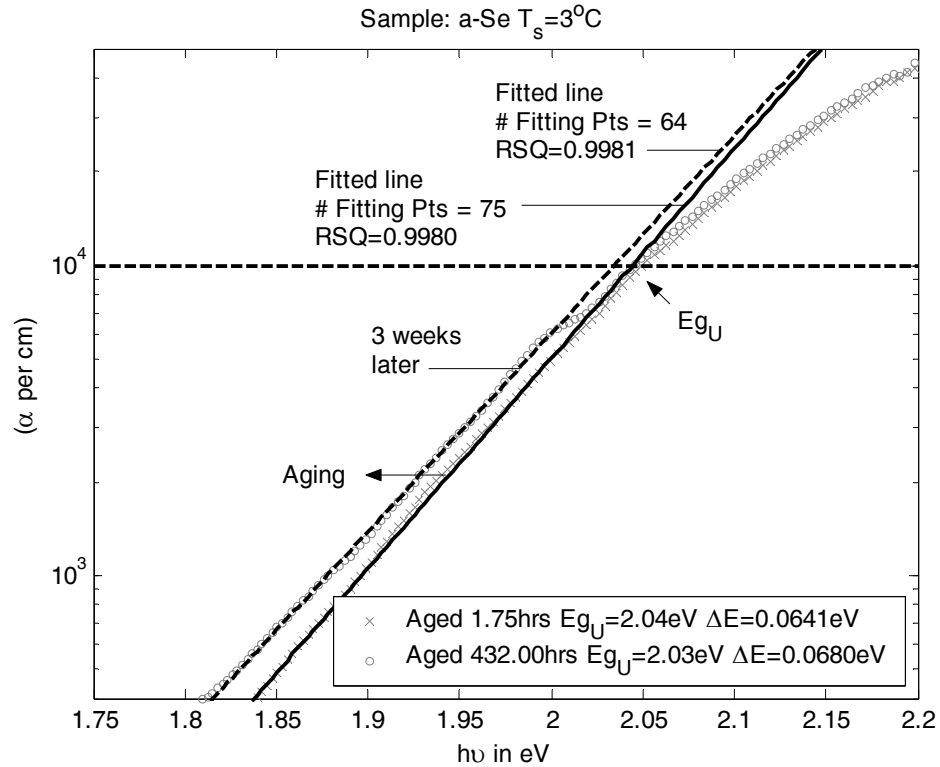
Figure 5.14: The determination of Eg_U for an aging 2.026μm a-Se film.
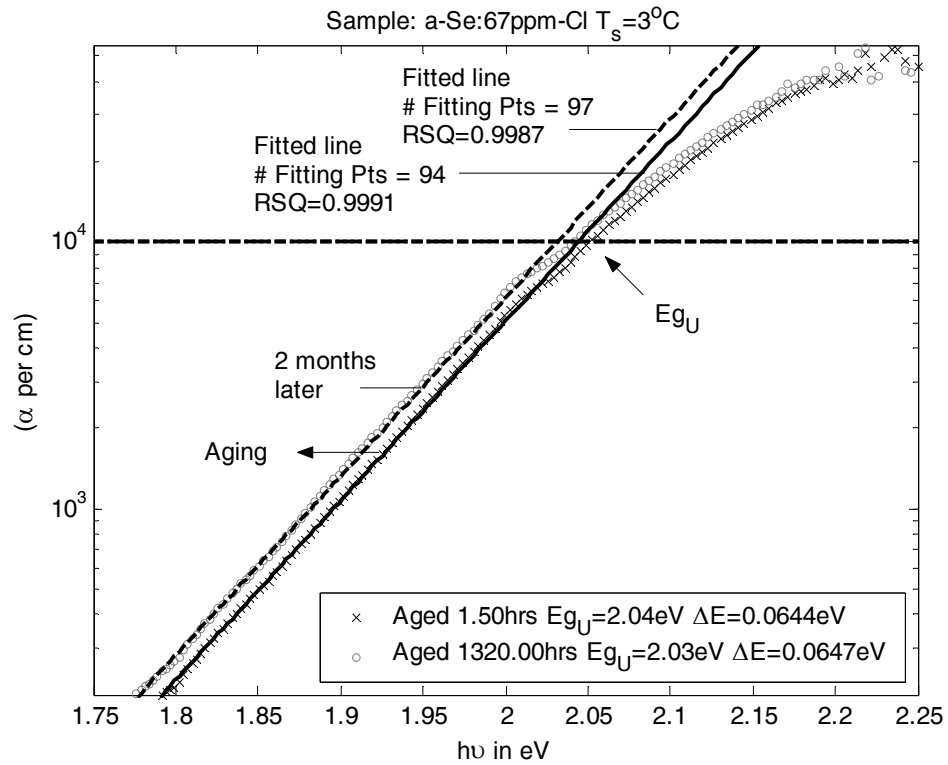
Figure 5.15: The determination of Eg_U for an aging 2.305μm a-Se:67ppm-Cl film.
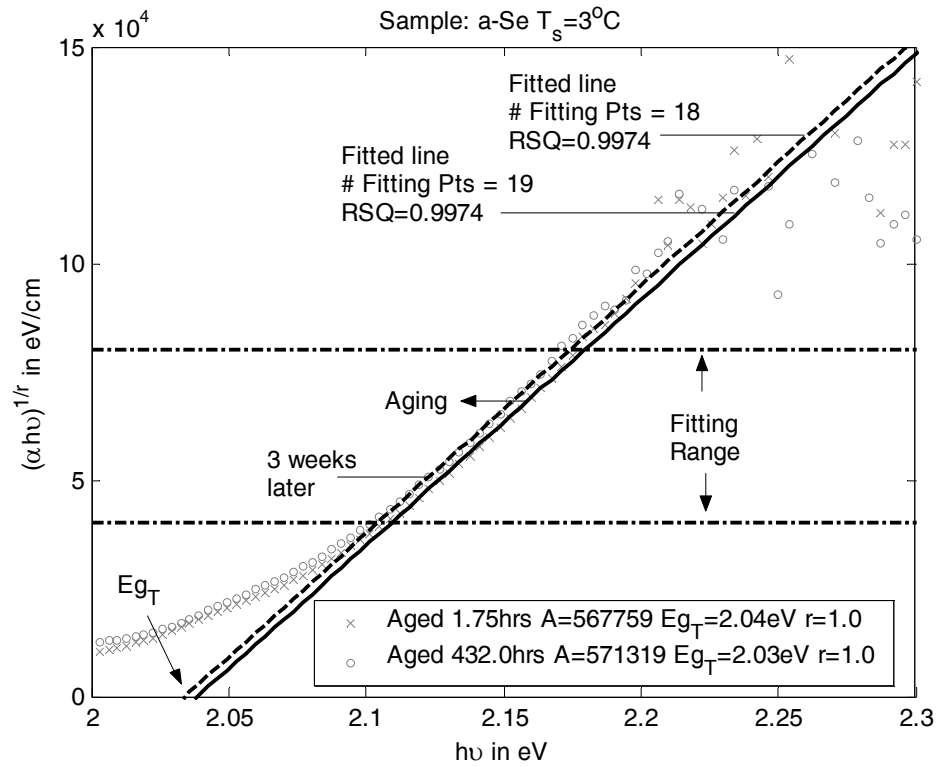
Figure 5.16: The determination of Eg_T for an aging 2.026μm a-Se film.
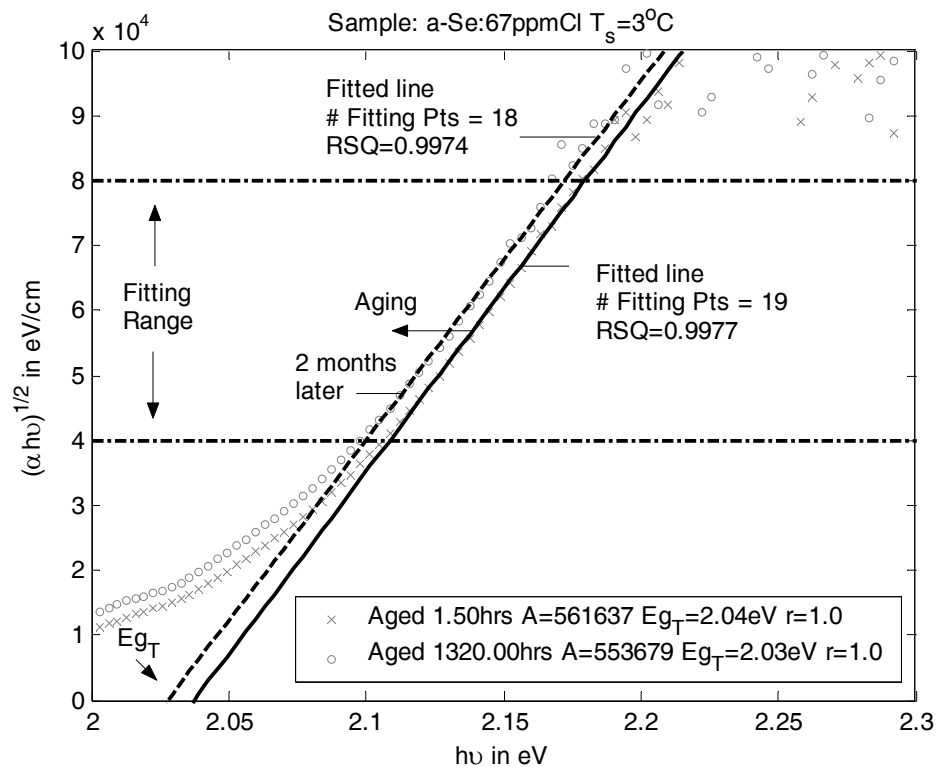
Figure 5.17: The determination of Eg_T for an aging 2.305μm a-Se:67ppm-Cl film.
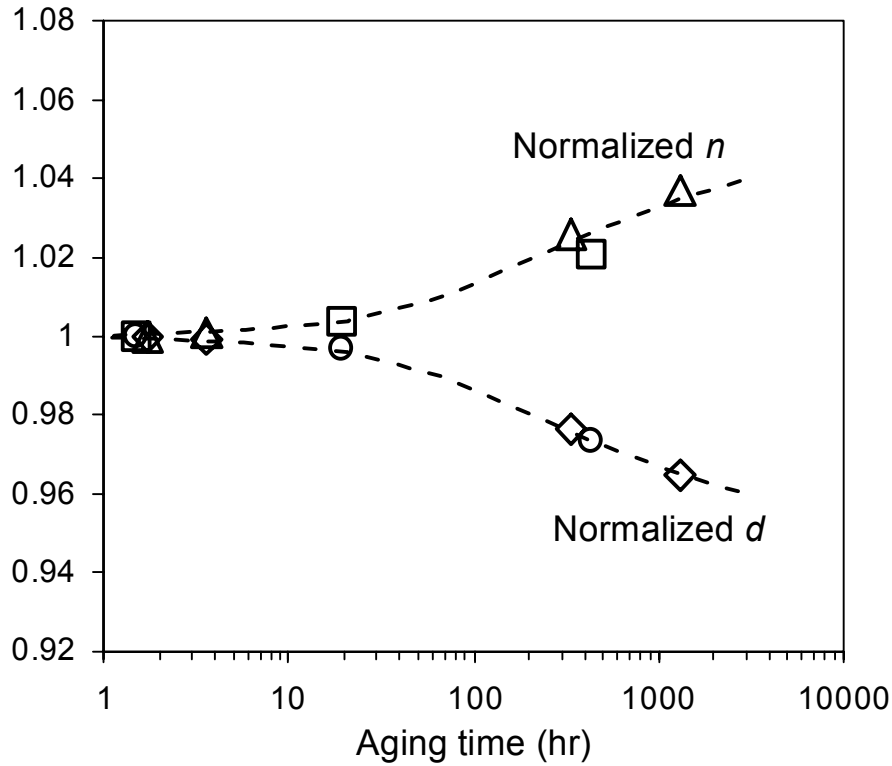
Figure 5.18: The increase of the refractive index due to densification.

Figure 5.18 shows the normalized refractive index and normalized thickness against the aging time, where the normalization was done with respect to n and d at the first measurement at 1.5 hr and 1.75 hr for undoped and Cl-doped films. The dashed curves in Figure 5.18 are to guides the eye. Their similar but opposite trends suggest that the changes in n may be due to changes in the thickness, *i.e.* densification or increase in the atomic concentration N_{at}. We can write the Clasius-Mossotti equation as $(n^2 - 1)(n^2 + 2)$ $= (1/3\varepsilon_o)\alpha N_{at} \approx C/d$ where α is the mean polarizability per atom, and C is a constant. Taking $n = 2.467$, $d = 2.305$ mm after 1.75 hr of aging, we can find C. Then, when $d = 2.224\mu$m after 1320 hr of aging, we should expect $n = 2.573$, which is very close to the measured value 2.558 in Table 5-11. Given the experimental errors we believe that changes in n can be accounted largely by changes in the density ρ, and changes in the average polarizability per atom may be of secondary importance.

6. Conclusions

Recently there has been a substantial renewed interest in the electrical and optical properties of amorphous selenium (*a*-Se) films due to its use as an x-ray photoconductor in newly developed x-ray image detectors and its use as a photoconductor in the ultra-sensitive HARP video tubes, which can even capture images under starlight, 5×10^{-6} lux. This project has examined the optical properties of a range of *a*-Se films fabricated by conventional vacuum deposition technique.

Materials deposited as thin films usually exhibit some degree of interfacial stress arising in part from the differences in the thermal expansion coefficients or lattice mismatches between the film and the substrate material. This interfacial stress is distinguishable from the inherent stress in a thin film that varies with crystallite grain size, phase homogeneity, and the presence of impurities. The magnitude of such stresses can be influenced by changing the film deposition parameters or through physical or chemical interaction of the film with the environment. Since both the real and imaginary parts of the refractive index change with the stress levels, large stresses may cause the optical performance to deviate from the design parameters. Knowledge of how the complex refractive index changes with the degree of stress and the stress homogeneity is thus necessary for us to understand the optical response, coating-substrate adherence, and stability during usage.

The transmission spectra, T(λ) were analyzed using the Swanepoel technique, which allowed the thickness, refractive index, and the absorption coefficient to be extracted. It was found that the refractive index is best fitted to the Sellmeier dispersion equation. For example, an *a*-Se film of 2.026μm thick deposited at 3°C for 1.75hrs, the Sellmeier equation was found to be,

$$n^2 = 4.647 + \frac{1.377\lambda^2}{\lambda^2 - (483)^2} \text{ ,} \qquad\qquad 6.1$$

where λ is in nm. Higher terms were found to be unnecessary. The Sellmeier coefficients for the rest of the *a*-Se films investigated in this work are given in

Table 5-3, Table 5-6, Table 5-8, Table 5-10 and Table 5-12.

In this project, it was found that an annealed a-Se film will have a higher refractive index and optical bandgap Eg_T than an as-evaporated a-Se film. Its thickness would decrease and the film would become more compact. The increase in the refractive index is across the entire spectral region from λ =500 to 2000nm and it is not caused by densification alone. This can be seen from the equation below:

$$\frac{\Delta n}{n} = \frac{-(n^2-1)(n^2+2)}{6n^2}\frac{\Delta d}{d}$$
6.2

A change of $\Delta d/d$ = -14.88% leads to a $(\Delta n/n)_{cal}$ = 16.43%. This is much higher than what was obtained from the experiment, which is $(\Delta n/n)_{exp}$ = 0.45%. The reason is that the change in n also involves changes in bonding and hence in the polarizability per atom.

The refractive index was also fitted to the Wemple-DiDominico dispersion relationship to show that when the thickness decreases, the dispersion energy E_d increases. The annealed films have been found to have a broader absorption edge and their absorption around the Urbach tail region has been observed to increase with annealing. This is in agreement with the results obtained by the Time-of-Flight transient photocurrent measurement.

Although the influence of the thickness of the film, the temperature of the glass substrate, and the doping of 67ppm of chlorine on the optical properties of the a-Se film was found to be negligible, there are noticeable changes in aging.

 In the determination of the time dependence of the optical properties of a-Se films, it was found that as the cold deposited pure a-Se films age, the refractive index would increase, the thickness would decrease, and the two optical bandgaps of the pure a-Se films, Eg_T and Eg_U, would decrease slightly. Similar time dependence trends in the

thickness, refractive index, and absorption in the Urbach tail region were also noted when 67ppm of chlorine was added to amorphous selenium. The increase in the refractive index is across the entire spectral region from λ =500 to 2000nm and it is found to be caused by densification alone. This can be seen from Equation (6.1) above where a change of $\Delta d/d$ = -3.55% predicts a $(\Delta n/n)_{cal}$ = 3.52% which is very close to the value we have obtained. Unlike a cold deposited film, hot deposited and annealed a-Se films has very little changes in their thickness and its optical properties during aging.

Table 6-1: Summary of the results obtained on the Optical properties of a-Se films.

Effect	d (um)	Eg_T (eV)	Eg_U (eV)	n (at λ=2000nm)
Annealing	Decreased ▼	-	-	Increased ▲
Increased Thickness	N.A.	-	-	-
Doped 67ppm of Cl	N.A.	-	-	-
Deposition Temperature	N.A.	-	-	-
Aging (Hot deposited)	-	-	-	-
Aging (Cold deposited)	Decreased ▼	Decreased ▼	Decreased ▼	Increased ▲

Note: N.A. means parameter not applicable to the effect under investigation and the dash line '-' means no significant changes has occurred.

In using the Swanepoel technique to extract the optical properties of thin films from the transmission spectrum, it was realized that the technique would only give a reasonably acceptable results, RMSE < 2%, for thin films that are under 7.0-8.0μm thick. Any films that are roughly thicker than this thickness would experience noticeable error in their optical properties. In our opinion, the ideal thickness for applying the Swanepoel technique is around 0.8 to 5.0μm.

7. References

[1]   Joseph H. Simmons and Kelly S. Potter, "Optical Materials", Academic Press, San Diego, CA (USA), xiii-xv, 2000.

[2]   Ralf M., "Photonics – Linear and Nonlinear Interaction of Laser Light and Matter", Springer-Verlag Berlin Heidelberg, 1-9, 2001.

[3]   Gregory J. E., "Characterisation of Optical Materials", Butterworth-Heinemann, Stoneham, MA(USA), 1-5, 1993.

[4]   Zhao W., Hunt D.C., Kenkichi T., Rowlands J.A., " Amorphous selenium flat panel detectors for medical applications", *Nuclear Instruments & Methods in Physics Research A*, **549**, 205-209, 2005.

[5]   Kasap S.O, Rowlands J.A., "Review x-ray photoconductors and stabilized *a*-Se for direct conversion digital-at-panel x-ray image detectors", *Journal of Materials Science: Materials in Electronics*, **11**, 179-198, 2000.

[6]   Kubota M., Kato T., Suzuki S., Maruyama H., Shidara K., Tanioka K., Sameshima K., Makishima T., Tsuji K., Hirai T. and Yoshida T., "Ultrahigh-sensitivity New Super-HARP camera", *IEEE Transaction on broadcasting*, **42**, 3, 1996.

[7]   Kasap S.O., Harry R., and Yann B., "Cambridge Concise Encyclopedia   of Optoelectronics and Photonics", to be published in 2007.

[8]   Kasap S.O., "Photoreceptors: The Chalcogenides, Handbook of Imaging Materials Second Edition Revised and Expanded edited by Arthur S. Diamond and David S. Weiss", Marcel Dekker Inc., New York, 329-369, 2002.

[9]   Toshisha W., Masahide G., Hiroshi O., Hirotaka M., Masahide A., Kenkichi T., and Norifumi E., " New Signal Readout Method for Ultrahigh-Sensitivity CMOS Image Sensor", IEEE transactions on electron devices, **50**, 63-69, 2003.

[10] Madan A. and Shaw M.P., "The Physics and Applications of Amorphous Semiconductors", Academic Press Inc., San Diego, 4-10, 471-476, 1988.

[11] Mott N.F., "Electrons in disordered structures", *Advances in Physics*, **16**, 49-57, 1967.

[12] Cohen M.H., Fritzsche H. and Ovshinski S.R., "Simple band model for amorphous semiconductor alloys", *Physical Review Letters*, **22**, 1065-1072, 1969.

[13] Marshall J.M. and Owen A.E., "Drift mobility studies in vitreous arsenic triselenide", *Philosophical Magazine*, **24**, 1281-1290, 1971.

[14] Tauc J., "Amorphous and Liquid Semiconductor", Plenum Press, London and New York, 177-178, 1974.

[15] Tauc J., "Amorphous and Liquid Semiconductor", Plenum Press, London and New York, 171-178, 1974.

[16] Singh J., Shimakawa K, " Advances in Amorphous Semiconductors", Taylor & Francis, London and New York, 57-96, 2003.

[17] O'Leary S. K., "Relationship between the optical gap and the absorption   tail breath in amorphous GaAs", *Journal of Applied Physics*, **96**, 12, 7052-   7059,   2004.

[18] O'Leary S. K., "The relationship between the distribution of   electronic states and the optical absorption spectrum of an amorphous semiconductor: An empirical analysis", *Journal of Applied Physics*, **82**, 7, 3334-3340, 1997

[19] Tauc J., "Amorphous and Liquid Semiconductor", Plenum Press, London and New York, 178-188, 1974.

[20] Tauc J., "Amorphous and Liquid Semiconductor", Plenum Press, London and New York, 188-192, 1974.

[21] Tan W.C., Koughia K., Singh Jai, and Kasap S.O, "Fundamental properties of Optical Properties I", Wiley, in print, Chapter 1, 2006.

[22] Wemple S.H. and DiDomenico M., "Behavior of the Electronic Dielectric Constant in Covalent and Ionic Materials", *Physical Review B*, **3**, 1338, 1971.

[23] Hervé P. J. L. and Vandamme L. K. J., *Journal of Applied Physics*, **77**, 5476 (1996).

[24] Tauc J., "Amorphous and Liquid Semiconductor", Plenum Press, London and New York, 195-218, 1974.

[25] Lucovsky G., "Physics of Selenium and Tellurium edited by E. Gerlach and P. Grosse", Springer-Verlag, New York, 1979.

[26] Lucovsky G. and Galeener F.L., "Intermediate range order in amorphous solids", *Journal of Non-Crystalline Solids*, **35-36**, 1209-1214, 1980.

[27] Meek P.E., "Structural interpretations of the vibrational spectra of models of amorphous As and SE", Processing of the symposium on the Structure of Non-Crystalline Solids, edited by Gaskell P.H., Taylor & Francis Ltd., London, 235-237, 1977.

[28] Robertson J., "Electronic structure of amorphous semiconductor", *Advances in Physics*, **32**, 361-452, 1983.

[29] Kastner M., Adler D. and Fritzsche H., "Valence-alternation Model for Localized Gap States in lone-pair semiconductors", *Physical Review Letters*, **37**, 1504-1507, 1976.

[30] Adler D., "Amorphous-semiconductors", *Scientific American*, **236**, 36-48, 1977.

[31] Kastner M., "Amorphous and liquid semiconductors", Seventh International Conference on Amorphous and Liquid Semiconductors, edited by Spear W.E., University of Edinburgh, 504, 1977.

[32] Abkowitz M., "Changes in photoelectric properties of glassy chalcogenides induced by chemical doping, irradiation, and thermal history", *Journal of Chemical Physics*, **46**, 4537, 1967.

[33] Agarwal S.C., "Nature of localized states in amorphous semiconductors – a study by electron spin resonance", *Physical Review B*, **7**, 685-691, 1973.

[34] Mott N.F. and Davis E.A., "Electronic Processes in Non-Crystalline Solids", Clarendon Press, Oxford, 1979.

[35] Elliot S.R., "Physics of Amorphous Materials, Longman", New York, 1984.

[36] Elliot S.R., "A unified model for reversible photo-structural effects in chalcogenide glasses", *Journal of Non-Crystalline Solids*, **81**, 71-98, 1986.

[37] Charles D., Lefrancois G. and Larmagnac J.P., "A model for steady-state photoconductivity in amorphous selenium", *Journal of Physics Letters*, **45**, L901-L906, 1984.

[38] Abkowitz M., "Density of states in *a*-Se from combined analysis of xerographic potentials and transient transport data". *Philosophical Magazine Letters*, **58**, 53-57, 1988.

[39] Abkowitz M., "Evidence of the defect origin of states which control photoelectric behavior of amorphous chalcogenides", *Journal of Non-Crystalline Solids*, **66**, 315-320, 1984.

[40] Abkowitz M., "Relaxation induced charges in electrical behavior of glassy chalcogenide semiconductors", *Polymer Engineering Science*, **24**, 1149-1154, 1984.

[41] Kasap S.O. and Juhasz C., "Time-of-flight drift mobility measurements on chlorine-doped amorphous selenium films", *Journal of Physics D: Applied Physics*, **18**, 703-720, 1985.

[42] Veres J. and Juhasz C., "Cycled xerographic and time-of-flight measurements: theory and experiment", *Journal of Non-Crystalline Solids*, **164-166**, 407-410, 1993.

[43] Orlowski T.E. and Abkowitz M., "Microstripline transient photocurrents in *a*-Se structure resolved in shallow band tail states", *Solid State Communications*, **59**, 665-668, 1986.

[44] Abkowitz M. and Markovics J.M., "Evidence of equilibriumnative defect population in amorphous chalcogenides from analysis of xerographic spectra", *Philosophical Magazine B*, **49**, L31-L36, 1984.

[45] Spear W.E., "Transit Time Measurements of Charge Carriers in Amorphous Selenium Films", Proceedings of Physical Society of London, **B70**, 669, 1957.

[46] Spear W.E., "The Hole mobility in Selenium", Proceedings of Physical Society of London, **B76**, 826, 1960.

[47] Hartke J.L., "Drift mobilities of Electrons and Holes and Space-Charged-Limited Currents in Amorphous Selenium Films", *Physical Review*, **125**, 1177-1192, 1962.

[48] Song H.Z., Adriaenssens G.J., Emelianova E.V., Arkhipov V.I., „Distribution of gap states in amorphous selenium thin films", *Physical Review B*, **59**, 10607-10613, 1999.

[49] Kasap S.O. and Rowlands J. A., "x-ray photoconductors and stabilized a-Se for direct conversion digital flat-panel x-ray image-detectors", *Journal of Material Science: Material in Electronics*, **11**, 179-198, 2000.

[50] Benkhedir L., Aida M.S., and Adriaenssens G.J., "Defect levels in the band gap of amorphous selenium", *Journal of Non-Crystalline Solids*, **344,** 193-198, 2004.

[51] Benkhedir L., Brinza M. and Adriaenssens G. J., "Electronic density of states in amorphous selenium", *Journal of Physic: Condensed Matter*, **16**, S5253-64**,** 2004.

[52] Qamhieh N., Benkhedir M.L., Brinza M., Willekens J. and Adriaenssens G.J., " Steady-state photoconductivity in amorphous selenium glasses", *Journal of Physics: Condensed Matter*, **16,** 3827-3833, 2004.

[53] Koughia K., Shakoor Z., Kasap S.O. and Marshall J.M., "Density of localized electronic states in *a*-Se from electron time-of-flight photocurrent measurements", *Journal of Applied Physics*, **97**, 33706-11, 2005.

[54] Abkowitz M. and Enck R., "Xerographic spectroscopy of gap states in amorphous semiconductors ", *Physical Review. B*, **25**, 2567, 1982.

[55] Veres J. and Juhasz C., "Cycled xerographic and time-of-flight measurements: theory and experiment", *Journal of Non-Crystalline Solids*, **164-166,** 407-410, 1993.

[56] Nesdoly M.T.A., "x-ray Sensitivity and x-ray induced charge transport changes in stabilized *a*-Se Films", Electronic Thesis: University of Saskatchewan, Library, Canada, 29, 2000.

[57] Kasap S.O., "Photoreceptors: The Chalcogenides, Handbook of Imaging Materials Second Edition Revised and Expanded edited by Arthur S. Diamond and David S. Weiss", Marcel Dekker Inc., New York, 333-339, 2002.

[58] Kasap S.O., "Photoreceptors: The Chalcogenides, Handbook of Imaging Materials Second Edition Revised and Expanded edited by Arthur S. Diamond and David S. Weiss", Marcel Dekker Inc., New York, 335, 2002.

[59] Kasap S.O., "Photoreceptors: The Chalcogenides, Handbook of Imaging Materials Second Edition Revised and Expanded edited by Arthur S. Diamond and David S. Weiss", Marcel Dekker Inc., New York, 343-346, 2002.

[60] Heavens O.S., "Optical Properties of Thin Solid Films", Dover Publications, New York, 1965, 1991.

[61] Poelmen D. and Smet P.F., "Methods for the determination of the optical constants of thin films from single transmission measurements: a critical review", *Journal of Physics D: Applied Physics*, **36,** 1850-1857, 2003.

[62] Swanepoel R., "Determination of the thickness and optical constants of amorphous silicon", *Journal of Physics E: Scientific Instrument*, **16**, 1214-1222, 1983.

[63] Adalbert Feltz, "Amorphous Inorganic Materials and Glasses", VCH Publishers, Inc., New York, NY (USA), 371-372, 1993.

[64] Stuke J., "Review of optical and electrical properties of amorphous semiconductor", *Journal of Non-Crystalline Solids*, **4**, 1-26, 1970.

[65]   Swanepoel R., "Determination of surface roughness and optical constants of inhomogeneous amorphous silicon films", *Journal of Physics E: Scientific Instrument*, **17**, 896-903, 1984.

[66]   Van-Popta A.C., "Photoinduced refractive index change in As_2Se_3 by 633nm illumination", *optics express*, **10**, 15, 639-644, 2002.

[67]   Tauc J., "Amorphous and Liquid Semiconductor", Plenum Press, London and New York, 171-194, 1974.

[68]   Manifacier J.C., Gasiot J., and Fillard J.P., "A simple method for the determination of the optical constants n, k and the thickness of a weakly absorbing thin film", *Journal of Physics E: Scientific Instruments*, **9**, 1002-1004, 1976.

[69]   Moharram A.H., Othman, Osman M.A., "Optical characterization of amorphous $Ga_{50}Se_{45}S_5$ films", *Applied Surface Science*, **200**, 143-149, 2002.

[70]   Caricato A.P., Fazzi A., Leggieri G., "A computer program for determination of thin films thickness and optical constants", *Applied Surface Science*, **248**, 440-445, 2005.

[71]   Chambouleyron I., Ventura S. D., Birgin E. G., Martínez J. M., "Optical constants and thickness determination of very thin amorphous semiconductor films", *Journal Applied Physics*, **92**, 3093-3102, 2002.

[72]   Ayadi K. and Haddaoui N., "New approach to the determination of optical constants and thickness of thin dielectric transparent films", *Journal of Material Science: Mater Electron*, **11**, 163-167, 2000.

[73]   Marquez E., Ramirez-Malo J.B., Villares P., Jimenez-Garay R. and Swanepoel R., "Optical characterization of wedge-shaped thin films of amorphous arsenic trisulphide based only on their shrunk transmission spectra", *Thin Solid Films*, **254**, 83-91, 1995.

[74]   Marquez E., Ramirez-Malo J.B., Villares P., Jimenez-Garay R, Ewen P.J.S., and Owen A.E., "Calculation of the thickness and optical constants of amorphous

arsenic sulphide films from their transmission spectra", *Journal of Physics D.*, **25**, 535-541, 1992.

[75] Márquez E., González-Leal J.M., Prieto-Alcón R., M. Vlcek, Stronski A., Wagner T., Minkov D., "Optical characterization of thermally evaporated thin films of $As_{40}S_{40}Se_{20}$ chalcogenide glass by reflectance measurements", *Applied Physics A: Materials Science & Processing*, **67**, 371-378, 1998.

[76] Gonzalez-Leal J.M., Ledesma A., Bernal-Oliva A.M., Prieto-Alcon R., Marquez E., Angel J.A., Carabe J., "Optical properties of thin-film ternary Ge10As15Se75 chalcogenide glasses", *Materials Letters*, **39**, 232-239, 1999.

[77] Marquez E., Bernal-Oliva A.M., GonzaÂlez-Leal J.M., Prieto-Alcon R., Ledesma A., Jimenez-Garay R., Martil I., "Optical-constant calculation of non-uniform thickness thin films of the $Ge_{10}As_{15}Se_{75}$ chalcogenide glassy alloy in the sub-band-gap region (0.1-1.8eV)", *Materials Chemistry and Physics*, **60**, 231-239, 1999.

[78] Moharram A.H., Othman A.A. and Osman M.A., "Optical characterization of amorphous $Ga_{50}Se_{45}S_5$ films", *Applied Surface Science*, **200**, 143-149, 2002.

[79] Bakr N.A., El-Hadidy H., Hammam M., Migahed M.D., "Refractive index, extinction coefficient and DC conductivity of amorphous arsenic triselenide thin film doped with silver", *Thin Solids Films*, **424**, 296-302, 2003.

[80] Gonzalez-Leal J.M., Prieto-Alcon R., Angel J.A., Marquez E., "Optical properties of thermally evaporated amorphous $As_{40}S_{60-x}Se_x$ films", *Journal Non-Crystalline Solids*, **315**, 134-143, 2003.

[81] El-Sayed S.M., Amin G.A.M., "Surface roughness and dispersion parameters of indium doped amorphous As_2Se_3 thin films", *NDT&E Interational,* **38**, 113-117, 2005.

[82] Tigau N., Ciupina V., Prodan G., "The effect of substrate temperature on the optical properties of polycrystalline Sb2O3 thin films", *Journal Crystal Growth*, **277**, 529-535, 2005.

[83]   Fayek S.A., El-Sayed S.M., "Optical properties of amorphous Ge28-xSe72Sb x thin films", *NDT&E Interational,* **39**, 39-44, 2006.

[84]   Gonzalez-Leal J.M., Mir. Vlcek, Prieto-Alcon, A.Stronski, Wagner T., Marquez, "Thermal Relaxationof the structural and optical properties of amorphous $As_{40}S_{60-x}Se_x$ Films", *Journal Non-Crystalline Solids*, **326**, 146-153, 2003.

[85]   Rodriguez J., Gomez M., Ederth J., Niklasson G.A., Granqvist C.G., "Thickness dependence of the optical properties of sputter deposited Ti oxide films", *Thin Solid Films*, **365**, 119-125, 2000.

[86]   El-Sayed S.M., Amin G.A.M., " Surface roughness and dispersion parameters of indium doped amorphous As_2Se_3 thin films", *NDT&E international*, **38**, 113-117, 2005.